Stony Brook University

The official electronic file of this thesis or dissertation is maintained by the University Libraries on behalf of The Graduate School at Stony Brook University.

Green CO$_2$ Processing for Manipulating Structures and Electrical Properties of Organic Photovoltaic Devices

A Dissertation Presented

by

Levent Sendogdular

to

The Graduate School

in Partial Fulfillment of the

Requirements

for the Degree of

Doctor of Philosophy

in

Materials Science and Engineering

Stony Brook University

December 2015

Stony Brook University

The Graduate School

Levent Sendogdular

We, the dissertation committee for the above candidate for the

Doctor of Philosophy degree, hereby recommend

acceptance of this dissertation.

Tadanori Koga – Dissertation Advisor
Professor, Department of Materials Science and Engineering

Jonathan Sokolov
Professor, Department of Materials Science and Engineering

T.A. Venkatesh
Professor, Department of Materials Science and Engineering

Chang-Yong Nam
Adjunct Professor, Department of Materials Science and Engineering

This dissertation is accepted by the Graduate School

Charles Taber
Dean of the Graduate School

Abstract of the Dissertation

Green CO$_2$ Processing for Manipulating Structures and Electrical Properties of

Organic Photovoltaic Devices

by

Levent Sendogdular

Doctor of Philosophy

in

Materials Science and Engineering

Stony Brook University

2015

It is known that morphological, optical and electrical properties of polymer-fullerene nanoparticle organic photovoltaic devices (OPVs) are significantly influenced by individual and integrated structures of the components blended together as photovoltaic active layers. In many cases, conventional thermal and solvent annealing processes do not provide robust control over multi-interfacial systems; therefore, the true potentials of OPVs are still limited with these post-processing treatments available up to now. In this thesis, I report alternative use of supercritical CO$_2$ (scCO$_2$) as a low-temperature and green plasticization agent. A poly(3hexylthiophene)-phenyl-C$_{61}$-butyric acid methyl ester (P3HT-PCBM) blend system was used as a model system, and the effects of various CO$_2$ process conditions, thickness of the blend films, filler concentrations on the structures were investigated by using a suite of surface sensitive techniques including X-ray diffraction, neutron reflectivity, and atomic force microscopy. In addition, I performed conductivity experiments for the scCO$_2$ treated P3HT/PCBM films, demonstrating that the defect densities, charge trap densities, and carrier concentrations are significantly improved by the optimized scCO$_2$ condition. The understanding of the structure-property relationship would lead to development of new polymer-based OPVs.

Dedication Page

To my fiancée and my family.

Table of Contents

List of Figures

List of Tables

Acknowledgments

I would like to express my sincere gratitude to my thesis advisor Dr. Tadanori Koga for his excellent guidance, patience, friendship, continuous inspiration and support during my PhD studies. He has provided deep understanding and insightful discussions related to my research and also the development of my personal career. His encouragement and moral support have been incredibly helpful, especially during the most difficult times in my studies. I could not imagine having a better advisor and mentor for my PhD studies. It would not have been possible to complete this doctoral thesis without his mentorship and support.

I would like to thank Dr. Maya Endoh for her guidance and assistance during my years in Koga's group. I also would like to thank my committee members, Prof. Jonathan Sokolov, Prof. T.A. Venkatesh and Prof. Chang-Yong Nam for their helpful suggestions and insightful comments on my thesis. I am also indebted to Prof. Chang-Yong Nam for his strong technical support on various laboratory instruments at Brookhaven National Laboratory.

Furthermore, I would like to thank Dr. Sushil Satija, and Dr. Bulent Akgun for their invaluable insights on various neutron scattering experiments at the National Institute of Standards and Technology (NIST), Center for Neutron Research, Gaithersburg MD. I would further like to acknowledge Dr. Masafumi Fukuto, Dr. Andrei Fluerasu, and Dr. Lutz Wiegart for their technical support at the National Synchrotron Light Source, Brookhaven National Laboratory (BNL). Additionally, I would like to thank Dr. Dmytro Nykypanchuk from Center

for Functional Nanomaterials (CFN), BNL for the GID and AFM experiments. I am also indebted to my lab mates Dr. Naisheng Jiang and Mani Sen for their support and encouragement.

Finally, most importantly, I pass my biggest gratitude to my fiancée Selda Topcu for her love, smile, support, and understanding during my PhD study. I would like to thank my parents for their unwavering love and support throughout my life.

1. Chapter 1: General Introduction

1.1. Motivation and Goal

At temperatures and pressures above the critical point values, one-component fluids can have densities and solvent properties approaching those of the corresponding liquid. Fluids in this regime are defined as "supercritical fluids" (SCFs) (Fig.1-1). SCFs have been widely utilized as regeneration solvents in a range of technical and chemical processes, such as chromatography, extraction, reactor cleanup and preparation of pharmaceutical products[1-3]. The unique features of SCFs are that the solvent quality of SCFs is pressure or/and temperature dependent, while the diffusion coefficient is closer to that of a gas. By varying the external parameters of temperature and pressure, one can control the interactions between the polymer and the fluid environment. In particular, much attention has been focused on supercritical carbon dioxide (scCO$_2$) since CO$_2$ has a moderate critical point with T_c = 31.3 °C and P_c = 7.38 MPa and is an environmentally benign solvent.
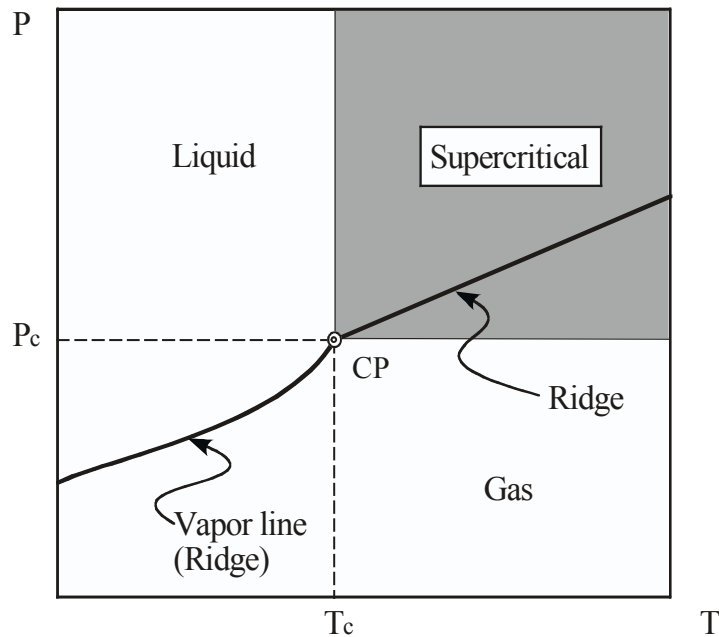
Figure 1-1 Schematic phase diagram of CO$_2$ near the critical point (CP)

However, these potentials of scCO$_2$ have not fully realized yet for polymer processing. This is due to the fact that only a limited class of polymers called "CO$_2$-philic", such as highly fluorinated or silicone-based polymers can be dissolved in CO$_2$ under relatively moderate conditions ($T < 100°C$ and $P < 50MPa$)[4].
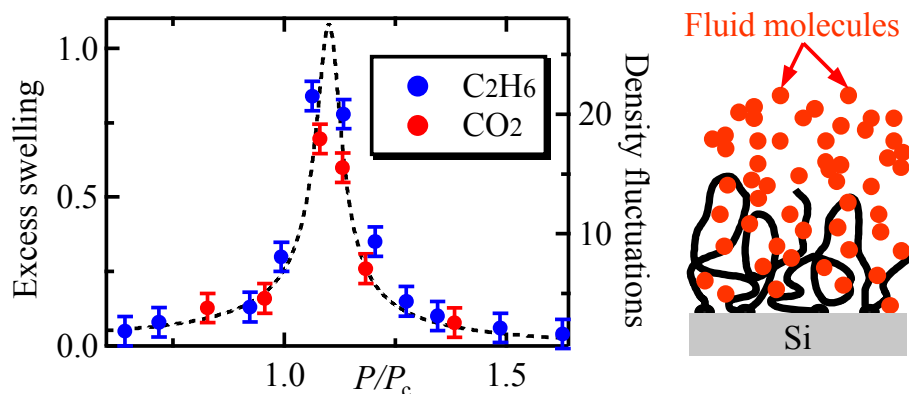
Figure 1-2 Strong correlation between the magnitude of the excess swelling of deuterated polybutadiene thin films (~ 50 nm in thickness) in both CO$_2$ and ethane and the magnitude of the density fluctuations near their critical points.

Recently, our research group found a new piece of experimental evidence: CO$_2$ molecules can be absorbed to a large extent in polymer thin films (< 100 nm thickness) near the critical point of CO$_2$ even when the bulk miscibility with CO$_2$ is very poor[5-8]. The enhancement in the absorption is universal and independent of the polymer/scCO$_2$ combinations. In contrast to conventional solvents, the region of the anomalous adsorption of CO$_2$ molecules is determined by the correlation length of the density fluctuations of CO$_2$ near the critical point and hence only occurs within the first few ten nanometers depth from the polymer/scCO$_2$ interface[5]. Even though it may be a small fraction of the overall film thickness, it is sufficiently large to affect surface properties of polymer films, facilitating the use of such density fluctuating supercritical fluids as new process environments or fields for polymer surface and interface processing. Moreover, our group revealed that the density fluctuating scCO$_2$ can be used as an effective

plasticizer to induce highly ordered molecular aggregation structures of semicrystalline polymers[9, 10].

In my thesis, a special attention was given to poly 3-hexylthiophene (P3HT)/phenyl-C61-butyric acid methyl ester (PCBM) blend thin films, which have been frequently highlighted as an alternative photovoltaic device (OPV). However, the power conversion efficiency is still about 10%[11], which is quite lower than that of other crystalline Si solar cells (~ 30%). Therefore further improvement of electrical properties is urgently required in order to cultivate future commercial markets for OPV. It is known that interchain polymer-polymer interactions control self-assembling ordered structures of conjugated polymers. The interchain interactions are mediated predominantly through weak van der Waals interactions that introduce structural defects in a polymer layer during thin film formation on a substrate via solution processing techniques such as spin-coating[12], bar coating[13], and ink-jet coating[14]. Structural defects arising from poorly organized chain arrangements could result in poor electrical properties by limiting interchain charge carrier transport. Hence, I utilized the density fluctuating CO_2 annealing for P3HT/PCBM systems as an alternative post-annealing process in place of conventional high temperature thermal annealing. As will be discussed in the Chapter 2, the results are intriguing to show that the density fluctuating CO_2 annealing facilitates the self-assembling of not only intermolecular backbone layer but also interchain π-π stacking of the P3HT alkyl side chains.

In Chapter 3, I focus on the effect of CO_2 annealing on self-organization of nanoparticles in an organic matrix. Control of layered structures at the nanometer scale is particularly desirable for thin-film organic devices because this essentially affects electrical, optical, and mechanical properties. To spontaneously fabricate such layered structures, careful control of driving forces such as phase separation, crystallization, or surface energy of materials is necessary. For

example, Goffri et al. reported the spontaneous formation of bilayer structures between poly(3-hexylthiophene) (P3HT) and polyethylene (PE) in mixture films. The crystallization of PE induces effective encapsulation of P3HT at the organic-semiconductor/dielectric interface, resulting in mechanically robust and high-performance thin film transistors[15]. On the other hand, Wei et al. synthesized phenyl C_{61} butyric acid methyl ester (PCBM) with a fluorocarbon chain, which has a low surface energy and prefer to migrate to the air/polymer interface, and created a very thin layer of the PCBM nanoparticles at the polymer/air interface used for organic thin film transistors[16]. Achieving the precise control of such driving forces is complicated, however, because specific synthetic surface modifications of nanoparticles are often required[17-19]. Moreover, when constrain placed on configurations of polymer chains to accommodate nanoparticles become significant, nanoparticles even compatible with polymers are migrated to the polymer/air surface (the so-called "entropy-driven" segregation[20-22]). An understanding of the delicate balance of the enthalpic and entropic effects is still limited and the precise control of the nanoparticle dispersions embedded in nanometer-thick polymer films remains a challenge. Recently, our group found that density fluctuating $scCO_2$ induces surface migration of nanoparticles embedded in polymer thin films to the topmost polymer surface regardless of a choice of nanoparticles[23]. I found that the density fluctuating CO_2 process promotes the surface segregation of PCBM nanoparticles to the $P3HT/CO_2$ interface. Moreover, by optimizing the surface migrated structures of the nanoparticle, I found that the electron conductivity of the P3HT/PCBM blend film increases by a factor of 2.5 compared to that of a P3HT/PCBM blend film prepared by a conventional post-thermal annealing process.

In Chapter 4, I performed preliminary experiments to investigate the effect of the interfacial polymer chain conformations at the polymer-substrate interface. Solid-polymer

interfaces play crucial roles in the multidisciplinary field of nanotechnology and are the confluence of physics, chemistry, biology, and engineering. There is now growing evidence that polymer chains irreversibly adsorb even onto weakly attractive solid surfaces, forming a nanometer-thick adsorbed polymer layer ("adsorbed polymer nanolayers"). Our group has been working to reveal the structures and dynamics of the adsorbed nanolayers composed of homopolymers and their roles in the unusual physical and mechanical properties of polymer thin films[24-30]. However, the effects of nanoparticles on the structures and dynamics of the adsorbed nanolayers are not known yet. Addition of a diverse array of inorganic nanoparticles to polymer thin films is vital. It is known that nanoparticles often migrate to the film-substrate interface[31-43] and form a diffused immobile interfacial layer[31, 37, 40, 43], which serves to screen the polymer-substrate interaction and suppress dewetting. My results demonstrated that the polymer adsorbed layer structures are quite different, depending on the interactions between the polymer-substrate and substrate-nanoparticle. The questions to be answered are how the diffused immobile interfacial layer influences the electrical property/power conversion efficiency.
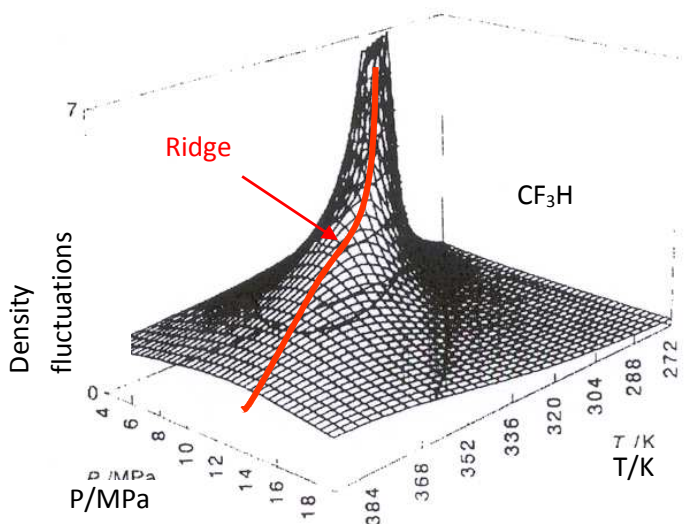
Figure 1-3 Three-dimensional density fluctuation map for CF3H18. The critical point locates behind the peak.

1.2. Significance of Density Fluctuating Supercritical Carbon Dioxide for Polymer Surface Processing

1.2.1. Introduction to density fluctuating supercritical fluids (SCFs)

It is well known that SCFs are composed of inhomogeneous regions with high and low densities at the microscopic scale[44]. Near the critical point, the microscopic thermal fluctuations become strongly correlated, leading to large-scale, coherent density fluctuations [45]. The existence of the long-range density fluctuations in SCFs has been experimentally observed by partial molar volume measurements [46-52] and small-angle x-ray scattering experiments [53-55]. The density fluctuations, $<(\Delta N)^2>/<N>$, can also be theoretically calculated from the thermodynamic relation[45],

$$\left\langle (\Delta N)^2 \right\rangle / \left\langle N \right\rangle = (N/V)\kappa_T k_B T, \qquad (1\text{-}1)$$

where N is the number of molecules in the corresponding volume V, k_B is the Boltzmann constant and κ_T is the isothermal compressibility. Fig. 1-3 shows density fluctuations for CF_3H as a function of temperature and pressure[55]. The isothermal compressibility was calculated from the *P-V-T* data for the substance. From the figure one can see that the amplitude of the fluctuations shows a maximum under each isothermal condition. The locus of these maxima is known as "the density fluctuation ridge" (designated as the red line in Fig. 1-3 and the two-dimensional projection is also shown in Fig. 1-1. The ridge emanates from the critical point where the amplitude of the density fluctuations diverges, and is a general feature for substances [53, 55]. It is also known that the ridge corresponds to a maximum or minimum of various physical quantities such as isothermal compressibility[56], thermal conductivity[57], sound velocity[58], and partial molar

volumes[46, 59]. In addition, the rate constants or equilibrium constants of various chemical reactions in SCFs show maxima, minima or inflection points at the ridge[59].
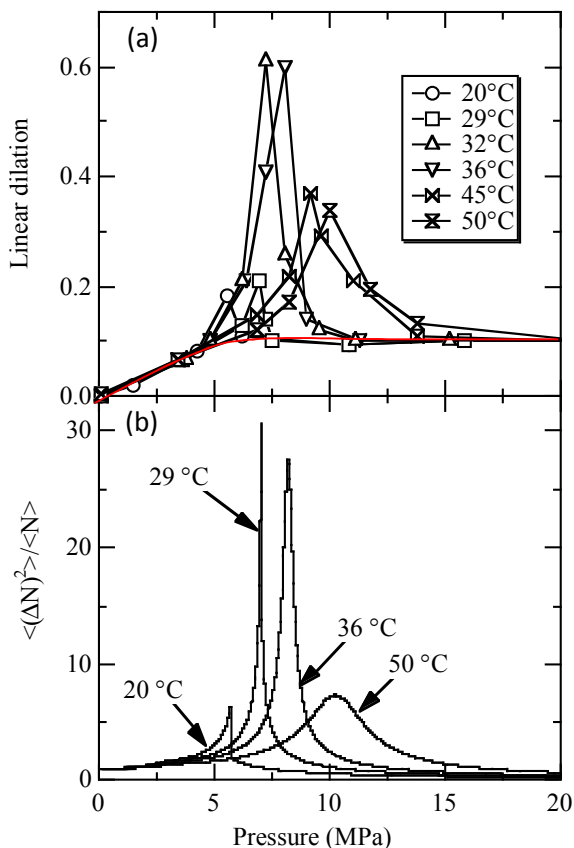
Figure 1-4 (a) Linear dilation for the d-SBR thin films as a function of pressure at different temperatures. The red line corresponds to the swelling behavior of the bulk SBR film. (b) Calculated density fluctuations of CO_2 based on the equation of state of CO_2.

1.2.2. Density-fluctuation-induced swelling of polymer thin films in scCO₂

Here I show that the density fluctuation ridge also corresponds to the region where the solubility of CO_2 with polymer thin films has a maximum. Fig. 1-4 (a) shows the linear dilation (S_f) of the deuterated styrene-butadiene random copolymers (d-SBR) films (the original film thickness of 35 nm) determined by the neutron reflectivity (NR) experiments. The large penetration depth inherent with neutrons makes NR an ideal tool to determine *in situ* thickness,

composition, and interfacial structures of polymer thin films immersed in fluids or gases, under high pressure in thick walled vessels[7].

The linear dilation was calculated from the equation $S_f = (L-L_0)/L_0$, where L and L_o are the measured thickness of the swollen and unswollen polymer thin films, respectively. From the figure one can see that the large maximal values of 0.6 are observed in the dilation curves at $T = 32$ and 36 °C and the values of the maxima gradually decrease to approximately 0.35 with increasing temperature at $T > 36$ °C. As the pressure is increased well into the liquid or supercritical region, i.e., $P > 15$ MPa, the film collapses and only a small dilation of approximately 10 %, which is the equivalent to the bulk swelling (shown by the red line), is observed[7]. It should be emphasized that the dilation was an equilibrium quantity, which was a function only of the pressure and temperature of CO_2[5].

From close examination of the density fluctuations in pure CO_2 calculated by eq. (1-1), it was found that the magnitude of the excess swelling observed is strongly correlated to that of the density fluctuations in pure CO_2, and the anomalous maxima occurred along the density fluctuation ridge (Fig. 1-4(b))[5]. Hence, in contrast to the existing concept, i.e., the density of the fluid controls the solubility of CO_2 with bulk polymers[60-68], the long-range density fluctuations can directly control the solubility of CO_2 with polymer thin films. Here is the summary of the other novel characteristics of the density-fluctuation-induced anomalous swelling:

The anomalous swelling can be scaled by the radius of polymer gyration (R_g) and is a surface effect which occurs only within the first few ten nanometers thickness of the polymer/CO_2 interface [5].

The magnitude of the anomalous swelling may depend on the hardness of the films rather than the solubility of the homopolymers with CO_2[7]. For example, the excess dilation in glassy

polymers with the glass transition temperatures (T_g) of about 100°C is at most 30%, while those in the rubber polymers exceed 60%[5, 7].

a) The anomalous swelling occurs in both spun-cast polymer thin films and polymer brushes regardless of the immobilization of the chain ends[8].

b) The anomalous swelling is associated with a large decrease in T_g of the polymer thin films[6].

c) The anomalous swelling induces the excess enhancement in the interfacial width of two immiscible polymers[69].

d) The anomalous swelling of polymer thin films is also observed at the density fluctuation ridge of supercritical ethane (T_c = 32.3°C, P_c = 4.8MPa)[70], suggesting that the excess swelling may be a general phenomenon regardless of a choice of SCFs.
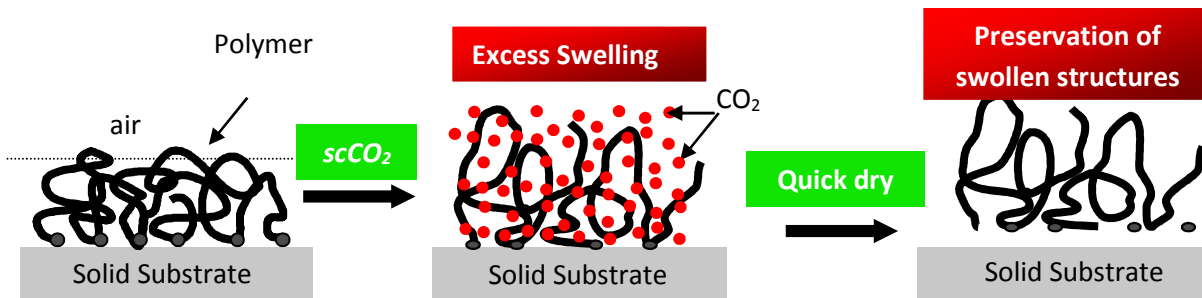
Figure 1-5 New concept for creating low-density polymer thin films using the scCO$_2$

1.2.3. "Density-fluctuating scCO$_2$ process" for fabrication of functional polymer surfaces

1.2.3.1. Thin Films

Moreover, when the fluid was released rapidly, the glassy polymer thin films could be vitrified and preserved the swollen structures as they were in scCO$_2$[6]. As schematically shown in Fig. 1-5, this utilizes the vitrification of the polymer chains induced by pressure quench. This

process is known to form porous structures of micron scales in the bulk[71, 72]. However, in the case of polymer thin films, by using small-angle x-ray scattering (SAXS) experiments with reflection geometry[73], it was found that the average size of the pores formed in the expanded poly-phenylene vinylene (PPV) film was 0.8 nm[74], i.e., molecular scale porosity. At the same time, x-ray reflectivity (XR) experiments proved that the density of the $scCO_2$-treated PPV ultrathin films (50 nm thickness) was decreased by 15%[74]. In addition, XR experiments clarified that the low-density PPV film was stable for at least 6 months at room temperature, allowing further subsequent processing[74]. Consequently, "*the density-fluctuating scCO₂ process*", i.e., a combined use of the anomalous swelling and subsequent pressure quench, can produce a large degree of molecular level porosity within the expanded polymer thin films [75], leading to development of new functionalities of the films, such as index of refraction[74, 75], dielectric constant[75], glass transition temperature[75], good metallization property[76], and high gas permeability [77]. It should be emphasized that the density-fluctuating $scCO_2$ process is not only "environmentally-friendly" but also "polymer-friendly" because of its mild operating temperature (typically 30-50°C) and pressure conditions (8-15MPa).
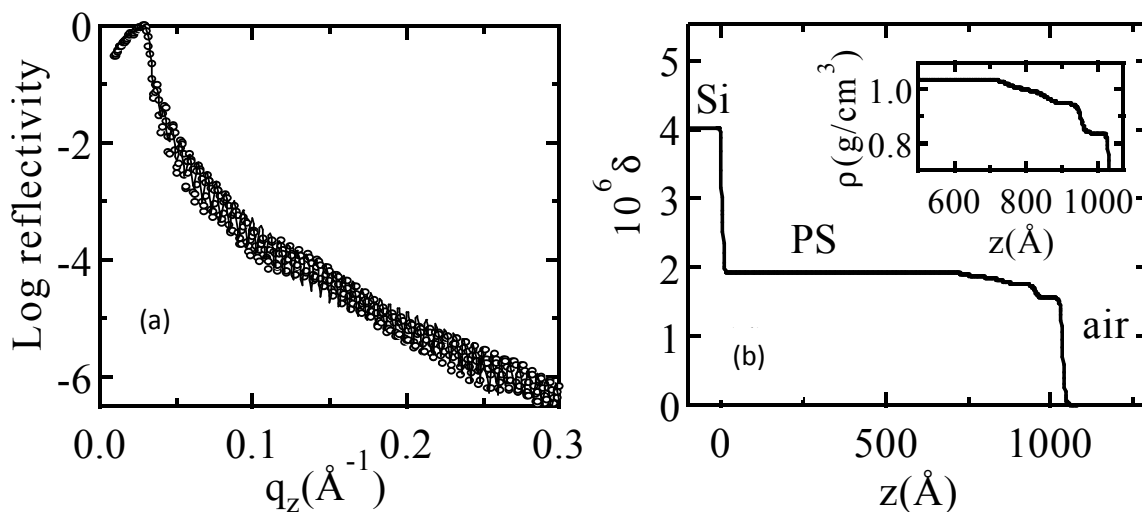
Figure 1-6 (a) Measured RF (○) and refinement (solid line) of the thick frozen PS1 film. (b) δ (index of refection for x-ray) profile used for the refinement. In the inset, the density of the film (ρ) near the polymer-air interface regime is shown

1.2.3.2.   Thick films

In order to deter mine whether this anomalous swelling is strictly a thin film phenomenon, we also characterized the exposed polystyrene (PS) thick film (~110 nm thickness) by using X-ray reflectivity (XR). Fig. 1-6(a) shows the XR profile where we can clearly see a pronounced beating pattern, indicating that the film is not homogenous. Hence, a Fourier Transform (FT) analysis method which can provide detailed density profiles even for films of relatively low scattering contrast[78] was used.

In this technique the XR and FT data are fitted simultaneously using a dispersion model. The best fit (solid lines in Fig. 1-6(a)) was obtained with the dispersion model shown in Fig. 1-6(b) which consisted of six layers, silicon substrate, native oxide, and four different PS layers, based upon the number of the peaks in the FT profile[75]. As shown in the inset of Fig. 1-6(b), the XR results proved that a layer about 10 nm in thick was formed at the polymer/vacuum surface with a reduced density of $\rho=0.83$ g/cm^3 and a relatively sharp interface of about 2 nm with the layers beneath. The subsequent layers also have reduced density, but these layers are more diffuse and decay over a region of approximately 20 nm towards a uniform layer with the bulk density ($\rho =1.04$ g/cm^3) [75].

Consequently, the XR data indicated that scCO$_2$ penetrates into thick films as well, but to limited extent of approximately 30 nm thickness. Even though it may be a small fraction of the overall film thickness, it is sufficiently large to affect the surface tension and surface energy properties that are crucial in determining adhesion, metallization, and wetting. Hence the density-fluctuating scCO$_2$ process could be further extended to general cases of surface modification for *bulk* (thick) polymer films.

1.2.4. Comparison with other works

The anomalous swelling of relatively thicker polymer films (100 - 300 nm) near the critical point of $scCO_2$ was experimentally reported by the Johnston and Green groups[79, 80]: By using high-pressure spectroscopic Ellipsometry, they found that the anomalous swelling occurred in a variety of polymer thin films including the CO_2-philic fluorinated polymer, glassy polymers, semi-crystalline polymer, and block copolymer films. Based on the multilayer model analysis for the spectroscopic data, they suggested a middle layer between the two interfacial layers, i.e., polymer/CO_2 and polymer/substrate interfaces, was responsible for the anomalous swelling[80]. This is inconsistent with our XR data described above and may be due to the lack of the experimental resolution of Ellipsometry for determination of the density profile in the direction normal to the surface, while the XR method using a novel inversion method can provide it directly[78].

Theoretically, Wang and Sanchez studies the anomalous sorption of CO_2 molecules near the critical point by using a combination of the gradient theory of inhomogeneous systems and the Sanchez-Lacombe equation of state [81]. As a result, they found that an excess adsorption layer of CO_2 molecules was formed on the film surface and showed the similar anomalous swelling at the ridge. Although they concluded that the critical adsorption of CO_2 on an attractive surface was responsible for the anomalous swelling, they never showed the conformation of polymer chains in density fluctuating $scCO_2$. In addition, the predicted thickness was at most 3 nm, which is at least one order of magnitude smaller than those determined experimentally [5-8, 79, 80].

On the other hand, multiscale simulation[82, 83] predicted excess expansion of a single polymer chain in a SCF regardless of solute-solvent interactions when the solvent's compressibility becomes larger. Sumi et al. proposed that an increase in the local solvent density

around a solvophilic polymer chain or the formation of a large correlation hole around a solvophobic polymer chain (i.e., excluding the fluid molecules around the polymer chain) is induced and the polymer chain in the solvation structures is anomalously expanded as a thermodynamically stable state[82, 83]. This expansion causes additional large solvent-density fluctuations around the polymer chain over a large area compared with the correlation length of the solvent molecules, thus lowering the free energy of a SCF/polymer system[44].

1.2.5. Theoretical models

In order to further understand the mechanism of the anomalous expansion driven by long-range density fluctuations in SCFs, Koga and co-workers proposed a simple thermodynamic model which assumed that polymer chains belong to only two thermodynamic states, i.e., the excess swollen state (denoted by E) and non-excess swollen state (denoted by N). Similar two-state model has been widely used to determine conformation stability of a protein molecule during a unfolding process by gradually changing its environmental conditions[84]. Polymer chains may undergo the transition between the E and N states according to a simple kinetic model,

$$\text{N} \rightleftharpoons \text{E} \qquad (1\text{-}2)$$

with rate constants k_N and k_E for the collapse of polymer chains and for the expanding of polymer chains, respectively. The difference in the Gibbs free energy between the E and N states is defined as $\Delta G = G_E - G_N$ and the total differentiation is then given by

$$d(\Delta G) = dP\Delta V - dT\Delta S, \qquad (1\text{-}3)$$

where $\Delta V = V_E - V_N$ and $\Delta S = S_E - S_N$ are the changes in the volume and entropy of the entire system due to the anomalous expansion, respectively. ΔG is related to the equilibrium constant,

$K_{ea} \equiv k_E / k_N = X_E / X_N$ via $\Delta G = -k_B T \ln K_{ea}$, where X_E and $X_N = 1 - X_E$ are probabilities of the

E and N state, respectively. To convert the swelling data into the probabilities, the following

assumptions were made: The observed excess expansion can be decomposed into a weighted

average of the two states,

$$l_e = X_E l_e^{max} + (1 - X_E) l_e^{min}, \tag{1-4}$$

where l_e^{max} and l_e^{min} correspond to the l_e value for the E and N state, respectively. The other

assumption is that only the E state contributes to the excess expansion (i.e., $l_e^{min} = 0$) and at the

density fluctuation ridge all chains belong to the E state (i.e., $X_E = 1$) such that l_e^{max} corresponds

to the l_e value. With these assumptions, ΔG can be then simplified as follows:

$$\Delta G = -k_B T \ln\left[l_e / (l_e^{max} - l_e) \right]. \tag{1-5}$$
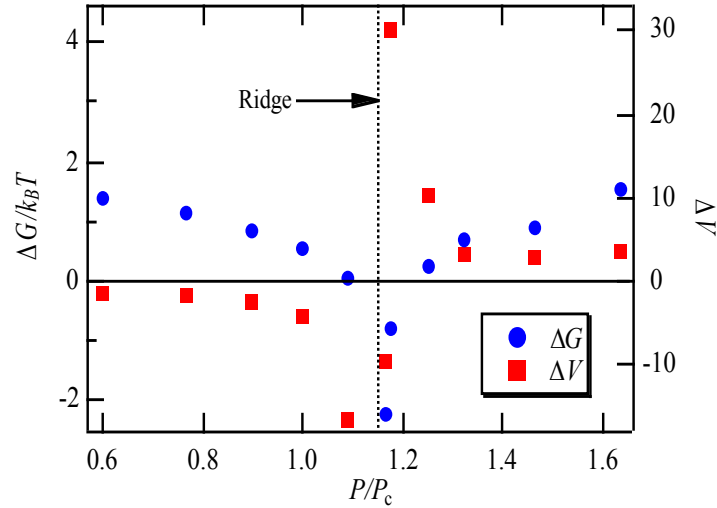
Figure 1-7 Pressure dependences of ΔG (blue circles) and $\Delta V = (\partial \Delta G / \partial p)_T$ (red squares) for the deuterated polybutadiene thin films in SCFs at $T = 1.15 Tc$.

Fig. 1-7 shows the pressure dependence of ΔG and $\Delta V = \left(\partial \Delta G / \partial P \right)_T$ calculated by the experimental l_e values shown in Fig. 1-2. As expected, ΔG becomes negative (and minimum) at around the ridge. The more important point is that ΔV is negative at the lower-pressure side of P_{ridge} (=1.15 P_c) during the pressurization process, while ΔV changes the sign to positive after passing P_{ridge}. In other words, the amount of the excess absorption of SCF molecules increases with increasing pressure at $P < P_{ridge}$ and, in contrast, decreases with increasing pressure at $P > P_{ridge}$. Hence, this two-state model proposes that the density fluctuation ridge is a unique environmental condition on the solvation property of SCFs for polymer chains: the strength of the excess absorption of the fluid molecules becomes stronger or weaker across the density fluctuation ridge independently of polymer-fluid interactions, resulting in the maximum chain expansion at the density fluctuation ridge. Furthermore, the significant change in ΔV at around the ridge is indicative of a large difference in compressibility between the E and N states. This supports the aforementioned mechanism that a high response of density fluctuations in SCFs to the conformation changes of flexible polymer chains is essential to lower the free energy of the entire system.

1.2.6. Polymer nanocomposite thin films

Recently, our research group discovered that the density fluctuating scCO$_2$ also induces surface migration of nanoparticles to the polymer/CO$_2$ interface for different kinds of nanoparticle ligands, different sized nanoparticles, and different polymer matrices[23]. Fig. 1-8 (right) shows a representative result for PS (molecular weight (M_w) =200kDa and polydispersity (M_w/M_n) =1.06, Pressure Chemical Co.)/phenyl-C61-butyric acid methyl ester (PCBM, Sigma-

Aldrich Co.) thin films. The PCBM nanoparticles (the average diameter of 3 nm) were first dissolved in toluene.
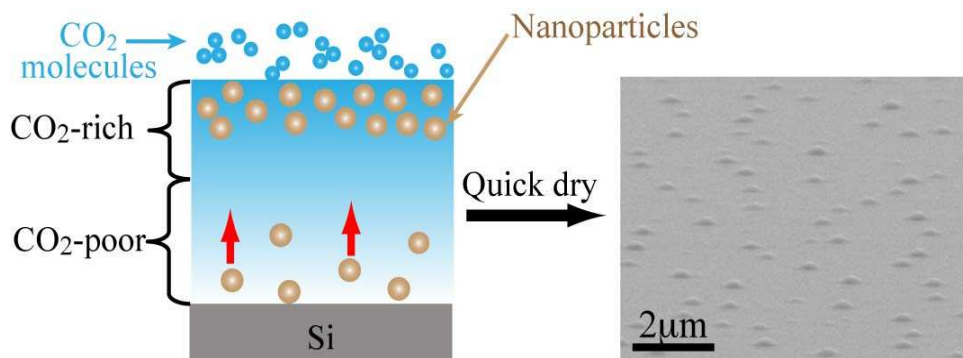
Figure 1-8 Proposed mechanism of scCO2-induced surface segregation of nanoparticles. In a polymer matrix, a concentration gradient of fluid molecules is formed due to limited penetration power of fluids in a viscous polymer matrix. Nanoparticles with critical wetting of CO_2 molecules near the ridge condition move to the CO_2-rich phase by taking advantage of a steep concentration gradient of the CO_2 concentration near the surface. The right SEM image corresponds to the frozen PS/PCBM nanocomposite thin film after treated at the density fluctuation ridge condition and subsequent quick dry.

The concentration of the nanoparticles against the polymer was 10 % by weight. PS/PCBM thin films (10-150 nm in thickness) were prepared by spin-casing onto cleaned Si substrates and then annealed for 24h in vacuum at T=160 °C >> T_g of PS in order to remove residual solvents and spin-induced stress. The PS/PCBM thin films were then placed into a high-pressure cell designed for the scCO2 processing (Fig. 1-9)[7] and exposed to scCO2 at T = 36 °C and P=8.2MPa (i.e., the density fluctuation ridge condition) for 1h. The system was subsequently depressurized to atmospheric pressure quickly (within 10s) in order to solidify the film structures using the vitrification of the polymer matrix[75]. As seen in Fig. 1-8, the hemispherical PCBM aggregates with the diameters of 0.1-1 μm and the heights of 50-200 nm are formed on the film surface after the scCO2 process. Note that the untreated films prior to the scCO2 process have the flat and smooth surface, while the presence of the interfacial segregation layer (about 2 nm in

thickness) of the PCBM nanoparticles at the substrate interface was indicated by x-ray reflectivity results. Further experiments with varying CO_2 pressure conditions have clarified that the surface segregation occurs only near the density fluctuation ridge condition[23]. Moreover, it was found that similar surface segregation occurs for different sets of polymers and polymer-soluble nanoparticles [85].
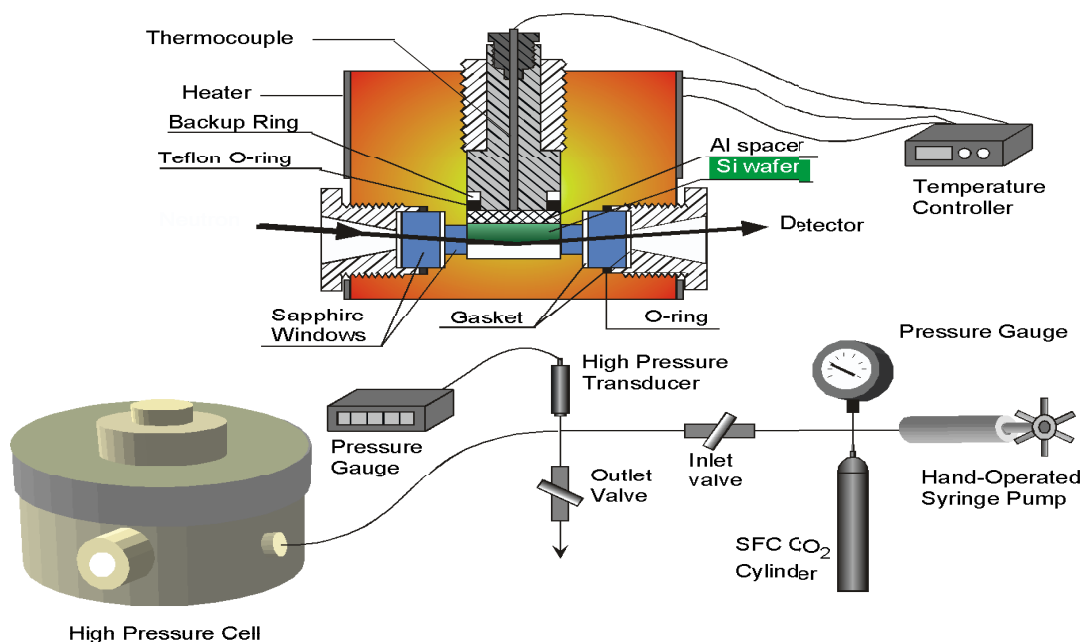
Figure 1-9 Schematic view of the high pressure chamber designed for the scCO$_2$ annealing experiments used for the study. The *in-situ* neutron reflectivity measurements were also performed with the chamber.

Fig. 1-10 shows an example of the surface segregated structures of polyhedral oligomeric silsesquioxane derivatives co-polymerized with styrene monomers (POSS-PS from Hybrid Plastics Ins., the weight fraction of the POSS component is 15%) embedded in the same PS. In this case, the adverse monomeric enthalpic effect between the polymer and nanoparticles coated with PS is minimal. Interestingly, we found many rim-shaped structures in which spherical clusters (about 100 nm in size) of the POSS-PS nanoparticles exist (Fig. 1-10). Hereafter we

define the aggregates of the nanoparticles at the surface as "nano-aggregates" to distinguish from individual nanoparticles. Furthermore, the cross sectional profile of the surface topographic image reveals that the rim-shaped structures are formed only near the topmost surface area (~ 10 nm in depth) of the entire film (~100 nm in thickness). Hence, these results indicate that the enthalpic contributions are not the central driving force for the $scCO_2$-induced surface segregation. Rather, an entropic effect imposed on the polymer chains owing to the presence of the nanoparticles, the so-called "depletion attraction"[86], should be crucial. In addition, it is suggestive that the morphologies of nano-aggregates depend on a choice of nanoparticles.
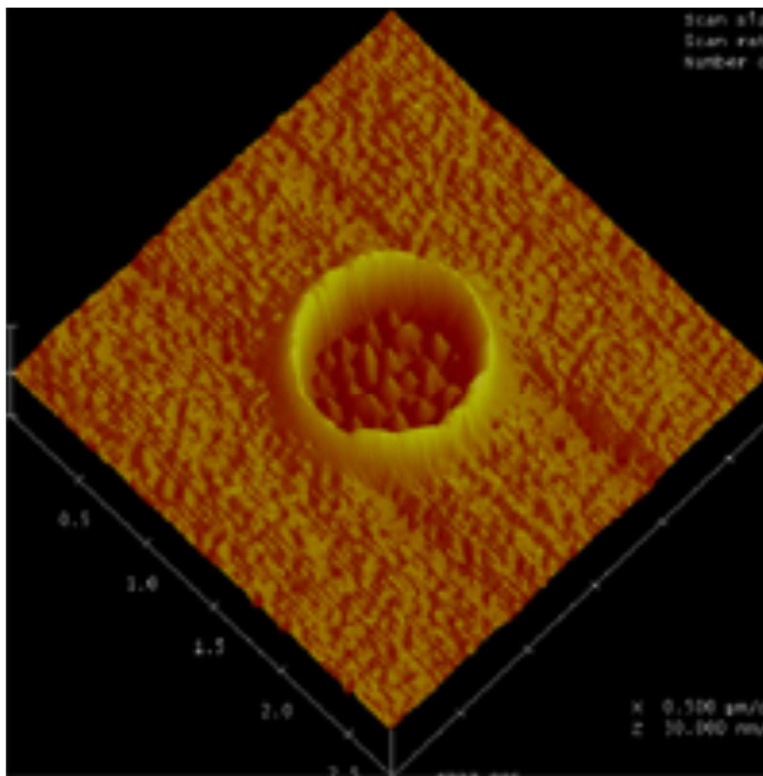
Figure 1-10 Topographic images for the CO_2 treated PS/POSS-PS thin film (100 nm in thickness). The image size is 2.5×2.5 μm^2

It is thus anticipated that the main driving force for the scCO$_2$-induced surface segregation of polymer-soluble nanoparticles is entropic in origin. However, we found that the surface segregation of the PCBM and PS/POSS-PS nanoparticles after the scCO$_2$ process at the density fluctuation ridge disappears when the film thickness becomes less than ~ $4R_g$ thick (R_g is the radius of polymer gyration)[23]. Consequently, the aforementioned entropic penalty imposed on the polymer chains alone is not sufficient to explain the thickness dependence of the nanoparticle dispersions induced by highly compressible scCO$_2$.

1.2.6.1.   Mechanism

When polymer nanocomposite thin films are exposed to scCO$_2$ in the highly compressible region near the critical point, two phenomena are induced independently: (i) excess a*b*sorption of CO$_2$ molecules into a polymer matrix, as described above, and (ii) excess a*d*sorption of CO$_2$ molecules on the nanoparticle surfaces[87-90]. Findenegg has firstly reported the excess surface adsorption of ethylene and sulfur hexafluoride molecules on graphite carbon black particles[87] and similar excess adsorption of CO$_2$ molecules on various particles including silica and octadecyl-bonded silica have been also reported[88-90]. Furthermore, Lal et al. showed that the excess adsorption also takes place in particles with ligand molecules attached, while the degree of the adsorption depends on the interactions between solvent and ligand molecules[91, 92]. We found that the excess absorption expands polymer chains homogeneously or heterogeneously, depending on the balance between the penetration length of the fluid molecules into a polymer and the film thickness[75, 93]. When the film thickness is larger than the penetration length scale of the fluid molecules, a concentration gradient of the fluid is developed at the topmost surface region within the film. We hypothesize that this concentration gradient provokes instability of

the dispersion of the CO_2-wetted nanoparticles and thereby migration of the nanoparticles preferentially to the topmost CO_2-rich region through the concentration gradient. By contrast, when the homogenous excess absorption of the fluid molecules occurs, the resultant anomalous expansion of the polymer chains may reduce the entropic penalty of the chains without expelling the nanoparticles to the free surface, allowing the accommodation of the "CO_2-wetted" nanoparticles within the films. The nanoparticles migrated to the surface would be then coagulated together due to the attractive interaction among them, resulting in the large nano-aggregate structures at the polymer surface.
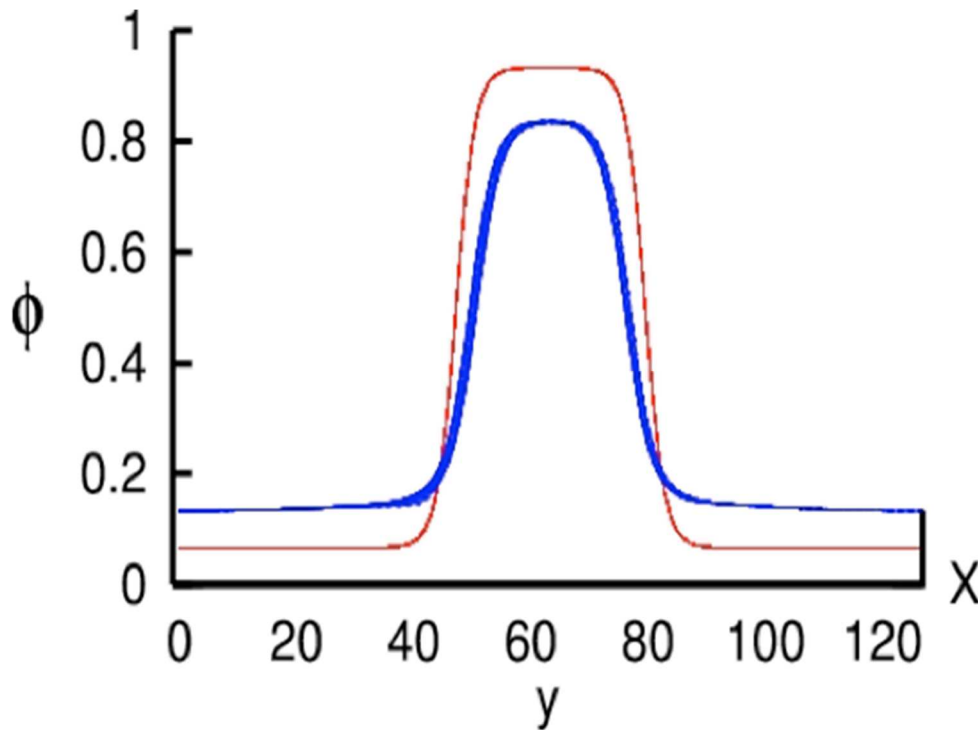
Figure 1-11 Volume fraction profiles of polymer segments at $\chi=2.5$ (red) and after quenching to $\chi=2.3$. The X and Y directions are parallel and perpendicular to the surface of a polymer film, respectively. The decrease in χ broadens the profile, indicating a large numbers of solvent molecules penetrate into the polymer matrix from both polymer/fluid interfaces (at around Y=45 and 80).

1.2.6.2.   Simulation efforts

In order to investigate how a concentration gradient of solvent molecules near the polymer-solvent interface affects the dynamics of particles, we also used a dynamic density functional theory for computing the dynamics of particles embedded in "A" (polymer) and "B" (solvent) fluids in collaboration with Prof. Takashi Taniguchi (Kyoto University). Within this model, we took into account the following three effects: (i) affinities among a particle, A- and B-fluids, (ii) phase separation dynamics of "A/B" binary fluids, and (iii) a hydrodynamic effect on particles and phase separation dynamics.

We assume that spherical particles with a diameter of d (=$2a$, a being a radius) are initially dispersed in a polymer matrix. If d is sufficiently small relative to the inverse of $|\nabla \phi_s|$, where ϕ_s is a volume fraction of the solvent,

$$d|\nabla \phi_s| \ll 1, \tag{1-6}$$

The particles can be then regarded as very small points in the binary fluid. This assumption allows us to incorporate the effect of a concentration gradient into particles at certain positions. When a position of α-th particle is given by r_a, a wetting energy $F_{w\alpha}$ is expressed as

$$F_{w\alpha} = \int \left[\gamma_p \phi_p(r_\alpha + ae_r) + \gamma_s \phi_s(r_\alpha + ae_r) \right] dS \tag{1-7}$$

$$\approx 4\pi a^2 \left[\gamma_p \phi_p(r_\alpha) + \gamma_s \phi_s(r_\alpha) \right] \text{if } a \ll 1/|\nabla \phi_s| \tag{1-8}$$

where the surface integral in eq. (1-7) is performed at the surface of the particle, e_r denotes a radial vector toward the surface from the center, $\phi_p(r_\alpha)$ and $\phi_s(r_\alpha)$ represent the volume fractions of the polymer and solvent at the position r, respectively ($\phi_p + \phi_s = 1$). γ_p and γ_s are particle-polymer and particle-solvent interfacial energies, respectively. Here we introduce a variable of ϕ

$=\phi_p-\phi_s$ so that the following expressions of $\phi_p= (1+\phi)/2$ and $\phi_s= (1-\phi)/2$ can be deduced. Using these expressions,

$$F_w = \sum_{\alpha=1}^{M} F_{w\alpha} \tag{1-9}$$

$$F_{w\alpha} = 4\pi a^2 [(\bar{\gamma}+\Delta\gamma\phi(r_\alpha)], \tag{1-10}$$

Where $\bar{\gamma}\equiv(\gamma_s + \gamma_p)/2$, $\Delta\gamma\equiv(\gamma_p - \gamma_s)/2$. The mixing free energy F_{mix} is then given by

$$F_{mix} = \frac{kT}{v_0}\int[f_0 + \kappa/2(\nabla\phi)^2]dV \tag{1-11}$$

$$f_0 = \frac{1}{N}\phi_p In\phi_P + \phi_s In\phi_s + \chi\phi_p\phi_s \tag{1-12}$$

The total free energy F is given by

$$F = F_{mix} + F_w \tag{1-13}$$

$$= \varepsilon_0 \int [f_0 + \kappa/2(\nabla\phi)^2 + \Gamma/\varepsilon_0\sum_\alpha \phi(r)\delta(r-r_\alpha)]dV, \tag{1-14}$$

where $\varepsilon_0 \equiv kT/v_0$, $\Gamma\equiv 4\pi a^2\Delta\gamma$ and the constant terms are omitted. The chemical potential $\mu(r)= \delta F/\delta\phi(r)$ is expressed as

$$\mu(r) = \varepsilon_0\left\{f_0'(\phi(r)) - \kappa\Delta\phi(r) + \Gamma/\varepsilon_0\sum_\alpha\delta(r-r_\alpha)\right\}. \tag{1-15}$$

The equation describing the phase separation is given as follow:

$$\frac{\partial}{\partial t}\phi(r,t) = -\nabla\cdot(\phi v) + L_0\Delta\mu, \tag{1-16}$$

where L_o is a transport coefficient and v is velocity of a binary fluid. Since the size of the particles is sufficiently small, we can neglect the degree of freedom related to the rotational motion. The equations of motion for α-th particle are given by

$$m\frac{d^2 r_\alpha}{dt^2} = F_\alpha^h \, , \ m = \frac{4}{3}\pi a^3 \rho_p \tag{1-17}$$

$$F_\alpha^h = -\varsigma \left\{ \frac{dr_\alpha}{dt} - v(r_\alpha) \right\} \, , \ \varsigma = 6\pi\eta a \tag{1-18}$$

$$F_\alpha^w = -\nabla_\alpha F_{w\alpha} = -\Gamma\nabla_\alpha \phi(r_\alpha) \tag{1-19}$$

$$F_\alpha^L = \sum_{\beta(\neq\alpha)} F_{\alpha\beta}^L$$

$$= \sum_{\beta(\neq\alpha)} \frac{3}{2}a^2\pi\eta \frac{(\dot{r}_\beta - \dot{r}_\alpha)\cdot \hat{r}_{\alpha\beta}}{\left(\left|r_\alpha - r_\beta\right| - 2a\right)} r_{\alpha\beta} \tag{1-20}$$

where ρ_p and η are mass density of particles and viscosity of the polymer, respectively, and $\hat{r}_{\alpha\beta} \equiv (r_\alpha - r_\beta)/\left|r_\alpha - r_\beta\right|$. In the right hand side of eq. (1-17), F_α^h stands for the hydrodynamic resistance, F_α^w is the force related to wettability and volume fraction gradient at around a particle, and F_α^L is the lubrication force working between two particles (Note that the lubrication force can be ignored because of smallness of particles). The hydrodynamic equation is finally given by

$$\rho\frac{\partial v}{\partial t} = \nabla\cdot\left[\eta(r)D\right] - \nabla p - \phi\nabla\mu - \sum_\alpha F_\alpha^w \delta(r - r_\alpha) \tag{1-21}$$

23
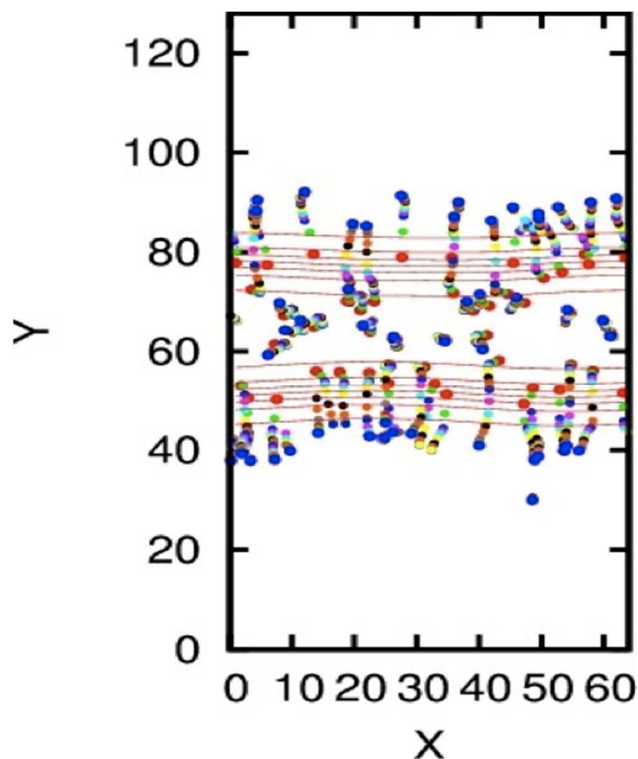
Figure 1-12 Trajectories of particles during migration after quenching from χ=2.5 to 2.3. The X and Y directions are parallel and perpendicular to the surface of a polymer film, respectively. The particles located near the surface in the initial state migrated to the solvent rich-regions. The migration of particles in bulk, on the other hand, is small and does not show a significant amount of surface migrated nanoparticles.

With this model, we performed numerical simulations with a total of 50 particles embedded in the system. We found that the combined use of χ=2.5 and $\Gamma = 0.01$ gave us a good approximation to the original concentration profile of the unexposed polymer after the equilibration. The predicted volume fraction profile of the polymer component is shown in Fig. 1-11 (indicated in red). We then decreased the χ value to 2.3 in order to mimic the swelling ratio of the polymer nanocomposite films (~ 20%) observed experimentally[23] (the blue line in Fig. 1-11). Fig. 1-12 shows the trajectories of the particles as a function of time after changing χ. Colors are indicative of representative times used for the simulations ranging from t=0 to t=2,700 (red corresponds to the original locations of the particles at t=0, while blue corresponds to the ones at t=2,700). Interestingly, the particles near the polymer/solvent interfaces (at around Y=45 and 80) tend to migrate to the fluid-rich regions (Y < 40 and Y > 80) by taking advantage of the concentration gradient there, while the particles far from the interfaces remained within the film. In addition, the results indicate that some of the particles are subsequently coagulated together.

Thus, the simulation results obtained from the simple model well describes the experimental findings.

A challenge in computing for supercritical fluid/polymer nanocomposite systems is to express their P-V-T properties since the two components (fluid and polymer) are quite dissimilar. In fact, the Flory-Huggins model derived for eq. (1-12) is not adequate since the volume change on the mixing is not considered[94]. We are therefore using a hybrid equation of state (EOS) for CO_2-polymer system recently proposed by Shin and Wu[95]. This hybrid EOS combines the Peng-Robinson EOS[96] to represent both molecular excluded-volume affects and van der Waals interactions with the equations from the statistical associating fluid theory (SAFT) model[97] to account for polymer interchain correlations and short-range forces. Their numerical results have shown accurate predictions of the phase behavior of polymer-CO_2 systems including volumetric properties of model polymers even near-critical regions. It is also anticipated that more sophisticated efforts should be carried out to consider plasticization effects of CO_2 on glassy polymers[98, 99] and semicrystalline polymers[100] as well as different shapes of nanoparticles (such as a rod-like shape)[101].

1.3. References

1. McHugh, M. A.; Krukonis, V., *Supercritical Fluids Extraction Principles and Practice*. Woburn, MA: 1994.

2. Brunner, G., *An Introduction to Fundamentals of Supercritical Fluids and their Applications to Separation Processes*. SteinKopft Darmstadt: New York, 1994.

3. *Supercritical Fluid Science: Fundamentals and Applications*. ACS Symp. Ser.: 1993; Vol. 514.

4. DeSimone, J. M.; Guan, X.; Elsbernd, C. S. *Science* **1992**, 257, 945-947

5. Koga, T.; Seo, Y. S.; Zhang, Y.; Shin, K.; Kusano, K.; Nishikawa, K.; Rafailovich, M. H.; Sokolov, J. C.; Chu, B.; Peiffer, D.; Occhiogrosso, R.; Satija, S. K. *Phys. Rev. Lett.* **2002**, 89, 125506

6. Koga, T.; Seo, Y. S.; Hu, X.; Kwanwoo, S.; Zhang, Y.; Rafailovich, M. H.; Sokolov, J. C.; Chu, B.; Satija, S. K. *Europhys. Lett.* **2002**, 60, 559

7. Koga, T.; Seo, Y. S.; Shin, K.; Zhang, Y.; Rafailovich, M.; Sokolov, J.; Chu, B.; Peiffer, D.; Satija, S. K. *Macromolecules* **2003**, 36, 5236

8. Koga, T.; Ji, Y.; Seo, Y. S.; Rafailovich, M. H.; Sokolov, J. C.; Satija, S. K. *J. Polym. Sci, Part B:Polym. Phys.* **2004**, 42, 3282

9. Yamaguchi, H.; Gin, P.; Kobayashi, M.; Bennett, S.; Satija, S. K.; Asada, M.; Koga, T.; A.Takahara. *RSC Adv.* **2013**, 3, 4778-4785

10. Asada, M.; Jiang, N.; Sendogdular, L.; Sokolov, J.; Endoh, M. K.; Koga, T.; Fukuto, M.; Yang, L.; Akgun, B.; Dimitriou, M.; Satija, S. K. *Soft Matter* **2014**, 10, 6392-6403

11. Janssen, R. A.; Nelson, J. *Adv. Mater.* **2013**, 25, 1847-1858

12. DeLongchamp, D. M.; Vogel, B. M.; Jung, Y.; Gurau, M. C.; Richter, C. A.; Kirillov, O.

A.; Obrzut, J.; Fischer, D. A.; Sambasivan, S.; Richter, L. J. *Chem. Mater.* **2005**, 17, 5610

13.   Krebs, F. C. *Org. Electron.* **2009**, 10, 761

14.   Aernouts, T.; Aleksandrov, T.; Girotto, C.; Genoe, J.; Poortmans, J. *Appl. Phys. Lett.* **2008**, 92, 033306-1

15.   Goffri, S.; Muller, C.; Stingelin-Stutzmann, N.; Breiby, D. W.; Radano, C. P.; Andreasen, J. W.; Thompson, R.; Janssen, R. A. J.; Nielsen, M. M.; Smith, P.; Sirringhaus, H. *Nature Materials* **2006**, 5, 950-956

16.   Wei, W.; Nishizawa, T.; Tajima, K.; K., H. *Adv. Mat.* **2008**, 20, 2211-2216

17.   Glogowski, E.; Tangirala, R.; Russell, T. P.; Emrick, T. *J. Polym. Sci. A, Polym. Chem.* **2006**, 44, 5076-5086

18.   Owen, J. S.; Park, J.; Trudeau, P.-E.; Alivisatos, A. P. *J. Am. Chem. Soc.* **2008**, 130, 12279–12281

19.   Zhao, Y.; Thorkelsson, K.; Mastroianni, A. J.; Schilling, T.; Luther, J. M.; Rancatore, B. J.; Matsunaga, K.; Jinnai, H.; Wu, Y.; Poulsen, D.; Fréchet, J. M. J.; Alivisatos, A. P.; Xu, T. *Nat. Mater.* **2009**, 8, 979-985

20.   Tyagi, S.; Lee, J. Y.; Buxton, G. A.; Balazs, A. C. *Macromolecules* **2004**, 37, 9160-9168

21.   Lee, J. Y.; Buxton, G. A.; Balazs, A. C. *Journal of Chemical Physics* **2004**, 121, 5531-5540

22.   Lee, J. Y.; Zhang, Q. L.; Emrick, T.; Crosby, A. J. *Macromolecules* **2006**, 39, 7392-7396

23.   Asada, M.; Gin, P.; Endoh, M. K.; Satija, S. K.; Taniguchi, T.; Koga, T. *Soft Matter* **2011**, 7, 9231-9238

24.   Koga, T.; Jiang, N.; Gin, P.; Endoh, M. K.; Narayanan, S.; Lurio, L. B.; Sinha, S. K. *Phys. Rev. Lett.* **2011**, 107, 225901

25.   Asada, M.; Jiang, N.; Sendogdular, L.; Gin, P.; Wang, Y.; Endoh, M. K.; Koga, T.; Fukuto, M.; Schultz, D.; Lee, M.; Li, X.; Wang, J.; Kikuchi, M.; Takahara, A. *Macromolecules* **2012**, 45, 7098-7106

26.   Gin, P.; Jiang, N. S.; Liang, C.; Taniguchi, T.; Akgun, B.; Satija, S. K.; Endoh, M. K.; Koga, T. *Phys. Rev. Lett.* **2012**, 109, 265501

27.   Jiang, N. S.; Shang, J.; Di, X. Y.; Endoh, M. K.; Koga, T. *Macromolecules* **2014**, 47, 2682-2689

28.   Jiang, N.; Sendogdular, L.; Di, X.; Sen, M.; Gin, P.; Endoh, M. K.; Koga, T.; Akgun, B.; Dimitriou, M.; Satija, S. K. *Macromolecules* **2015**, 48, 1795–1803

29.   Jiang, N.; Endoh, M. K.; Koga, T., Structures and Dynamics of Adsorbed Polymer Nanolayers on Planar Solid. In *Non-Equilibrium Phenomena in Confined Soft Matter*, Napolitano, S., Ed. Springer: 2015; pp 129-160.

30.   Jiang, N.; Wang, J.; Di, X.; Cheung, J.; Zeng, W.; Endoh, M. K.; Koga, T.; Satija, S. K. *Soft Matter* **2015**, DOI: 10.1039/c5sm02435h.

31.   Barnes, K. A.; Karim, A.; Douglas, J. F.; Nakatani, A. I.; Gruell, H.; Amis, E. J. *Macromolecules* **2000**, 33, 4177

32.   Mackay, M. E.; Hong, Y.; Jeong, M.; Hong, S.; Russell, T. P.; Hawker, C. J.; Vestberg, R.; Douglas, J. F. *Langmuir* **2002**, 18, 1877-1882

33.   Wei, B.; Gurr, P. A.; Genzer, J.; Qiao, G. G.; Solomon, D. H.; Spontak, R. J. *Macromolecules* **2004**, 37, 7857−7860

34.   Besancon, B. M.; Green, P. F. *Macromolecules* **2005**, 38, 110-115

35.   Kropka, J. M.; Green, P. F. *Macromolecules* **2006**, 39, 8758-8762

36.   Xavier, J. H.; Sharma, S.; Seo, Y. S.; Isseroff, R.; Koga, T.; White, H.; Ulman, A.; Shin,

K.; Satija, S. K.; Sokolov, J.; Rafailovich, M. H. *Macromolecules* **2006**, 39, 2972-2980

37. Krishnan, R. S.; Mackay, M. E.; Duxbury, P. M.; Pastor, A.; Hawker, C. J.; Horn, B. V.; Asokan, S.; Wong, M. S. *Nano Lett.* **2007**, 7, 484-489

38. Holmes, M. A.; Mackay, M. E.; Giunta, R. K. *Nanopart. Res.* **2007**, 9, 753−763

39. Koo, J.; Shin, K.; Seo, Y. S.; Koga, T.; Park, S.; Satija, S. K.; Chen, X.; Yoon, K.; Hsiao, B. S.; Sokolov, J. C.; Rafailovich, M. H. *Macromolecules* **2007**, 40, 9510−9516

40. Han, J. T.; Lee, G. W.; Kim, S.; Lee, H. J.; Douglas, J. F.; Karim, A. *Nanotechnology* **2009**, 20, 105705

41. Wong, H. C.; Cabral, J. T. *Phys. Rev. Lett.* **2010**, 105, 038301

42. Mukherjee, R.; Das, S.; Das, A.; Sharma, S. K.; Raychaudhuri, A. K.; Sharma, A. *ACS Nano* **2010**, 4, 3709−3724

43. Roy, S.; Bandyopadhyay, D.; Karim, A.; Mukherjee, R. *Macromolecules* **2015**, 48, 373-382

44. Tucker, S. C. *Chem. Rev.* **1999**, 99, 391-418

45. Stanley, H. E., *Introduction to Phase Transition and Critical Phenomena*. Oxford University Press: Oxford, 1971.

46. Eckert, C. A.; Ziger, D. H.; Johnston, K. P.; Kim, S. *J. Phys. Chem.* **1986**, 90, 2738-2746

47. Gates, J. A.; Wood, R. H.; Quint, J. R. *J. Phys. Chem.* **1982**, 86, 4948-4951

48. Eckert, C. A.; Ziger, D. H.; Johnston, K. P.; Ellison, T. K. *Fluid Phase Equilib.* **1983**, 14, 167

49. McGuigan, D. B.; Monson, P. A. *Fluid Phase Equilib.* **1990**, 57, 227

50. Chimowitz, E. H.; Afrane, G. *Fluid Phase Equilib.* **1996**, 120, 167

51. Shing, K. S.; Chung, S. T. *AIChE* **1989**, 34, 1973

52.   Chialvo, A. A.; Cummings, P. T. *AIChE* **1994**, 40, 1558

53.   Nishikawa, K.; Tanaka, I.; Amemiya, Y. *J. Phys. Chem.* **1996**, 100, 418-421

54.   Morita, T.; Kusano, K.; Ochiai, H.; Saitow, K.; Nishikawa, K. *J. Chem. Phys.* **2000**, 112, 4203

55.   Nishikawa, K.; Morita, T. *Chem. Phys. Lett.* **2000**, 316, 238-242

56.   Kamiya, M.; Muroki, K.; Uematsu, M. *J. Chem. Thermodyn.* **1995**, 27, 337

57.   Chen, Z.; Tozaki, K.; Nishikawa, K. *Jpn. J. Appl. Phys.* **1999**, 38, 6840-6845

58.   Carome, E. F.; Cykowski, C. B.; havlice, J. F.; Swyt, D. A. *Physica* **1968**, 38, 307

59.   Eckert, C. A.; Kuntson, B. L.; Debenedetti, P. G. *Nature* **1996**, 383, 313-318

60.   Fleming, G. K.; Koros, W. J. *Macromolecules* **1986**, 19, 2285-2291

61.   Wissinger, R. G.; Paulaitis, M. E. *J. Poly. Sci. Polym. Phys. Ed.* **1987**, 25, 2497-2510

62.   Shim, J. J.; Johnston, K. P. *AIChE J.* **1989**, 35, 1097-1106

63.   Briscoe, B. J.; Zakaria, S. *J. Polym. Sci. : Part B.* **1991**, 29, 989-999

64.   Goel, S. K.; Beckman, E. J. *Polymer* **1993**, 34, 1410-1417

65.   Garg, A.; Gulari, E.; Manke, W. *Macromolecules* **1994**, 27, 5643-5653

66.   Zhang, Y.; Gangwani, K. K.; Lemert, R. M. *J. Supercritical Fluids* **1997**, 11, 115-134

67.   Chang, S. H.; Park, S. C.; Shim, J. J. *J. Supercritical Fluids* **1998**, 13, 113

68.   Royer, J. R.; DeSimone, J. M.; Khan, S. A. *Macromolecules* **1999**, 32, 8965-8973

69.   Koga, T.; Jerome, J. L.; Seo, Y.-S.; Rafailovich, M. H.; Sokolov, J. C.; Satija, S. K. *Langumuir* **2005**, 21, 6157

70.   Koga, T.; Gin, P.; Yamaguchi, H.; Endoh, M.; Sendogdular, L.; Kobayashi, M.; Takahara, A.; Akgun, B.; Satija, S. K.; Sumi, T. *Polymer* **2011**, 52, 4331-4336

71.   Arora, K. A.; Lesser, A. J.; McCarthy, T. J. *Macromolecules* **1998**, 31, 4614-4620

72.   Stafford, C. M.; Russell, T. P.; McCarthy, T. J. *Macromolecules* **1999**, 32, 7610-7616

73.   Omote, K.; Ito, Y.; Kawamura, S. *Applied Physics Letters* **2003**, 82, 544-546

74.   Gin, P.; Asada, M.; Gedelian, C.; Lu, T.; Koga, T. *Appl. Phys. Lett. submitted* **2009**,

75.   Koga, T.; Seo, Y. S.; Jerome, J.; Ge, S.; Rafailovich, M. H.; Sokolov, J. C.; Chu, B.; Seeck, O. H.; Tolan, M.; Kolb, R. *Appl. Phys. Lett.* **2003**, 83, 4309

76.   Koga, T.; Jerome, J. L.; Gordon, C.; Rafailovich, M. H.; Sokolov, J. C. *The Journal of Adhesion* **2005**, 81, 751-764

77.   Koga, T. *Kobunshi Ronbunshu* **2004**, 61, 458

78.   Seeck, O. H.; Kaendler, I. D.; Tolan, M.; Shin, K.; Rafailovich, M. H.; Sokolov, J. C.; Kolb, R. *Appl. Phys. Lett.* **2000**, 75, 2713-2715

79.   Sirard, S. M.; J., Z. K.; Sanchez, I. C.; Green, P. F.; Johnston, K. P. *Macromolecules* **2002**, 35, 1928-1935

80.   Li, Y.; Park, E.; Lim, K. T.; Johnston, K. P.; Green, P. F. *J. Polym. Sci, Part B:Polym. Phys.* **2007**, 45, 1313-1324

81.   Wang, X.; Sanchez, I. C. *Langumuir* **2006**, 22, 9251-9253

82.   Sumi, T.; Sekino, H. *J. Chem. Phys.* **2005**, 122, 194910-1-11

83.   Sumi, T.; Imazaki, N.; Sekino, H. *Phys. Rev. E* **2009**, 79, 030801

84.   Anson, M. L. *Adv. Protein Chem.* **1945**, 2, 361

85.   Asada, M.; Gin, P.; Endoh, M. K.; Satija, S. K.; Koga, T. *Journal of Physics: Conference Series* **2011**, 272, 012013

86.   Lee, J. Y.; Shou, Z.; Balaza, A. C. *Phys. Rev. Lett.* **2003**, 91, 136103

87.   Findenegg, G. H., *In Fundamentals of Adsorption*. Engineering Foundation: New York, 1983.

88.   Blümel, S.; Findenegg, G. H. *Phys. Rev. Lett.* **1985**, 54, 447-450

89.   Strubinger, J. R.; Parcher, J. F. *Anal. Chem.* **1989**, 61, 951-955

90.   Strubinger, J. R.; Song, H.; Parcher, J. F. *Anal. Chem.* **1991**, 63, 98-103

91.   Lal, M.; Plummer, M.; Richmond, N. J.; Smith, W. *J. Phys. Chem. B* **2004**, 108, 6052–6061

92.   Lal, M.; Plummer, M.; Smith, W. *J. Phys. Chem. B* **2006**, 110, 20879–20888

93.   Gin, P.; Asada, M.; Endoh, M. K.; Gedelian, C.; Lu, T.; Koga, T. *Appi. Phys. Lett.* **2009**, 94, 121908

94.   Maloney, D. P.; Prausnitz, J. M. *Industrial & Engineering Chemistry Process Design and Development* **1976**, 15, 216-220

95.   Shin, H. Y.; Wu, J. Z. *Industrial & Engineering Chemistry Research* **2010**, 49, 7678-7684

96.   Peng, D.; Robinson, D. B. *Ind. Eng. Chem. Res.* **1976**, 15, 59-64

97.   Chapman, W. G.; Jackson, G.; Gubbins, K. E. *Molecular Physics* **1988**, 65, 1057-1079

98.   Cao, G. P.; Liu, T.; Roberts, G. W. *J. Appl. Poly. Sci.* **2010**, 115, 2136-2143

99.   Kasturirangan, A.; Koh, C. A.; Teja, A. S. *Ind. Eng. Chem. Res.* **2011**, 50, 158-162

100.   de Paz, E.; Matrtin, A.; Rodriguez-Rojo, S.; Herreras, J.; Cocero, M. J. *J. Chem. Eng. Data* **2010**, 55, 2781-2785

101.   Makino, M.; Taniguchi, T.; Doi, M. *Proc. Int. Conf. Adv. Polym.* **2001**, 171-178

2. Chapter 2: Low-temperature CO_2 annealing for improving crystalline structures and electrical properties of π-conjugated polymer thin films

2.1. Abstract

We propose to use compressed CO_2 gas as a low-temperature and robust plasticization agent to improve structural ordering and preferred chain orientations of π-conjugated polymers on an impenetrable solid surface. Poly(3-hexylthiophene) (P3HT) thin films ($\sim$ 40 nm in thickness) prepared via a spin-casting process on Si substrates were used as a model system. In-situ neutron reflectivity experiments demonstrated that the isothermal swelling curve of the P3HT thin film at 36 °C has a maximum at P=8.2 MPa, the so-called "density fluctuation ridge". In addition, we characterized the P3HT thin films after the density fluctuating CO_2 treatment by using grazing incidence X-ray diffraction. The results are intriguing to show that the in-plane (π-π) stacking of the side chains as well as out-of-plane stacking of the backbone are improved simultaneously, resulting in an increase in the crystalline size that neither conventional thermal annealing nor organic solvent annealing can offer. Finally, we also characterized the electric properties of the CO_2 annealed P3HT thin films. It is known that oxygen molecules interacting with the thiophene ring affect the electrical properties and this influence can be controlled by an O_2 doping level through the polymer morphology. The present results showed that, depending on the CO_2-induced chain mobility, the charge carrier densities and mobilities of the P3HT films can be manipulated.

2.2. Introduction

Directly converting ultraviolet radiation energy from everlasting energy source, Sun to electrical energy, solar cells are ideal and practical systems without toxic by-products. As one type of the most applicable solar cells, simple solution processed organic semiconductor solar cells made of blends of conjugated polymers (donors) and functionalized fullerenes (acceptors) have been extensively studied as an alternative source of electrical energy because of their mechanical flexibility, low-cost fabrication, ease of processing and the miscellaneous approaches to chemical structure from progress in organic chemistry. [6, 7, 16, 21, 40]

In this aspect, among its alternatives the use P3HT has taken precedence as hole transporting material in the most organic field effect transistors (OFETs) and organic photovoltaic cells (OPVs) since the earlier studies showing 1% efficiency for OPVs.[26, 35, 39, 50, 53, 61, 63, 64, 67] To fabricate high-performance devices, high charge carrier mobility of semiconducting polymer (P3HT) is essential of which has been reported earlier to reach comparable levels to amorphous-silicon-based systems (0.1cm2V-1s-1).[60] And device efficiencies reach up to 10% with structural changes on P3HT (donor) material ever since.[5] As Sirringhaus et al.[60] and Kline et al[27] also reported, these electrical properties are strongly influenced with the crystallinity and the morphology of polymer based on regioregularity and molecular weight of the polymer, respectively. In the light of these information, the effect CO_2-P3HT interactions have been scrutinized from different point of views as represented on this chapter.

2.2.1. Chemical and Crystal Structure

A single unit cell of a regioregular poly(3-hexylthiophene) (RR-P3HT) is composed of two monomers which contain two thiophene rings and two head to tail coupled hexyl side groups. Conjugated polymer is the consolidated form of these monomers after polymerization process (Fig. 2-1). As shown by McCullough et. al.[45], configuration of those couplings determines the regioregularity; HH couplings disturb conjugation due to the dimensionally forced twist of the two adjacent thiophenes while cyclic HT couplings introduce continuity to the π-system order with good electrical conductivity. Regioregularity refers to the ratio of HT coupling and can be measured by NMR technique[44].
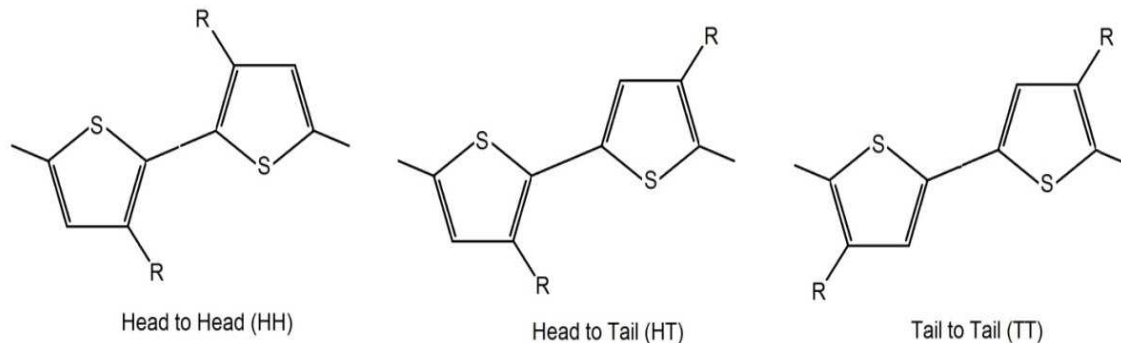
Figure 2-1 Possible regiochemical side group couplings for poly(3-hexylthiophene)

X-ray diffraction and electron diffraction techniques can be useful to analyze crystalline structure (Fig. 2-2), hence earlier selected area electron diffraction (SAED) results suggested the orthorhombic cubic unit structure for P3HT with three different lattice spacings: a=1.66nm, b=0.39nm and c=0.836nm.[23]
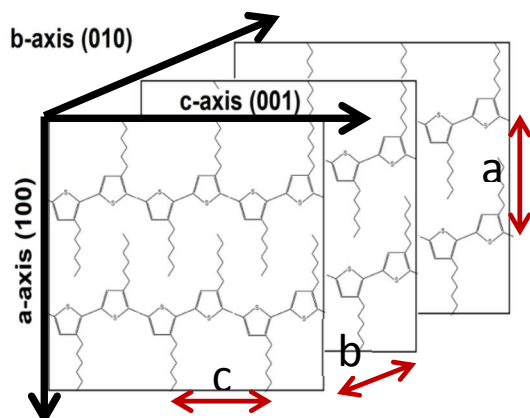
Figure 2-2 Orthorhombic crystal structure of P3HT as deduced from X-ray and Electron Diffraction.

2.2.2. P3HT Meso-Structure from Solution to Solid State

In order to understand the relationship between structure and property of P3HT polymer films, studies on the alignment and morphology of the polymer films after spin or drop casting onto a substrate were reported earlier[8, 9, 45]. Subsequent P3HT film structure growing on a substrate after deposition is influenced by its molecular weight[27], regioregularity[62] and the type of solvent[8] (by solidification rate from wet film), besides polymer substrate interactions which will be explained on the fourth chapter.

According to their responses during film deposition, P3HT polymer can be classified into two different groups: low molecular weight polymer (M_w < 20 kg/mol) and high molecular weight polymer (M_w > 20 kg/mol). It has been showed that higher M_w polymers will be exposed to comparatively longer solvent evaporation times than low M_w polymers due to the changes in evaporation rate introducing better charge carrier mobilities[9].

Another approach was introduced by comparing kinetics from two different solvents with different boiling points (1,2,4-trichlorobenzene (T_b=214°C) and chloroform (T_b=61.2°C)) on low

36

and high molecular weight P3HT polymers by Chang et. al.[8]. And charge carrier mobilities of high M_w polymer were reported to be enhanced with TCB (~10min drying time) compared to chloroform, however solvent dependence on charge carrier mobility was reported as unclear for low M_w polymers. From the following GID and AFM results, they concluded that low M_w polymer always had higher diffraction peaks and the higher degree of crystallinity than high M_w polymer which was inconsistent with charge carrier mobility data. Similar outcome can be seen on the reports from Kline et. al.[27] which explain the lowered mobility with more well defined grain boundaries of low M_w polymers compared to high M_w. It is known that through optical absorption and emission measurements one can calculate the neutral bandwidth of excitons. Chang et. al.[8] also showed that decreased exciton bandwidth was associated with the increased conjugation length. This correlation was explained with higher conjugation length of high M_w polymers inducing higher mobility and by which charge carrier transfer over polymer backbone was improved.

Reitzel et. al.[52] conducted GID experiments on amphiphilic P3HT Langmuir films simply floating on water surface in order to illustrate the self-assembly of conjugated polymers in 2-dimensional crystal forms. Resultant film represented the alignment and structure similar to bulk film with an estimated in-plane coherence length (~5nm) deduced from Scherrer formula[17]. Another related study focused on the same polymer film transferred onto SiO_2 substrate which was then doped with $AuCl_3$ before measuring its surface potential through electrostatic force microscopy (EFM)[18]. And corresponding results showed that the conductive domain sizes were between 200nm and 800nm which is much different than amphiphilic film structure measured on water. And they concluded that those conducting domains are combination of several other sub-domains which explains the enhanced mobility of high M_w polymer while crystallinity seems

reducing by Chang et. al.[8]. It is the possible enhancement of interconnected backbone domains with high molecular weight polymer film; therefore, possible high potential barriers would be avoided at the domain boundaries. Moreover, alternative studies also suggested that thermal annealing based post-deposition treatments can both improve crystallinity and the mobility spontaneously which contradicts with grain boundary based mobility retardation hypothesis[1, 68]. As explained above, higher M_w introduces larger scale π-conjugation regardless of crystallinity which enables charge carriers being transferred along longer polymer chain without interruption by hopping to adjacent polymer over interchain contact, however disoriented backbone confirmations cause fewer interchain contacts which hinders interchain mobility for low M_w polymers[68]. Thermal annealing based mobility improvement suggests that both intrachain and interchain stacking order is enhanced with more planar and ordered polymer backbones.

In conclusion, crystallinity does not explain it all but rather the morphological differences can be more strategical parameter which may control transport properties of P3HT polymer. Since post-deposition treatments induce higher mobility and carrier injection performance with extended π- and π^*-band dispersions, the investigation of the effect of scCO$_2$ on electronic structure has been the driving force for this dissertation.

2.2.3. Post-Deposition Treatment Effect

The structure of P3HT films as studied in X-ray and neutron reflectivity techniques is the combination of the polycrystalline domains encapsulated within the amorphous matrix. Interchain (lamellar) and intrachain (π-π) interactions dominate the crystallinity of π-delocalized conjugated polymer (P3HT), and withal upon film deposition on to substrate through spin casting process these weak interactions form microscopic defects, disordered structures and stressed

locations, which inhibit thin film's optical and electrical properties. On that account, versatile post-deposition treatments have been proposed to improve those interchain and intrachain molecular order of which consequences were the enhanced electrical properties of the conjugated polymer.[22, 25, 69, 70] However, applicability of these post-deposition processes are limited to some extend such as incompatibility of high temperature thermal annealing for flexible solar cells on substrates with low glass transition temperatures and inefficiency of solvent annealing onto large scale applications.

For this reason, we propose the use of supercritical carbon dioxide ($scCO_2$) as an innovative polymer friendly approach offering more flexible process parameters and robust control over polymers' electronic structures with low application temperatures; one can control the interactions between the polymer and the CO_2 by simply varying external parameters such as temperature, pressure and exposure time. In this case, we would like to focus attention on density fluctuation ridge.

Among supercritical fluids CO_2 was chosen due to its moderate critical point of $Tc = 31.3°C$ and $Pc = 7.38MPa$ which possesses coexistence curve of liquid and gaseous phases in the phase diagram close to the room temperature. And because of the solvent density fluctuations around the coexistence curve, $scCO_2$ miscibility with thin films of even immiscible bulk polymers is exponentially enhanced.[29-32]

Thermodynamics and kinetic processes that take place after $scCO_2$ sorption within polymer are quite different than the conventional annealing method. Basically, changes in thermal properties such as decreased glass transition temperature, increased polymer viscosity and withal increased chain diffusivity due to the increased free volume after $scCO_2$ sorption enable the regeneration of polymer structure to the desired level of crystallinity order. [11, 32, 54]

As stated earlier, organic semiconductor solar cells are complex systems; therefore, in this study we have solely focused on polymer/scCO$_2$ interactions to construct basic understanding and to eliminate complexity before incorporating fullerene component. Choosing P3HT (widely used in BHJ systems with fullerene) as a target polymer, we aimed to collect in-situ and ex-situ data about scCO$_2$/P3HT interactions on different process conditions of which could be helpful to relate the morphology with the electrical properties of the polymer.

2.3. Experimental Section

2.3.1. Sample Preparation

A regioregular P3HT was purchased from American Dye Source Inc. with a number-average molecular mass M$_n$=69kDa and the approximate regioregularity of 96%. The polymer was dissolved in a good solvent (chlorobenzene) with a fixed polymer concentration (1wt %). The polymer solution was heated at 60˚C for at least 3h before filtering the solution using a PTFE syringe filter (a 0.45μm pore-size). The bulk glass transition temperature (T$_g$) and melting temperature are estimated to be 12 °C and 239 °C, respectively. Silicon disks (3-inch diameter and 8-mmthickness) for NR and silicon wafers (1×1 cm^2 and 0.5-mm thickness) for GD experiments were placed in piranha solutions (i.e., a mixture of H$_2$SO$_4$ and H$_2$O$_2$, *caution: a piranha solution is highly corrosive upon contact with skin or eyes and is an explosion hazard when mixed with organic chemicals/materials; Extreme care should be taken when handing it*) at T=373 K for 30 min. The wafers were rinsed with deionized water and subsequently submersed in an aqueous solution of hydrogen peroxide (HF) for 1min to remove a native oxide layer (SiOx) on Si substrates. However, it should be noted that we confirmed that a SiO$_2$ layer of about

1.3 nm in thickness was reproduced even just after hydrofluoric acid etching due to atmospheric oxygen and moisture, as reported previously[57]. The filtered P3HT solution was then spun cast onto the HF-etched Si wafers at room temperature with a rotation speed of 2500 rpm, giving the thickness of about 40nm P3HT thin films. Finally, the spin-coated P3HT thin films were kept under vacuum at room temperature (25°C) for 24h to remove residual solvent molecules.

As will be discussed later, the NR experiments demonstrate that CO_2 exposure at the ridge condition (i.e., P = 8.2 MPa and T = 36 °C) for 24 h is satisfactory to achieve a final self-assembled structure of the P3HT chains. After the CO_2 exposure, the chamber was rapidly quenched to atmospheric pressure within 10 s (i.e., a quench rate of ca. 50 MPa/min) or slowly (i.e., a quenching rates of ca. 0.15 MPa/min). At the same time, as controls, we treated the P3HT thin films via conventional high temperature annealing at 170 °C for 24 h, followed by rapid quench to room temperature.

2.3.2. In-situ Neutron Reflectivity (NR)

With a large penetration depth, neutron reflectivity (NR) is an ideal tool to determine the *in situ* thickness, composition, and interfacial structure of polymer thin films immersed in fluids or gases, under high pressure in thick walled vessels[31, 58]. The *in-situ* swelling behavior of the P3HT thin films in CO_2 was measured by NR. P3HT thin films with the average thicknesses of 40 nm were prepared on 3-inch H-Si wafers. The specular NR measurements were performed at the NG-7 reflectometer, the National Institute of Standards and Technology Center for Neutron Research. The wavelength (λ_N) of the neutron beams was 0.47 nm with $\Delta\lambda_N/\lambda_N$ = 2.5 %. The details of the high-pressure NR experiments and high-pressure cell have been described elsewhere[31]. The NR

experiments were conducted under the isothermal condition (T = 36 °C) with elevated pressures up to P = 10.0 MPa. Temperature and pressure stabilities during the NR measurements were within an accuracy of ± 0.1°C and ± 0.2 %, respectively. The P3HT thin films were exposed to CO_2 for up to 1 h prior to data acquisition. The scattering length density (*SLD*) values of CO_2, which vary from 0.0004×10^{-4} to 1.75×10^{-4} nm^{-2} in the pressure range of 0.1 MPa < P < 10.0 MPa at T = 36 °C, were calculated based on the density of CO_2 obtained by the equation of state[20]. The SLD value of the bulk P3HT (the density of 1.1 g/cm^3) is calculated to be 0.0022×10^{-4} nm^{-2}. The NR data was obtained by successively increasing the pressure and then slowly decreasing the pressure. Since the background scattering from a pure CO_2 phase increases dramatically near the critical point[31, 32], we measured the scattering from the pure fluid phase (i.e., the long-range density fluctuations) for the respective pressure condition. The NR data corrected for the background scattering was analyzed by comparing the observed reflectivity curves with the calculated ones based on model *SLD* profiles having three fitting parameters for each layer: film thickness, *SLD*, and roughness between the CO_2 and polymer layers represented as a Gaussian function[55]. To ensure conservation of the mass of the polymer for the NR data fitting, the volume fraction profiles were calculated such that the amount of the polymer chains remained the same at all solvent concentrations including in the dry state (i.e., before CO_2 exposure).

2.3.3. Grazing incidence X-ray diffraction (GID)

Grazing incidence x-ray diffraction (GID) measurements for the CO_2-treated and thermally annealed PEO thin films were carried out at the X9 beamline (λ=0.0918nm and

E=13.5keV) at the National Synchrotron Light Source (NSLS), Brookhaven National Laboratory (BNL). Two dimensional diffraction patterns were measured with a CCD camera (Princeton Instruments) with two different incident x-ray angles (θ) of 0.08 and 0.16°, which are below and above the critical angle of P3HT (θ_c=0.12) at the x-ray wavelength of 0.0918 nm. All GID experiments were carried out at room temperature under vacuum and the exposure time for all the measurements was set to 300 sec.

2.3.4. Atomic Force Microscopy (AFM) measurements

The surface morphologies of the P3HT thin films were observed by atomic force microscope (AFM) (Digital Nanoscope III and Bruker Bioscope Catalyst). Both contact mode and standard tapping mode were conducted in air using a cantilever with a spring constant of 0.06 N/m and 40 N/m, respectively. The scan rate was 0.5 Hz or 1.0 Hz with the scanning density of 256 or 512 lines per frame.

2.3.5. Polarized Optical Microscopy (POM) Measurements

Polarized optical microscopy (POM) measurements were conducted by using reflective light under an Olympus BHT Microscope equipped with a differential interference contrast attachment for incident light after Nomarski (NIC Model). POM images were captured by a digital camera under polarized light at room temperature.

2.3.6. Device Electrical Measurements
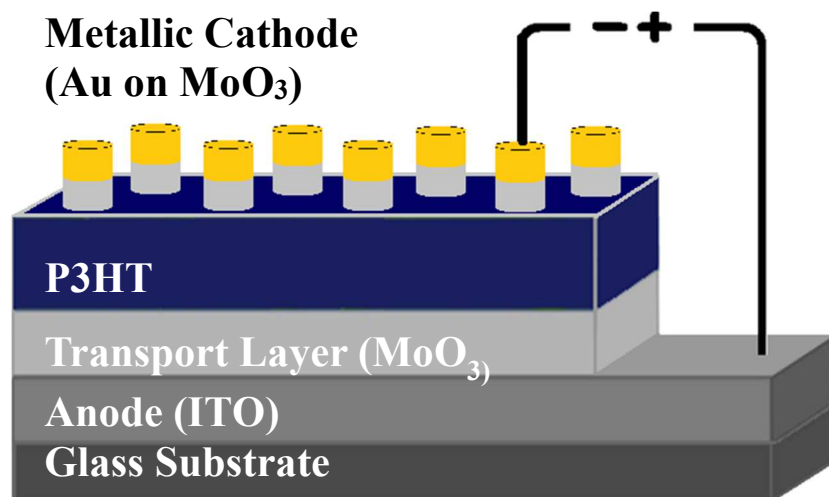
Figure 2-3 Representative device configuration fabricated for pure P3HT hole conductivity measurements.

For device samples, P3HT-chlorobenzene solution were spin casted onto 100nm-thick MoO_3 transport layer deposited by thermal evaporation (Lesker PVD 75) at ~$5*10^{-7}$Torr on to ITO-glass substrate. Each sample were then either thermally annealed or scCO2 exposed at designated conditions. And as also illustrated in fig.2-3,~40nm-thick treated P3HT films were finally ready for SCLC mobility measurements after depositing another 100nm- thick MoO_3 transport layer and 100nm-thick Au layer deposited by thermal evaporation (at ~$5*10^{-7}$Torr), respectively.

J-V characterization for $scCO_2$ and thermally annealed 40nm P3HT films were performed in the Center for Functional Nanomaterials at BNL. J-V performance of post-deposition treated devices was obtained by using Agilent 4156C precision semiconductor parameter analyzer. Each device were repeatedly exposed to forward (Au contact is biased negatively) and reverse (Au contact is biased positively) biasing in order to examine heterogeneous structure of $scCO_2$ exposed samples (as observed in GID results) perpendicular to the substrate surface. Electrical

properties were calculated by fitting both forward and reverse J-V profiles to the SCLC and Ohmic model.

2.4. Results

2.4.1. In situ NR results

Fig. 2-4(a) shows the in-situ NR profiles for the 43 nm thick P3HT thin film at the four different pressures and T=36 °C. The solid lines correspond to the best-fits to the data based on the volume fraction profiles of the polymer, $\Phi(z)$, shown in Fig. 2-4(b). It should be noted that contributions from the density fluctuations of the pure CO_2 phase become significant near the ridge condition ($P = 8.2$ MPa at T $= 36$ °C) and overwhelms the observed intensity at $q_z > 0.06$ Å^{-1}[31, 32].
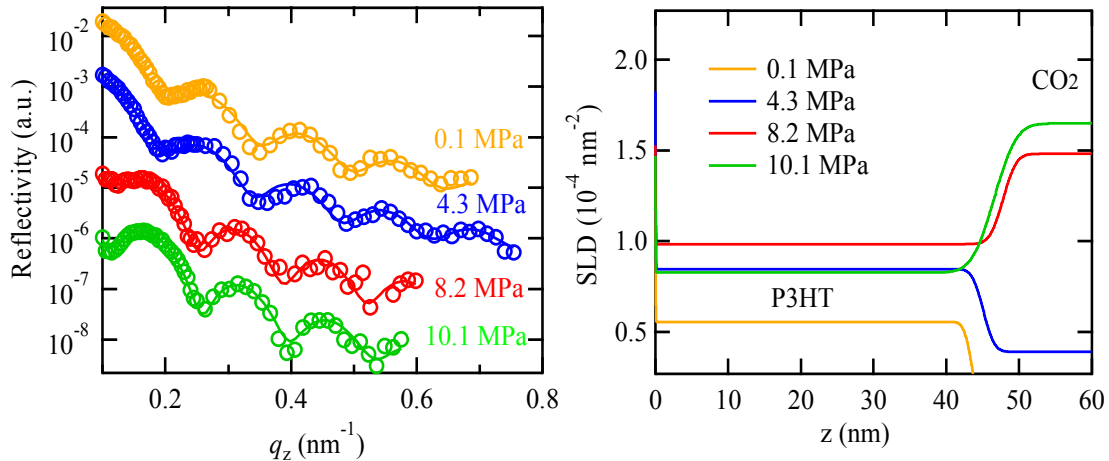
Figure 2-4 (a) NR profiles for the 43 nm thick P3HT film at the four different pressures and T $= 36$ °C. The solid lines correspond to the best-fits to the data based on the corresponding SLD profiles shown in (b).

Fig. 2-5 summarizes the linear dilation (S_f) of the 43 nm thick film during the pressurization process. The S_f values were calculated by the equation, $S_f = (L_1 - L_0) / L_0$,

where L_1 and L_0 are the measured thicknesses of the swollen and unswollen film, respectively. In the pressurization process, there is an anomalous peak in S_f near $P = 8$ MPa that is attributed to the excess sorption of CO_2 molecules at the "density fluctuation ridge" [28-32, 41, 42, 48, 59] where the density inhomogeneity of CO_2 molecules becomes maximum[51]. Intriguingly, in the depressurization process, the S_f value decreased gradually to 0.075 at $P = 0.1$ MPa, as previously seen in the PEO thin film[4]. Hence, it is clear that the swollen PEO thin film just after the depressurization is in the non-equilibrium state. However, we confirmed that the swollen structures were stable at least for 1 month at room temperature.
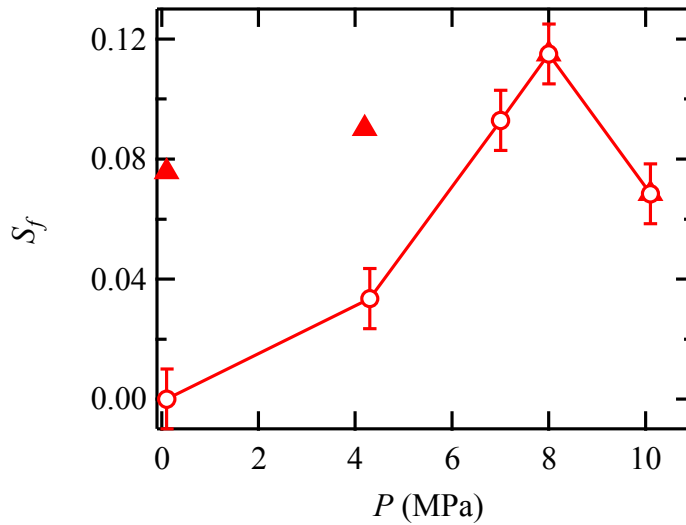
Figure 2-5 Linear dilation of the P3HT thin film as a function of pressure at T=36°C. The circles correspond to the data in the pressurization process, while the triangles correspond to the data in the depressurization process.

In addition, we also studied the effect of the CO_2 exposure time at the ridge condition on the swelling behavior. As shown in Fig. 2-6, the linear dilation gradually

decreased and saturated at S_f=0.02 after the exposure time of 20h. This will be further discussed in the GID results.
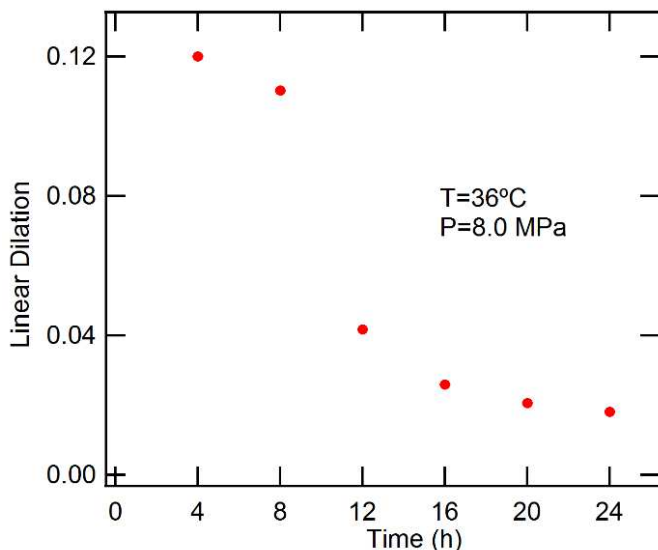
Figure 2-6 Exposure time dependence of the linear dilation of the P3HT thin film at the density fluctuation ridge condition.

2.4.2. GID results

Based on the in-situ NR experiments, we found that the plasticization effect of CO_2 is maximized at the ridge condition. Here we further characterize the CO_2 annealing P3HT thin films (fixed original film thickness of 43 nm) by quenching them from high pressure CO_2 to atmospheric pressure with two different depressurizing rates of CO_2 gas. Goel and Beckman used a similar CO_2 process to establish a foaming method in which the bulk polymer is saturated with supercritical CO_2 followed by rapid depressurization[14, 15]. However, as previously reported[13], the CO_2 process used in the present study generates only molecular scale porosity (the average size of 0.8 nm) with a relatively broad size distribution. The lack of large voids in the P3HT films after the CO_2 process may be due to the short diffusion path for residual CO_2 and/or the high diffusivity of CO_2 in the P3HT matrix.
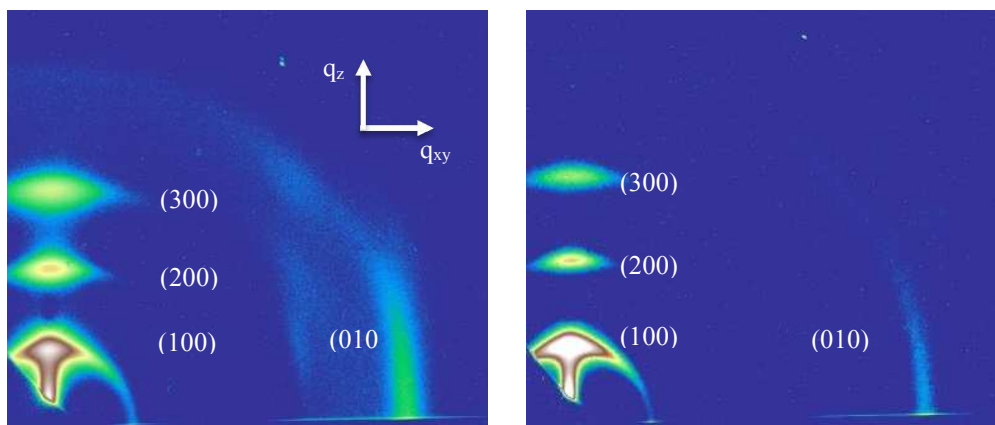
Figure 2-7 2D GID images for the CO_2 treated P3HT thin film (the original thickness of 43 nm) after expose to CO_2 at the ridge condition for 24h: (left) surface region; (right) entire film region.

Fig. 2-7 shows representative 2-d GID images of the CO_2-treated P3HT films that were exposed to CO_2 at the ridge condition for 24h. The abscissa is in the plane of the substrate (q_{xy}) and the coordinate is perpendicular to the substrate (q_z). The appearance of the well-defined (100), (200), and (300) peaks along the q_z direction, rather than rings of scattering, and (010) peak in the q_{xy} direction are seen in all the GID images of the CO_2-treated P3HT films in both the surface and film modes.
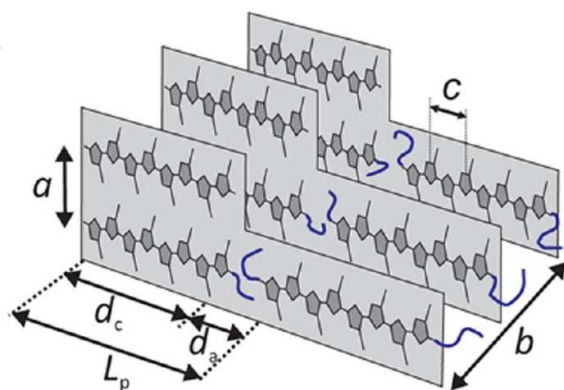
Figure 2-8 Schematic view of the regioregular P3HT crystalline structure. *a*, *b*, *c* represent the crystal lattice constants: d_e and d_c are the thickness of the crystal and amorphous lamellae, respectively. Data from Kohn et. al.[34]

Ellipsometry (Rudolf Auto EL-II) experiments with a fixed refractive index of 1.45 gave the thicknesses of 44 nm for the exposed P3HT films regardless of a choice of the quench rates.
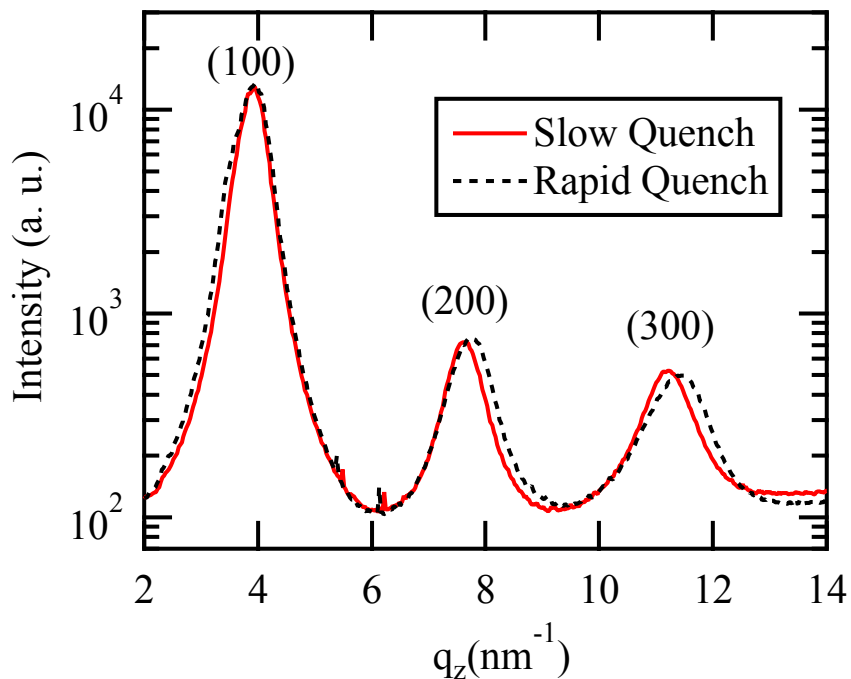
Figure 2-9 GID profiles to study the effect of quench ratios on the resultant backbone packing structures.

In addition, as shown in Fig. 2-9, the 1d GID profiles between the slow quenched and rapid quenched films are in good agreement with each other, while the peak positions of the (200) and (300) reflections for the rapid quenched film are slightly off. As we previously reported for semicrystalline PEO thin films, the slow depressurization process (the quench rate of 0.15 MPa/min) provokes more highly ordered crystalline structures with large grain sizes when the CO_2-polymer mixture is melted prior to the quench[4, 66]. Hence, we postulate that the P3HT chains do not melt even at the ridge condition, which is consistent with a previous result[36] and the present NR results demonstrate that the linear dilation is only 0.12 at the ridge condition (the

S_f values of the exposed PEO thin films (16 ~ 78 nm in thickness) are about 0.5[4]).
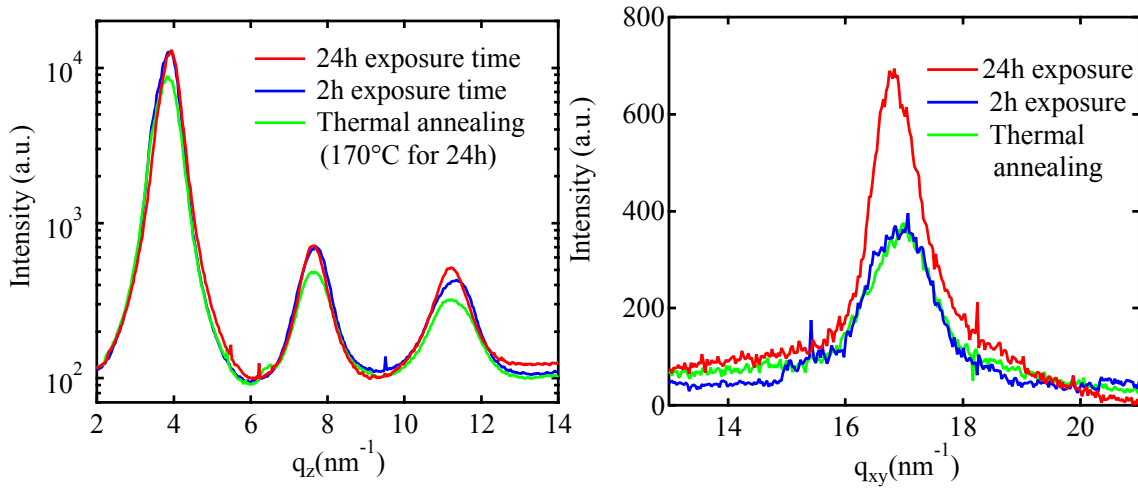
Figure 2-10 GID profiles of the P3HT thin film (the original thickness was 43 nm) along (left) the q_z and (right) q_{xy} directions after the CO_2 annealing at the ridge condition and thermal annealing.

By simple analysis of the 1d scattering profiles using a Gaussian function, the peak position, peak intensity, and peak width were obtained. The lattice constants $a=2\pi/q_{z,0}$, and $b=2\pi/q_{xy,0}$ (Fig.2-8)[34] were calculated, and the Scherrer equation ($L=(K\lambda)/(\beta\cos\theta)$, K is the crystallite shape factor (=0.9), β is FWHM, θ is the scattering angle)[56] was further used to obtain the crystalline size (L). With these parameters, we highlight the novel features of the "density fluctuating" CO_2 annealing at the ridge. Fig. 2-10 shows the CO_2 exposure time dependence of the GID profiles along the q_z and q_{xy} directions for the CO_2 treated P3HT thin films at the ridge condition. As a comparison purpose, we also plot the GID results for the P3HT 40 nm thick film.

From the figures, the backbone chain orientation along the z direction improves significantly with the CO_2 annealing at the ridge condition as compared to that with thermal annealing at 170 °C for 24h, while the GID profiles between 2 h exposure time and 24 h exposure time remained nearly identical. We also found that the lattice constant of the P3HT

(i.e., the intermolecular backbone distance) remained unchanged (a =1.62 nm). In addition, the CO_2 annealed film at the ridge for exposure time of 2h gives L=10.8 nm. This corresponds to about 7 layers whereas for 24 h exposed sample, L= 12.4 nm that corresponds to 8 layers. It should be emphasized that these sizes are larger than that of the thermally annealed film (at 170 °C for 24h, L= 9.1 nm). On the other hand, in the lateral direction, the (010) reflection, which corresponds to the intermolecular π-π stacking plane distance, becomes intensified after 24 h exposure of CO_2 at the ridge condition, which can't be achieved by conventional thermal annealing or short CO_2 exposure treatment (Fig. 2-10). Similar improved π-π stacking along the in-plane direction via solvent annealing was recently reported by Kim and co-workers[24]. They used binary mixtures of aliphatic and aromatic organic solvents to simultaneously dissolve the rigid aromatic backbone and alkyl chains at the 3-positions of the thiophene of the P3HT chains.

Hence, we conclude that the density fluctuating CO_2 annealing play a role as a robust plasticization agent to prompt the chain mobility and hence improve the chain orientations of both the backbone and side chains of the π conjugated polymer effectively.
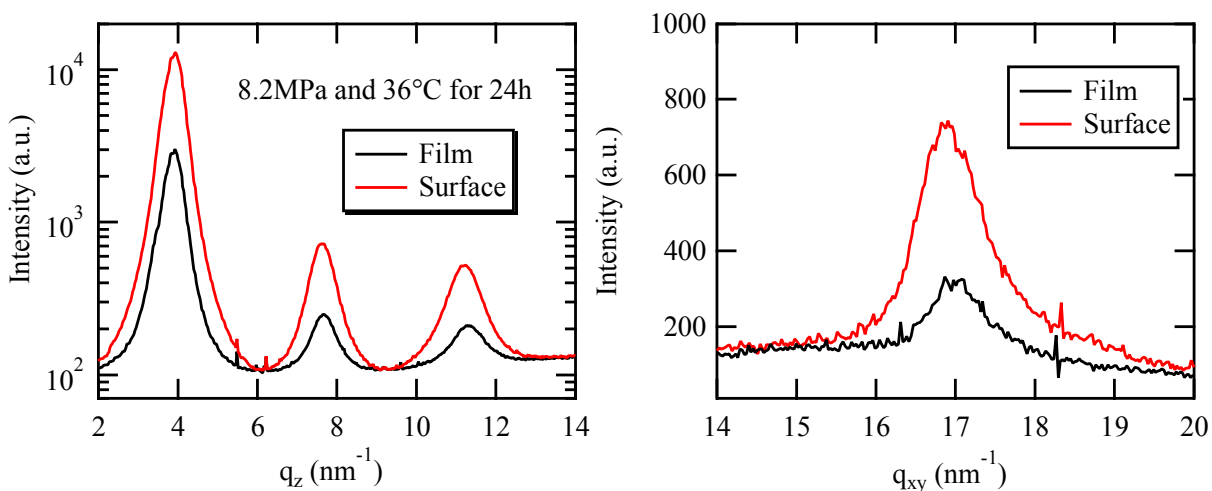
Figure 2-11 GID profiles of the P3HT thin film (the original thickness was 43 nm) along (left) the q_z and (right) q_{xy} directions after the CO_2 annealing at the ridge condition.

There is another unique feature of the CO_2 annealing at the ridge. Fig. 2-11 shows the 1d GID profiles along the q_z and q_{xy} directions in the surface region (the topmost about 10 nm) and bulk film region of the P3HT thin film after the CO_2 annealing at the ridge for 24h. Their 2d images are also shown in Fig. 2-7. It is clear that the multiple peak intensities from the surface region are much higher than those of the entire film region, indicating that the backbone orientation at the surface region is more ordered relative to that of the entire film. In addition, the crystalline size at the surface region is much larger (L=12.4 nm) than that of the entire film (L=9.9 nm). Moreover, the peak intensity of the in-plane (010) reflection at the surface region is about 4 times higher than that of the entire film. These experimental results are consistent with the characteristic of the density fluctuating CO_2 annealing: this anomalous CO_2 absorption is a surface effect due to the limited penetration depth of the density fluctuating CO_2 molecules in a viscous polymer matrix[3, 13, 31-33]. In the next chapter, we discuss the structure-conductivity relationship.

2.4.3. Conductivity Results: I-V Characteristics of Thermal Annealled and scCO₂ Exposed Pure P3HT

Device electrical measurements represented in this section is the summary of P3HT hole conductivity experiments on the two-probe measurements. Fig. 2-12 shows corresponding current-voltage (I-V) studies of the thermal and CO_2 treated P3HT devices on Au and MoO_3 electrodes at dark ambient conditions.
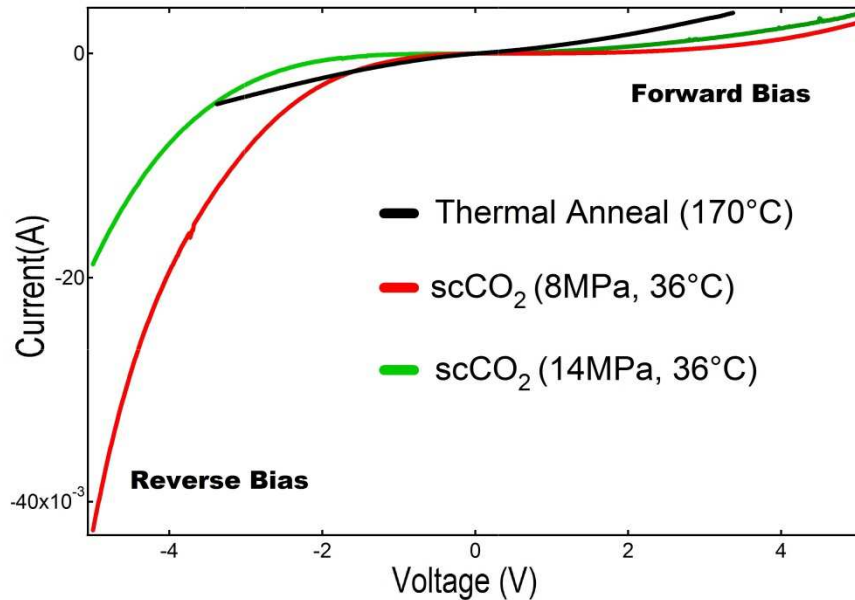
Figure 2-12 Two-probe I-V data of 24h thermal and scCO2 annealed 40nm P3HT films. Voltage range for thermal annealing samples is limited to -3<V<3, while the voltage range for scCO$_2$ samples is -5<V<5

From this data, we realized that the CO$_2$ treated samples exhibit Ohmic and space charge limited conductivity (SCLC) at low and high applied voltages, respectively; however, this transition is less clear for the thermal annealed samples. The thermal annealed samples were electrically shorted at bias voltages over 3V while the CO$_2$ samples were stable up to 5V on both forward and reverse biasing which can be due to expended film thickness and structural stability of CO$_2$ samples[10].

In fabricated organic semiconductor thin films like P3HT, the existence of trap states localized in the bandgap even after the tempering is well documented before[19, 65], and the structural and morphological defects, disorders and impurities define the distribution of these gap states through the bulk film which affects device electrical properties. Hence sufficiently understanding and controlling the distribution of these defects is critical importance; therefore,

earlier studies on organic semiconductors are reported on the direct fitting of SCLC behavior to charge transport models by scanning through trap distribution[5, 50].
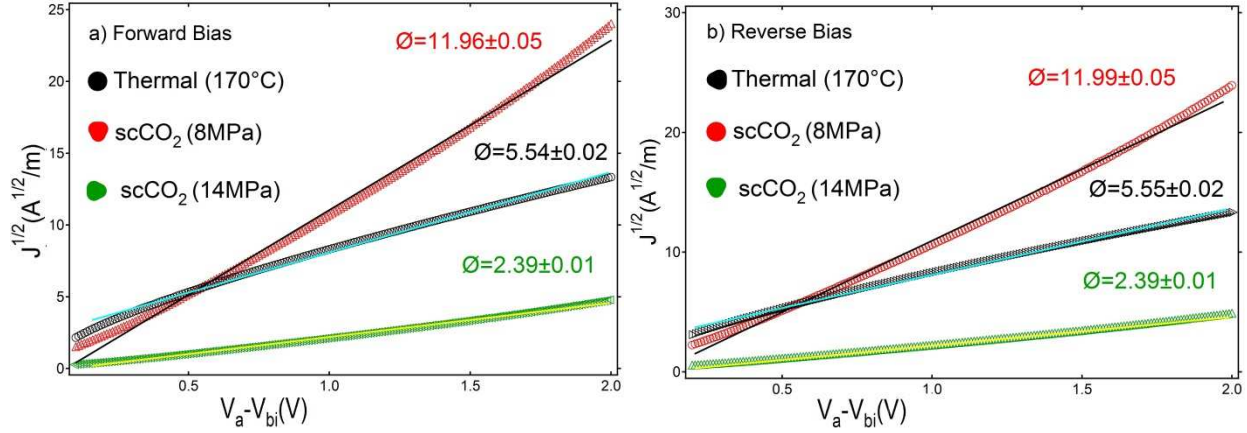
Figure 2-13 Low voltage $J^{1/2}$-V characteristics of 24h annealed CO_2 (36°C) and thermal (170°C) MoO3-P3HT-MoO3-Au devices a) forward bias (Au is biased negatively) b) reverse bias (Au is biased positively).

For the trap density dependent hole transfer through P3HT network, applied voltage is found to be linearly increasing with the square root of current density ($J^{1/2}$) (Fig. 2-13), where we can apply renowned Mott-Gurney equation[38]:

$$J = \left(\frac{9}{8}\right) \varepsilon_0 \varepsilon_r \mu \left(V^2/d^3\right) \qquad (2\text{-}1)$$

where μ is the charge carrier mobility, ε_0 is the free-space permittivity, ε_r is the dielectric constant of the semiconductor, V is the applied voltage, and d is the thickness of the semiconductor layer. SCLC mobility results are listed in Table 1(f) which shows enhancement around ridge condition.
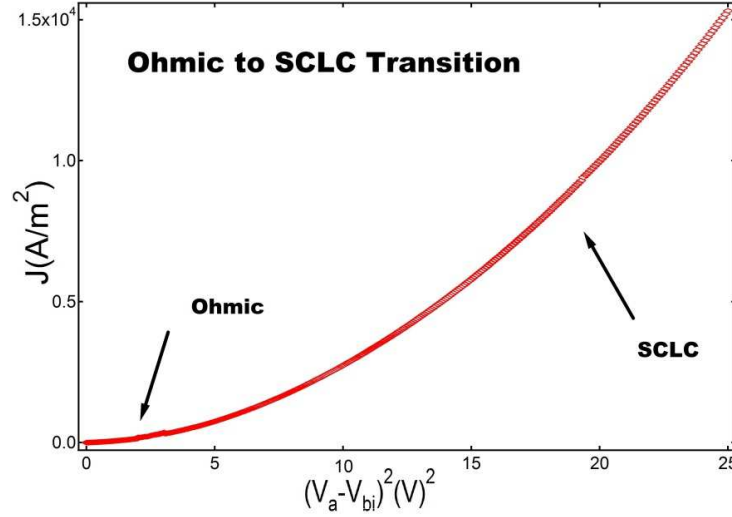
Figure 2-14 . I-V^2 plot for 40nm thick P3HT on Au and MoO_3

To simply point out the transition, current is plotted as a function of the second power of applied voltage (V^2) in Fig 2-14.

Modifications to eq.(2-1) have been derived to be able to consider the effect of excess charge carriers injected from the electrode to semiconductor which is the magnitude of eq.(2-1)[49]:

$$J = ne\mu \left(\frac{V}{d}\right), \qquad (2\text{-}2)$$

$$n_{SCLC} = \frac{9}{8} \frac{\varepsilon_0 \varepsilon_r}{e} \frac{V}{d^2} \qquad (2\text{-}3)$$

Extrapolated transition voltages (V_{th}), which is directly proportional to the charge carrier concentration, are shown in Fig. 2-15 and the corresponding charge carrier concentrations (n_{SCLC}) calculated from eq.(2-4) are listed in table 1(a). Comparative results from Fig 2-15(a) and Fig. 2-15(b) suggest that V_{th} decreases with the use of $scCO_2$ and reaches to its minimum around density fluctuation ridge with decreasing n_{sclc} (table 1(a)).
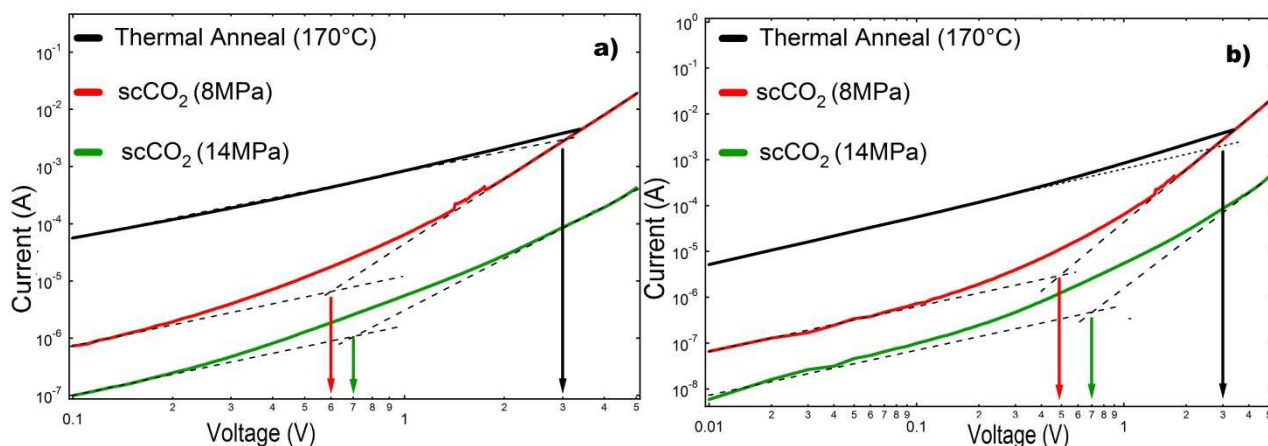
Figure 2-16 Double logarithmic I-V plots of the 24h CO_2 (36°C) and thermal (170°C) annealed P3HT devices a) Forward bias, where Au is biased negatively with respect to MoO_3 b) Reverse bias, where Au is biased positively with respect to MoO_3

Shifts in transition voltages are dependent on the CO_2 induced mobility which promotes higher order structure [36]along with a decrease in the oxygen doping amount as explained on earlier reports [43, 47, 49]which suggest that scCO$_2$ induced higher chain mobility allows to the higher extent of detrapment of molecular oxygen (O_2), which exist as hole dopant in P3HT. These oxygen molecules interact with thiophene ring, and in return they directly control n_{ohmic} and charge mobility (μ) through a charge transfer mechanism[2, 46].
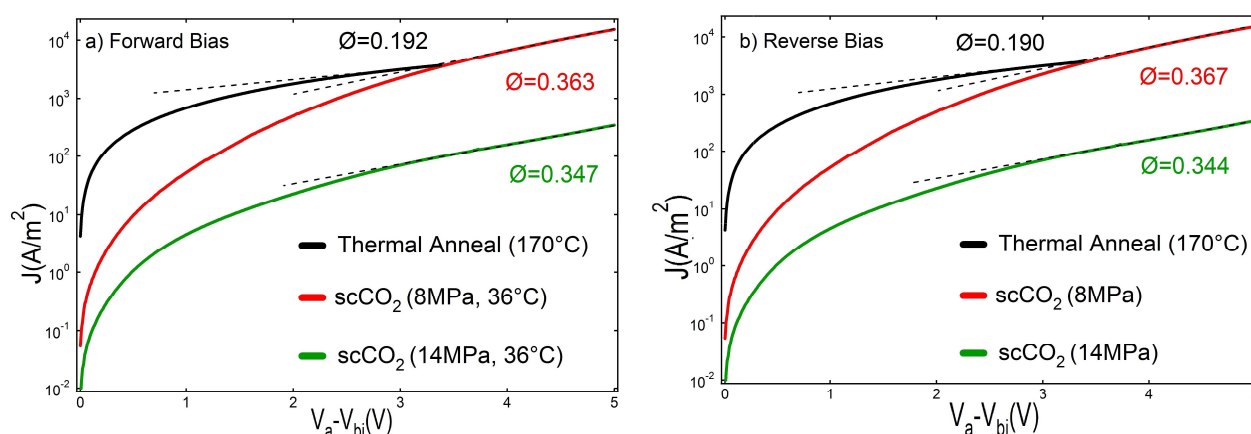
Figure 2-15 Log J-V plots of the 24h CO_2 (36°C) and thermal (170°C) annealed P3HT devices of which slopes are proportional to defect sizes a) Forward-bias (hole conduction from substrate interface to air interface) b) Reverse-bias (hole conduction from air interface to substrate interface)

Another aspect of using CO_2 is the heterogeneity developed along out of plane direction which can be observed from I-V profile. While thermal annealing samples are free of applied bias direction dependence, the CO_2 samples show some difference in the magnitude of charge carrier concentration from each direction. This is the most likely due to the chain mobility difference perpendicular to the substrate surface as a function of excess CO_2 adsorption around density fluctuation ridge on the polymer-air interface[29, 32, 42]. And comparative results in Table 1 suggest that polymer chain mobility is higher close to polymer-air interface where reverse biasing (conduction direction from air interface to substrate interface) introduces higher dopant detrapment.

Fig. 2-16 shows the current density-voltage characteristics of P3HT devices and for scCO2 treated samples strong bias dependence of the current is remarkable. One possible explanation to this is the Poole conduction: similar to Poole-Frenkel conduction, Poole conduction also considers effects of trap sites; however in Poole conduction trap site density is accepted to be higher with shorter distance between adjacent trap sites[12]. This correlation is expressed as:

$$J \; \alpha \; \exp(\frac{q S poole}{2kT} \frac{V}{d})\qquad\qquad (2\text{-}4)$$

Where S_{poole} is the distance between the adjacent trap centres and as provided in table 1 cubic inverse of trap distances give trap densities ($N_T = S_{poole}^{-3}$). Consistent with GID data, lower charge trap densities of the $scCO_2$ treated P3HT films (table 1) over thermally annealed counterparts suggest that the CO_2 process induces more significant chain mobility and the mobility reaches to its maxima at ridge supported with longer trap distances and lower trap densities.

I-V^2 plot is averted from linearity (SCLC) at low voltage where Ohmic conduction is dominant (Fig. 2-14). This deviation is caused by the substantial bulk free carriers in low bias regime. And at the transition point from Ohmic to SCLC conductivity there exists a threshold voltage which were originally explained by Lampert[37]:

$$n_{SCLC} = n_{Ohmic} = \frac{9}{8} \frac{\varepsilon_0 \varepsilon_r}{e} \frac{V_{th}}{d^2}$$
(2-5)

Regardless of treatment method, linearity of J-V curve were also observed at low applied voltage (0<V<2V) where ohmic conduction was calculated from:

$$\sigma = \frac{J}{E} = \frac{J}{V} t, \ E = V/t$$
(2-6)

where σ is ohmic film conductivity, E=V/t is the electric field and t is the film thickness. And then we can find ohmic mobility (V<V$_{th}$) since both ohmic conductivity and the bulk free carrier density (n$_{ohmic}$) at V$_{th}$ is known:

$$\mu = \sigma/(n * e)$$
(2-7)

Corresponding ohmic mobilities as shown in table 1(e), and negligible changes can be observed compared to SCLC mobility results which is due to the electric field influence[49]; however, results are reasonably following the same trend with SCLC mobility extracted from eq.(2-1) and the same trend with injected charge carrier concentration (table 1(a)) results continues with the use of CO_2.

In conclusion, we demonstrated that the dopant (O_2) in disordered P3HT forms a charge transfer complex which is responsible for free charge carrier generation for the π-conjugated polymers exposed to ambient conditions. In addition, the competition between free charge carriers and injected charge carriers can be observed through SCLC theory which also helps us investigate trap densities. Moreover, the light and heating under vacuum[43, 47], we propose an alternative CO_2 method which controls the p-type doping by inducing higher chain mobility in P3HT. In return, we found that CO_2 exposure at around density fluctuation ridge provides the higher extent of O_2 molecule detrapment which gives higher charge carrier mobility results.

Table 2-1 Calculated charge carrier concentrations, defect sizes and defect densities and the mobility data for thermal and $scCO_2$ samples

	Forward Bias **Reverse Bias**	**Thermal** **(170°C, 24h)**	**scCO$_2$** **(8MPa, 36°C, 24h)**	**scCO$_2$** **(14MPa, 36°C, 24h)**
a)	n_{SCLC} **(cm^{-3})**	$>34.8*10^{16}$ $>34.8*10^{16}$	$6.96(\pm0.04)*10^{16}$ $5.68(\pm0.07)*10^{16}$	$8.23(\pm0.03)*10^{16}$ $8.12(\pm0.09)*10^{16}$
b)	S_{poole} **(nm)**	$0.394(\pm0.02)$ $0.390(\pm0.02)$	$0.746(\pm0.03)$ $0.755(\pm0.02)$	$0.713(\pm0.02)$ $0.707(\pm0.02)$
c)	$N_{T,Spoole}$ **(cm^{-3})**	$16.349(\pm2.2)*10^{21}$ $16.858(\pm1.8)*10^{21}$	$2.409(\pm0.28)*10^{21}$ $2.323(\pm0.18)*10^{21}$	$2.759(\pm0.24)*10^{21}$ $2.829(\pm0.27)*10^{21}$
d)	σ **(S/cm)**	$3.51*10^{-7}$ $3.51*10^{-7}$	$3.32*10^{-7}$ $2.42*10^{-7}$	$0.15*10^{7}$ $0.14*10^{-7}$
e)	μ_{ohmic} **(cm^2/Vs)**	$0.63*10^{-5}$ $0.63*10^{-5}$	$2.98*10^{-5}$ $2.66*10^{-5}$	$0.11*10^{-5}$ $0.10*10^{-5}$
f)	μ_{SCLC} **(cm^2/Vs)**	$0.65*10^{-5}$ $0.66*10^{-5}$	$3.06*10^{-5}$ $3.08*10^{-5}$	$0.12*10^{-5}$ $0.12*10^{-5}$

2.5. References

1   M. S. A. Abdou, X. T. Lu, Z. W. Xie, F. Orfino, M. J. Deen, and S. Holdcroft, 'Nature of Impurities in Pi-Conjugated Polymers Prepared by Ferric-Chloride and Their Effect on the Electrical-Properties of Metal-Insulator-Semiconductor Structures', *Chemistry of Materials,* 7 (1995), 631-41.

2   M. S. A. Abdou, F. P. Orfino, Y. Son, and S. Holdcroft, 'Interaction of Oxygen with Conjugated Polymers: Charge Transfer Complex Formation with Poly(3-Alkylthiophenes)', *Journal of the American Chemical Society,* 119 (1997), 4518-24.

3   M. Asada, P. Gin, M. K. Endoh, S. K. Satija, T. Taniguchi, and T. Koga, 'Directed Self-Assembly of Nanoparticles at the Polymer Surface by Highly Compressible Supercritical Carbon Dioxide', *Soft Matter,* 7 (2011), 9231-38.

4   M. Asada, N. Jiang, L. Sendogdular, J. Sokolov, M. K. Endoh, T. Koga, M. Fukuto, L. Yang, B. Akgun, M. Dimitriou, and S. K. Satija, 'Melt Crystallization/Dewetting of Ultrathin Peo Films Via Carbon Dioxide Annealing: The Effects of Polymer Adsorbed Layers', *Soft Matter* (2014).

5   P. W. M. Blom, M. J. M. deJong, and J. J. M. Vleggaar, 'Electron and Hole Transport in Poly(P-Phenylene Vinylene) Devices', *Applied Physics Letters,* 68 (1996), 3308-10.

6   C. J. Brabec, S. Gowrisanker, J. J. M. Halls, D. Laird, S. J. Jia, and S. P. Williams, 'Polymer-Fullerene Bulk-Heterojunction Solar Cells', *Advanced Materials,* 22 (2010), 3839-56.

7   C. J. Brabec, N. S. Sariciftci, and J. C. Hummelen, 'Plastic Solar Cells', *Advanced Functional Materials,* 11 (2001), 15-26.

8   J. F. Chang, J. Clark, N. Zhao, H. Sirringhaus, D. W. Breiby, J. W. Andreasen, M. M. Nielsen, M. Giles, M. Heeney, and I. McCulloch, 'Molecular-Weight Dependence of Interchain

Polaron Delocalization and Exciton Bandwidth in High-Mobility Conjugated Polymers', *Physical Review B,* 74 (2006).

9   J. F. Chang, H. Sirringhaus, M. Giles, M. Heeney, and I. McCulloch, 'Relative Importance of Polaron Activation and Disorder on Charge Transport in High-Mobility Conjugated Polymer Field-Effect Transistors', *Physical Review B,* 76 (2007).

10   A. Du Pasquier, S. Miller, and M. Chhowalla, 'On the Use of Ga-in Eutectic and Halogen Light Source for Testing P3ht-Pcbm Organic Solar Cells', *Solar Energy Materials and Solar Cells,* 90 (2006), 1828-39.

11   G. K. Fleming, and W. J. Koros, 'Dilation of Polymers by Sorption of Carbon-Dioxide at Elevated Pressures .1. Silicone-Rubber and Unconditioned Polycarbonate', *Macromolecules,* 19 (1986), 2285-91.

12   J. Frenkel, 'On Pre-Breakdown Phenomena in Insulators and Electronic Semi-Conductors', *Physical Review,* 54 (1938), 647-48.

13   P. Gin, M. Asada, M. K. Endoh, C. Gedelian, T. Lu, and T. Koga, 'Introduction of Molecular Scale Porosity into Semicrystalline Polymer Thin Films Using Supercritical Carbon Dioxide ', *Appi. Phys. Lett.,* 94 (2009), 121908.

14   S. K. Goel, and E. J. Beckman, *J. Polym. Eng. Sci.,* 34 (1994), 1148.

15   ———, 'Plasticization of Poly(Methyl Methacrylate) Networks by Supercritical Carbon Dioxide', *Polymer,* 34 (1993), 1410-17.

16   M. A. Green, K. Emery, Y. Hishikawa, W. Warta, and E. D. Dunlop, 'Solar Cell Efficiency Tables (Version 39)', *Progress in Photovoltaics,* 20 (2012), 12-20.

17   A. Guinier, 'Role of X-Ray-Diffraction in Materials Science', *Journal of the Less-Common Metals,* 28 (1972), 15-&.

18   T. Hassenkam, D. R. Greve, and T. Bjornholm, 'Direct Visualization of the Nanoscale Morphology of Conducting Polythiophene Monolayers Studied by Electrostatic Force Microscopy', *Advanced Materials,* 13 (2001), 631-34.

19   G. Horowitz, R. Hajlaoui, D. Fichou, and A. El Kassmi, 'Gate Voltage Dependent Mobility of Oligothiophene Field-Effect Transistors', *Journal of Applied Physics,* 85 (1999), 3202-06.

20   F. H. Huang, M. H. Li, L. L. Lee, K. E. Starling, and F. T. H. Chung, *J. Chem. Eng. Jpn.,* 18 (1985), 490-96.

21   R. A. J. Janssen, J. C. Hummelen, and N. S. Saricifti, 'Polymer-Fullerene Bulk Heterojunction Solar Cells', *Mrs Bulletin,* 30 (2005), 33-36.

22   K. Kanai, T. Miyazaki, H. Suzuki, M. Inaba, Y. Ouchi, and K. Seki, 'Effect of Annealing on the Electronic Structure of Poly(3-Hexylthiophene) Thin Film', *Physical Chemistry Chemical Physics,* 12 (2010), 273-82.

23   D. H. Kim, J. T. Han, Y. D. Park, Y. Jang, J. H. Cho, M. Hwang, and K. Cho, 'Single-Crystal Polythiophene Microwires Grown by Self-Assembly', *Advanced Materials,* 18 (2006), 719-+.

24   S. Kim, B. Kang, M. Lee, S. G. Lee, K. Cho, H. Yang, and Y. D. Park, 'Sequential Solvent Casting for Improving the Structural Ordering and Electrical Characteristics of Polythiophene Thin Films', *RSC Adv.,* 4 (2014), 41159.

25   ———, 'Sequential Solvent Casting for Improving the Structural Ordering and Electrical Characteristics of Polythiophene Thin Films', *Rsc Advances,* 4 (2014), 41159-63.

26   Y. Kim, S. Cook, S. M. Tuladhar, S. A. Choulis, J. Nelson, J. R. Durrant, D. D. C. Bradley, M. Giles, I. Mcculloch, C. S. Ha, and M. Ree, 'A Strong Regioregularity Effect in Self-

Organizing Conjugated Polymer Films and High-Efficiency Polythiophene: Fullerene Solar Cells', *Nature Materials,* 5 (2006), 197-203.

27   R. J. Kline, M. D. McGehee, E. N. Kadnikova, J. S. Liu, and J. M. J. Frechet, 'Controlling the Field-Effect Mobility of Regioregular Polythiophene by Changing the Molecular Weight', *Advanced Materials,* 15 (2003), 1519-+.

28   T. Koga, P. Gin, H. Yamaguchi, M. Endoh, L. Sendogdular, M. Kobayashi, A. Takahara, B. Akgun, S.K. Satija, and T. Sumi, 'Generality of Anomalous Expansion of Polymer Chains in Supercritical Fluids ', *Polymer,* 52 (2011), 4331-36.

29   T. Koga, Y. Ji, Y. S. Seo, C. Gordon, F. Qu, M. H. Rafailovich, J. C. Sokolov, and S. K. Satija, 'Neutron Reflectivity Study of Glassy Polymer Brushes in Density Fluctuating Supercrifical Carbon Dioxide', *Journal of Polymer Science Part B-Polymer Physics,* 42 (2004), 3282-89.

30   T. Koga, Y. S. Seo, X. Hu, K. Shin, Y. Zhang, M. H. Rafailovich, J. C. Sokolov, B. Chu, and S. K. Satija, 'Dynamics of Polymer Thin Films in Supercritical Carbon Dioxide', *Europhysics Letters,* 60 (2002), 559-65.

31   T. Koga, Y. S. Seo, K. Shin, Y. Zhang, M. H. Rafailovich, J. C. Sokolov, B. Chu, and S. K. Satija, 'The Role of Elasticity in the Anomalous Swelling of Polymer Thin Films in Density Fluctuating Supercritical Fluids', *Macromolecules,* 36 (2003), 5236-43.

32   T. Koga, Y. S. Seo, Y. M. Zhang, K. Shin, K. Kusano, K. Nishikawa, M. H. Rafailovich, J. C. Sokolov, B. Chu, D. Peiffer, R. Occhiogrosso, and S. K. Satija, 'Density-Fluctuation-Induced Swelling of Polymer Thin Films in Carbon Dioxide', *Physical Review Letters,* 89 (2002).

33   T. Koga, Y.S. Seo, J. Jerome, S. Ge, M.H. Rafailovich, J.C. Sokolov, B. Chu, O. H. Seeck, M. Tolan, and R. Kolb, 'Low-Density Polymer Thin Film Formation in Supercritical Carbon Dioxide', *Appl. Phys. Lett.,* 83 (2003), 4309.

34   P. Kohn, Z. Rong, K. H. Scherer, A. Sepe, M. Sommer, P. Müller-Buschbaum, R. H. Friend, U. Steiner, and S. Hüttner, 'Crystallization-Induced 10-Nm Structure Formation in P3ht/Pcbm

Blends', *Macromolecules,* 46 (2013), 4002-13.

35   P. Kohn, Z. X. Rong, K. H. Scherer, A. Sepe, M. Sommer, P. Muller-Buschbaum, R. H. Friend, U. Steiner, and S. Huttner, 'Crystallization-Induced 10-Nm Structure Formation in P3ht/Pcbm Blends', *Macromolecules,* 46 (2013), 4002-13.

36   R. Kokubu, and Y. Yang, 'Vertical Phase Separation of Conjugated Polymer and Fullerene Bulk Heterojunction Films Induced by High Pressure Carbon Dioxide Treatment at Ambient Temperature', *Phys. Chem. Chem. Phys.,* 14 (2012), 8313-18.

37   M. A. Lampert, 'Simplified Theory of Space-Charge-Limited Currents in an Insulator with Traps', *Physical Review,* 103 (1956), 1648-56.

38   Murray A. Lampert, and Peter Mark, *Current Injection in Solids*, *Electrical Science* (New York,: Academic Press, 1970), pp. xii, 351 p.

39   G. Li, V. Shrotriya, J. S. Huang, Y. Yao, T. Moriarty, K. Emery, and Y. Yang, 'High-Efficiency Solution Processable Polymer Photovoltaic Cells by Self-Organization of Polymer Blends', *Nature Materials,* 4 (2005), 864-68.

40   G. Li, R. Zhu, and Y. Yang, 'Polymer Solar Cells', *Nature Photonics,* 6 (2012), 153-61.

41   X. X. Li, and B. D. Vogt, 'Impact of Thickness on Co2 Concentration Profiles within Polymer Films Swollen near the Critical Pressure', *Polymer,* 50 (2009), 4182-88.

42   Y. Li, E. park, K. Lim, K. P. Johnston, and P. F. Green, 'Role of Interfacial Interactions on the Anomalous Swelling of Polymer Thin Films in Supercritical Carbon Dioxide', *J. Polym. Sci., Part B:Polym. Phys.,* 45 (2007), 1313-24.

43   H. H. Liao, C. M. Yang, C. C. Liu, S. F. Horng, H. F. Meng, and J. T. Shy, 'Dynamics and Reversibility of Oxygen Doping and De-Doping for Conjugated Polymer', *Journal of Applied Physics,* 103 (2008).

44   R. D. McCullough, 'The Chemistry of Conducting Polythiophenes', *Advanced Materials,* 10 (1998), 93-+.

45   R. D. Mccullough, R. D. Lowe, M. Jayaraman, and D. L. Anderson, 'Design, Synthesis, and Control of Conducting Polymer Architectures - Structurally Homogeneous Poly(3-Alkylthiophenes)', *Journal of Organic Chemistry,* 58 (1993), 904-12.

46   E. J. Meijer, C. Detcheverry, P. J. Baesjou, E. van Veenendaal, D. M. de Leeuw, and T. M. Klapwijk, 'Dopant Density Determination in Disordered Organic Field-Effect Transistors', *Journal of Applied Physics,* 93 (2003), 4831-35.

47   E. J. Meijer, A. V. G. Mangnus, B. H. Huisman, G. W. 't Hooft, D. M. de Leeuw, and T. M. Klapwijk, 'Photoimpedance Spectroscopy of Poly(3-Hexyl Thiophene) Metal-Insulator-Semiconductor Diodes', *Synthetic Metals,* 142 (2004), 53-56.

48   A. Mendoza-Galvan, C. Trejo-Cruz, O. Solis-Canto, and G. Luna-Barcenas, 'Effect of a Temperature Gradient on Ellipsometry Measurements in Supercritical Co2', *Journal of Supercritical Fluids,* 64 (2012), 25-31.

49   C. Y. Nam, 'Facile Determination of Bulk Charge Carrier Concentration in Organic Semiconductors: Out-of-Plane Orientation Hopping Conduction Characteristics in Semicrystalline Polythiophene', *Journal of Physical Chemistry C,* 116 (2012), 23951-56.

50   C. Y. Nam, D. Su, and C. T. Black, 'High-Performance Air-Processed Polymer-Fullerene Bulk Heterojunction Solar Cells', *Advanced Functional Materials,* 19 (2009), 3552-59.

51   K. Nishikawa, I. Tanaka, and Y. Amemiya, 'Small-Angle X-Ray Scattering Study of Supercritical Carbon Dioxide', *J. Phys. Chem.,* 100 (1996), 418-21.

52   N. Reitzel, D. R. Greve, K. Kjaer, P. B. Hows, M. Jayaraman, S. Savoy, R. D. McCullough, J. T. McDevitt, and T. Bjornholm, 'Self-Assembly of Conjugated Polymers at the Air/Water Interface. Structure and Properties of Langmuir and Langmuir-Blodgett Films of Amphiphilic Regioregular Polythiophenes', *Journal of the American Chemical Society,* 122 (2000), 5788-800.

53   H. W. Ro, B. Akgun, B. T. O'Connor, M. Hammond, R. J. Kline, C. R. Snyder, S. K. Satija, A. L. Ayzner, M. F. Toney, C. L. Soles, and D. M. DeLongchamp, 'Poly(3-Hexylthiophene) and [6,6]-Phenyl-C-61-Butyric Acid Methyl Ester Mixing in Organic Solar Cells', *Macromolecules,* 45 (2012), 6587-99.

54   J. R. Royer, J. M. DeSimone, and S. A. Khan, 'Carbon Dioxide-Induced Swelling of Poly(Dimethylsiloxane)', *Macromolecules,* 32 (1999), 8965-73.

55   T. P. Russell, 'X-Ray and Neutron Reflectivity for the Investigation of Polymers', *Mater. Sci. Rep.,* 5 (1990), 171-271.

56   P. Scherrer, 'Bestimmung Der Grösse Und Der Inneren Struktur Von Kolloidteilchen Mittels Röntgenstrahlen', *Nachr. Ges. Wiss. Göttingen,* 26 (1918), 98-100.

57   K. Shin, X. Hu, X. Zheng, M.H. Rafailovich, J.C. Sokolov, V. Zaitsev, and S. A. Schwarz, 'Silicon Oxide Surface as a Substrate of Polymer Thin Films', *Macromolecules,* 34 (2001), 4993.

58 S. M. Sirard, P. R. Gupta, T. P. Russell, J. J. Watkins, P. F. Green, and K.P. Johnson, *Macromolecules,* 36 (2003), 3365-73.

59 S. M. Sirard, Z. K. J., L. C. Sanchez, P. F. Green, and K. P. Johnston, *Macromolecules,* 35 (2002), 1928.

60 H. Sirringhaus, P. J. Brown, R. H. Friend, M. M. Nielsen, K. Bechgaard, B. M. W. Langeveld-Voss, A. J. H. Spiering, R. A. J. Janssen, E. W. Meijer, P. Herwig, and D. M. de Leeuw, 'Two-Dimensional Charge Transport in Self-Organized, High-Mobility Conjugated Polymers', *Nature,* 401 (1999), 685-88.

61 C. W. Tang, '2-Layer Organic Photovoltaic Cell', *Applied Physics Letters,* 48 (1986), 183-85.

62 K. Tremel, and S. Ludwigs, 'Morphology of P3ht in Thin Films in Relation to Optical and Electrical Properties', *P3ht Revisited: From Molecular Scale to Solar Cell Devices,* 265 (2014), 39-82.

63 P. Vanlaeke, A. Swinnen, I. Haeldermans, G. Vanhoyland, T. Aernouts, D. Cheyns, C. Deibel, J. D'Haen, P. Heremans, J. Poortmans, and J. V. Manca, 'P3ht/Pcbm Bulk Heterojunction Solar Cells: Relation between Morphology and Electro-Optical Characteristics', *Solar Energy Materials and Solar Cells,* 90 (2006), 2150-58.

64 E. Verploegen, C. E. Miller, K. Schmidt, Z. N. Bao, and M. F. Toney, 'Manipulating the Morphology of P3ht-Pcbm Bulk Heterojunction Blends with Solvent Vapor Annealing', *Chemistry of Materials,* 24 (2012), 3923-31.

65 H. Xie, H. Alves, and A. F. Morpurgo, 'Quantitative Analysis of Density-Dependent Transport in Tetramethyltetraselenafulvalene Single-Crystal Transistors: Intrinsic Properties and Trapping', *Physical Review B,* 80 (2009).

66   H. Yamaguchi, P. Gin, H. Arita, M. Kobayashi, S. Bennett, S. K. Satija, M. Asada, T. Koga, and A. Takahara, 'Effect of Supercritical Carbon Dioxide on Molecular Aggregation States of Side Chains of Semicrystalline Poly{2-(Perfluorooctyl)Ethyl Acrylate} Brush Thin Films', *RSC Advances,* 3 (2013), 4778-85.

67   G. T. Yue, J. H. Wu, Y. M. Xiao, H. F. Ye, J. M. Lin, and M. L. Huang, 'Flexible Dye-Sensitized Solar Cell Based on Pcbm/P3ht Heterojunction', *Chinese Science Bulletin,* 56 (2011), 325-30.

68   A. Zen, J. Pflaum, S. Hirschmann, W. Zhuang, F. Jaiser, U. Asawapirom, J. P. Rabe, U. Scherf, and D. Neher, 'Effect of Molecular Weight and Annealing of Poly (3-Hexylthiophene)S on the Performance of Organic Field-Effect Transistors', *Advanced Functional Materials,* 14 (2004), 757-64.

69   K. Zhao, L. J. Xue, J. G. Liu, X. Gao, S. P. Wu, Y. C. Han, and Y. H. Geng, 'A New Method to Improve Poly(3-Hexyl Thiophene) (P3ht) Crystalline Behavior: Decreasing Chains Entanglement to Promote Order-Disorder Transformation in Solution', *Langmuir,* 26 (2010), 471-77.

70   Y. Zhao, Z. Y. Xie, Y. Qu, Y. H. Geng, and L. X. Wang, 'Solvent-Vapor Treatment Induced Performance Enhancement of Poly(3-Hexylthiophene): Methanofullerene Bulk-Heterojunction Photovoltaic Cells', *Applied Physics Letters,* 90 (2007).

3. Chapter 3: Low-temperature CO_2 annealing for manipulating P3HT/PCBM blend morphologies

3.1. Abstract

The morphology of the photoactive layer in organic bulk heterojunction solar cells is a key performance defining parameter. In this study, pressure controlled CO_2 treatment at just above room temperature was applied to control morphologies of poly(3-hexylthiophene) (P3HT) and phenyl-C_{61}-butyric acid methyl ester (PCBM) blend thin films. Combined surface sensitive techniques including scanning electron microscopy (SEM), grazing incidence X-ray diffraction (GID), UV-vis spectroscopy, and optical microscopy, we found that the CO_2 treatments induce PCBM concentration gradient along the direction normal to the film surface by the excess CO_2 adsorption into the polymer matrix. The morphological changes after the CO_2 treatment were attributed to increased chain mobility, resulting in higher crystalline order of P3HT as discussed in chapter 2. In addition, we found that this polymer plasticization accelerates the crystallinity of the P3HT chains. As a result, the PCBM nanoparticles are pushed out from the inner chain conformations and are prone to migrate to the polymer-CO_2 interface where the excess amount of CO_2 molecules exists. The driving force for the surface migration is excess adsorption of CO_2 molecules on the nanoparticle surfaces, as discussed in Chapter 1: the CO_2-wetted nanoparticles preferentially migrate to the topmost CO_2-rich region through the concentration gradient. We also discuss that this scCO_2 controlled phase segregation introduces better electrical response as deduced from device I-V performance.

3.2. Introduction

One of the earliest organic bilayer OPVs with two small conjugated molecules introduced by Tang achieved device efficiency of 1%.[3] Limitation on this earlier concept was the minimum required film thickness for the full incident light adsorption (~ 100 nm) which is much larger than exciton diffusion length (~ 10 nm)[4]; therefore, as it can be seen from this example, only 10% of the generated excitons have a possible chance of being transferred (Fig. 1(a)). Later, an alternative concept, bulk heterojunction (BHJ) solar cells for organic semiconductors was introduced in 1990s, considering both optimum layer thickness for sufficient light adsorption and low exciton diffusion lengths.[5] In BHJ, solar cells donor and acceptor components are intermixed with distributed junctions those are not planar like bilayer solar cells (Fig. 1(b)).
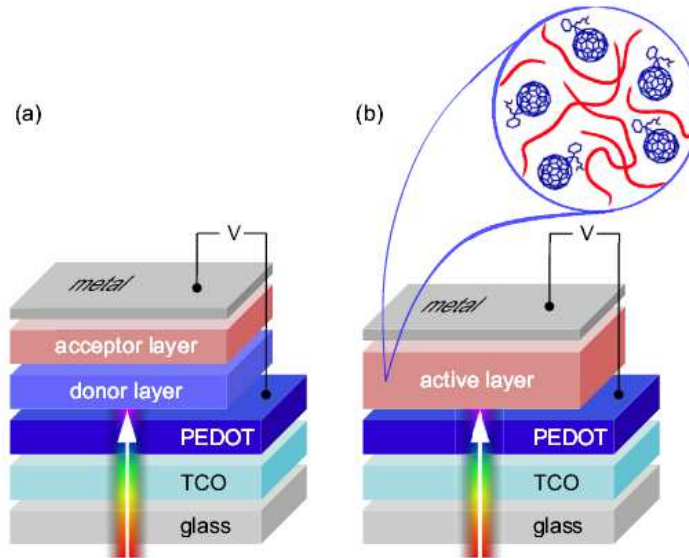
Figure 3- 1 Examples of device configurations a) bilayer device with planar heterojunction b) bulk heterojunction device composed of conjugated polymer and fullerene derivative. Data from Deibel et. al.[2]

One of the most common fabrication methods for BHJ solar cells is a spin coating method[6-8]; however, disordered structures after spin coating are still a bottleneck: strong

Coulomb interactions between electron-hole charge pairs make it difficult to dissociate these charge couples, and, due to disordered structure and pathway deficiencies, trapped charges are most likely to recombine with the free charges.

To fabricate an efficient organic solar cell, morphology of bulk heterojunctions (BHJ) is of critically importance: bicontinuous blend structures of hole and electron transferring components should be built in a way to adsorb as much light as possible for efficient exciton dissociation, charge transportation and charge collection. In addition, all these figures are drastically influenced by the volume morphology of the photoactive layer.[9, 10] Following studies on BHJ photovoltaic cells (OPVs) have focused on polymer/fullerene blend films with thicknesses between 40-200nm[11-14]. It was indicated that regardless of film thickness donor and acceptor phases with smaller domain sizes than exciton diffusion length should be well interpenetrating to form nanoscale interfaces distributed throughout the whole photoactive layer for high efficiency BHJ solar cells.

Upon disassociation of excitons by adsorbed light energy in the interfacial region, created free electrons and holes should be transferred through acceptor and donor components to the negative (metal) electrode and positive electrode, respectively.[10, 15] As explained in Chapter 2, many studies have been focused on morphological structures of both acceptor and donor materials to characterize the effects of crystalline order, dimensions, and orientations on the charge transfer process. In addition, the nanoscale intermixing structure is also critical at larger interfacial areas between components enhances photo-carrier generation and also short circuit current (J_{SC}) hindering charge recombination; therefore, bicontinuity of each phase is necessary to shorten these permeating pathways. Hence, as reported by van Bavel et. al.[16] and Kumar et. al.[17], it is an ideal condition for charge collection to have acceptor material enrichments close to

the metal electrode and donor material enrichment close to the positive electrode, which will shorten charge transfer pathways. On the other hand, it should be emphasized that the enrichment of one component near the positive electrode would introduce smaller interfacial areas on that region which is not beneficial in terms of charge carrier generation. That is why bulk morphology is desired to reflect smaller domain sizes, while larger domain sizes close to the corresponding electrodes would introduce the optimization of device structure.[18, 19]
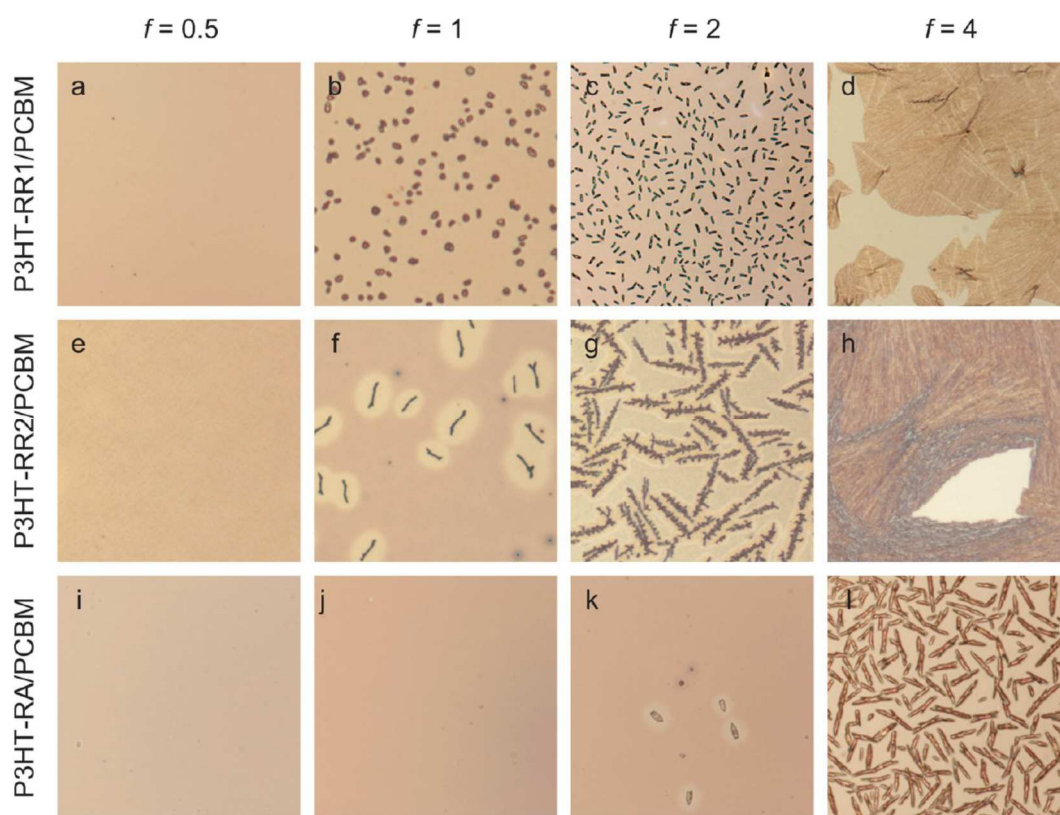
Figure 3- 2 Optical microscopy images of (a−d) P3HT-RR1/PCBM, (e−h) P3HT-RR2/PCBM, and (i−l) P3HT-RA/PCBM films. The PCBM to polymer weight fraction was varied from f = 0.5 to f = 4. Data from Kohn et. al.[1]

As shown in Fig. 3-2, PCBM concentration dependence and P3HT regioregularity dependence after thermal annealing were studied earlier. The results suggested that the phase

segregation of PCBM is directly proportional to polymer crystallinity and PCBM concentrations which can be also seen on fig. 3-2(i-k): regiorandom polymer has higher PCBM miscibility and therefore phase segregation is retarded on the active layer surface.[1] Therefore, similar post-processing based treatments have been implemented in different ways which lead to structure-based device performance enhancements in the last 20 years. These methods include conventional thermal annealing[8, 20-23], solvent annealing[8, 20, 24, 25], and the use of additives[26, 27], all of which mainly focused on controlling lateral morphology, whereas only a few assisted to optimize P3HT and PCBM vertical concentration gradients. The vertical composition of the photoactive layer is critically important because charges are transferred to their corresponding electrodes right after they are dissociated at the interfacial region along this direction. Hence, as also explained above, electron-acceptor materials, electron conductor, and enrichment towards the cathode create higher charge collection efficiency. However, it has been reported that as a result of surface energy differences where polymer surface energy is lower than PCBM (γ_{P3HT}=27mN m^{-2} and γ_{PCBM}=38mN m^{-2}), conventional thermal annealing promotes polymer accumulation at the top layer and PCBM dispersion within the blend film[28] which is conceptually undesired because this causes PCBM depleted area close to the cathode contact surface. And as also reported by Wang et. al.[29], flipping the blend film upside down also does not change device electrical properties because PCBM component is isolated by P3HT within blend structure; therefore, PCBM depleted area is also seen on anode contact surface.

The necessity of a method to fabricate photoactive layers with PCBM surface segregated structures is crucial. To achieve the goal, various studies have already conducted: such as the use of blend solvents or additives to manage surface directed assembly of PCBM components by making use of solubility and volatility differences,[27] or PCBM aggregates forming onto primarily

crystallized P3HT chains on a substrate.[20] On the other hand, those methods are mostly disadvantageous since the use of additives or artificially created layer structures introduces band gaps and the resultant charge traps reduce device performance.

An alternative use of CO_2 as an effective plasticization agent for conjugated polymer-fullerene systems is proposed and we aimed to control spatial distributions of PCBM particles embedded in a P3HT polymer matrix. As explained in Chapters 1 & 2, compressed CO_2 is known to absorb in organic materials like polymers, decreasing glass transition temperature (T_g) and accelerate the chain mobility[30], and blend film morphologies are expected to be controlled by this plasticization agent as function of pressure, temperature and exposure time. In addition, added PCBM particles are also covered with a wetting layer of CO_2 near critical point which acts as a "surfactant".[31, 32] On the contrary, it was reported that when constraints on polymer chains introduced by the addition of nanoparticles reaches to a critical threshold level, nanoparticles are directed to the polymer/air interface regardless of compatibility, called "entropy-driven segregation".[33-35] This can be observed in Fig. 3-2 where as the nanoparticle concentration is increased, PCBM starts to migrate to the polymer/air interface. In that case, the magnitude of aggregation is also dependent upon polymer crystallinity. As discussed in Chapter 1, similar segregation of nanoparticles embedded in polymer thin films under $scCO_2$ takes place at around the ridge condition where excess CO_2 adsorption occurs due to the anomalous swelling of ultrathin polymer films. Furthermore, anomalous swelling is an interfacial effect which takes place at the polymer-CO_2 interface[36] as well as the polymer-substrate interface reported by Li and Vogt[37, 38]. However, the detailed descriptions of the phenomenon still remain unclear.

In this chapter, the film structures of regioregular-P3HT/PCBM blend films with the CO2 annealing at the ridge and off-ridge conditions are discussed. In addition, the effect of the resultant structures induced by the CO2 process on the conductivity performance is also presented.

3.3. Experimental Section

3.3.1. Thin Film Preparation

The same regioregular P3HT (purchased from American Dye Source Inc. with a number-average molecular mass M_n=69kDa and the approximate regioregularity of 96%) used in Chapter 2 was chosen. The polymer was dissolved in a good solvent (chlorobenzene). In order to study the effect of the blend film thickness, the polymer concentration in chlorobenzene was fixed at three different weight ratios: 0.5%, 1% and 2%. PCBM was then added to the polymer solutions to have the exact P3HT/PCBM blend ratios of (4:1), (2:1), and (1:1). It should be noted that as it can be seen from this recipe, we tried not to exceed the PCBM content over the P3HT content, because phase segregation introduced by concentration based constraints is already known. Instead, in this study, CO_2 was used to induce surface PCBM migration with much less PCBM concentrations. The polymer solutions were heated at 60°C for at least 3h before filtering the solution using a PTFE syringe filter (a 0.45μm pore-size). Silicon wafers (1×1 cm^2 and 0.5-mm thickness) were placed in piranha solutions (i.e., a mixture of H_2SO_4 and H_2O_2) at T=373 K for 30 min. The wafers were rinsed with deionized water and subsequently submersed in an aqueous solution of hydrogen peroxide (HF) for 1 min to remove a native oxide layer (SiOx) on Si substrates. However, it should be noted that we confirmed that a SiO_2 layer of about 1.3 nm in thickness was reproduced even just after hydrofluoric acid etching due to atmospheric oxygen

and moisture, as reported previously[39]. The filtered P3HT/PCBM solutions were then spun cast onto the HF-etched Si wafers at room temperature with a rotation speed of 1500 rpm, giving the thicknesses of about 25 nm, 50 nm and 100 nm for the P3HT/PCBM blend films with the blend ratios of (4:1), (2:1) and (1:1) for each film thicknesses. Finally, the spin-coated P3HT/PCBM blend films were kept under vacuum at room temperature (25°C) for 24 h to remove residual solvent molecules.

CO$_2$ exposure time dependence ranging from 2h to 24h at the two different pressures (8MPa, 14MPa) under the isothermal condition of 36°C) were found from Chapter 2 to achieve comparative results with pristine P3HT and P3HT/PCBM films. After the CO$_2$ exposure, the chamber was rapidly quenched to atmospheric pressure within 10 s. At the same time, as controls, we treated the P3HT/PCBM thin films via conventional high temperature annealing at 170 °C for 2h, followed by rapid quench to room temperature.

3.4.   Results and Discussion

3.4.1. Polarized Optical Microscopy Results

The thin P3HT/PCBM blend films were studied after either CO$_2$ exposure or thermal annealing. As shown in Fig. 3-3, the P3HT/PCBM blend films with the (1:1) mixing ratio were treated under the three different post-annealing conditions. From this figure we can see that microclusters of the PCBM nanoparticles form in the respective regioregular P3HT/PCBM blend films regardless of post-deposition treatments and film thicknesses. This is due to the higher order structure of regioregular P3HT[1]. In contrast, regioregular P3HT has the smaller lattice spacings and smaller amorphous faction than

those of the regiorandom P3HT/PCBM blend films (Fig. 3-6) where the placement of the PCBM particles within the matrix forms much larger constraints pushing the PCBM particles to the polymer/CO_2 or polymer/air interfaces to reduce its entropic energy.[40]

Figure 3- 3 Optical images of 24h-scCO$_2$ treated (at 36°C) and 24h-thermal annealed samples (at 170°C) (a-c) 25nm P3HT/PCBM thin films with (1:1) blend ratio, (d-f) 50nm P3HT/PCBM thin films with (1:1) blend ratio, (g-i) 100nm P3HT/PCBM thin films with (1:1) blend ratio. Image widths: 70x70μm^2.

However, the surface coverage and microcluster sizes in the CO_2 treated blend films differ from those of the thermal annealing, possibility due to the polymer mobility

that defines the magnitude of particle migration to the air interface. As it can be seen from Fig. 3-3(b-e-h) and (c-f-i), the microclusters are more dispersive and homogeneous with the CO_2 treated blend films at the ridge condition where the CO_2 plasticizes the polymer chains in the most effectively manner [37, 38]. In addition, it is clear that the ridge condition, the surface migration is enhanced compared to that at the off-ridge condition (Fig. 3-4). Furthermore we can see that the thicker films are prone to form much larger and wider microclusters even with the same blend ratios. This is due to the higher amounts of PCBM originally embedded in the thicker films, facilitating the surface migration of the nanoparticles to the polymer/CO_2 or polymer/air surfaces.
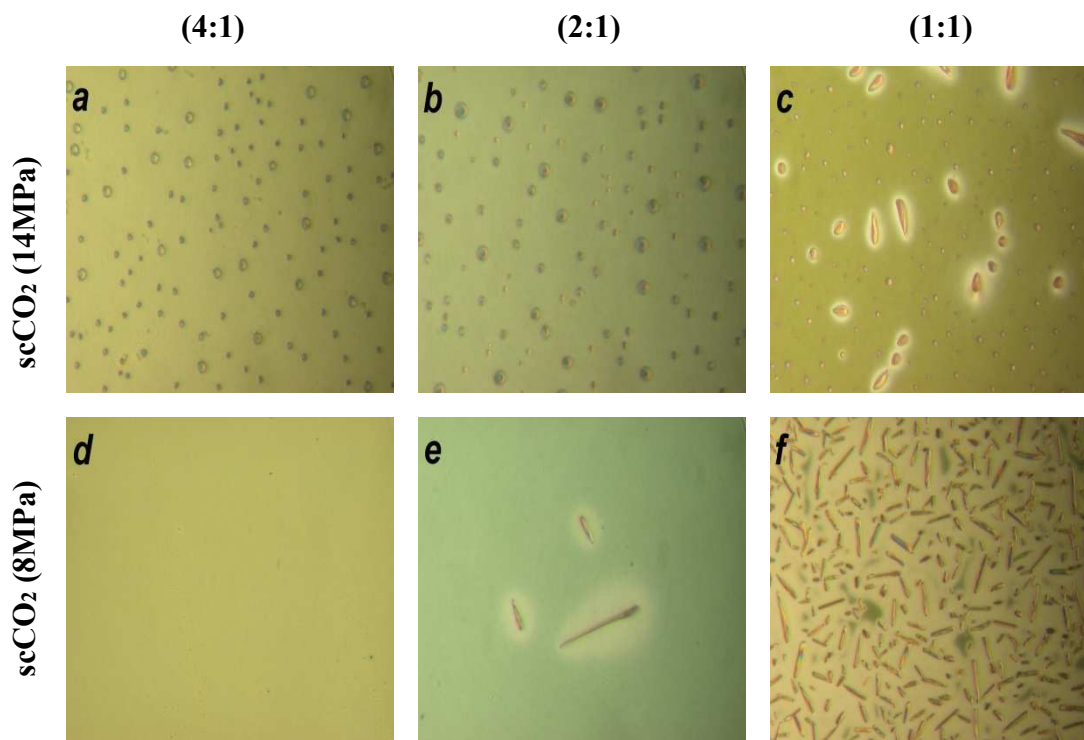
Figure 3- 4 Optical images of 24h-CO_2 treated 50nm P3HT/PCBM thin films at 36°C (a-c) CO_2 pressure at 14MPa with increasing PCBM concentration from a to c: (4:1), (2:1) and (1:1), (d-f) CO_2 pressure at 8MPa with increasing PCBM concentration from d to f: (4:1), (2:1) and (1:1). Image widths: $70 \times 70 \mu m^2$.

We also confirmed that even after 24h CO_2 exposure at the ridge condition, the polymer structure remained unchanged compare to Fig. 3-5(c), indicating that the surface migration structures is a metastable structure. Therefore, the PCBM microcluster sizes and surface coverage of the CO_2 (14MPa) treated blend films shown in Fig. 3-4 is in non-equilibrium. It is also interesting to note that when the PCBM concentration is higher (fig. 3-4(c)), the cluster sizes become larger, this might be due to the more PCBM particles diffuse to the former PCBM crystals which causes PCBM depleted areas on one side and larger crystals on the other.[18]
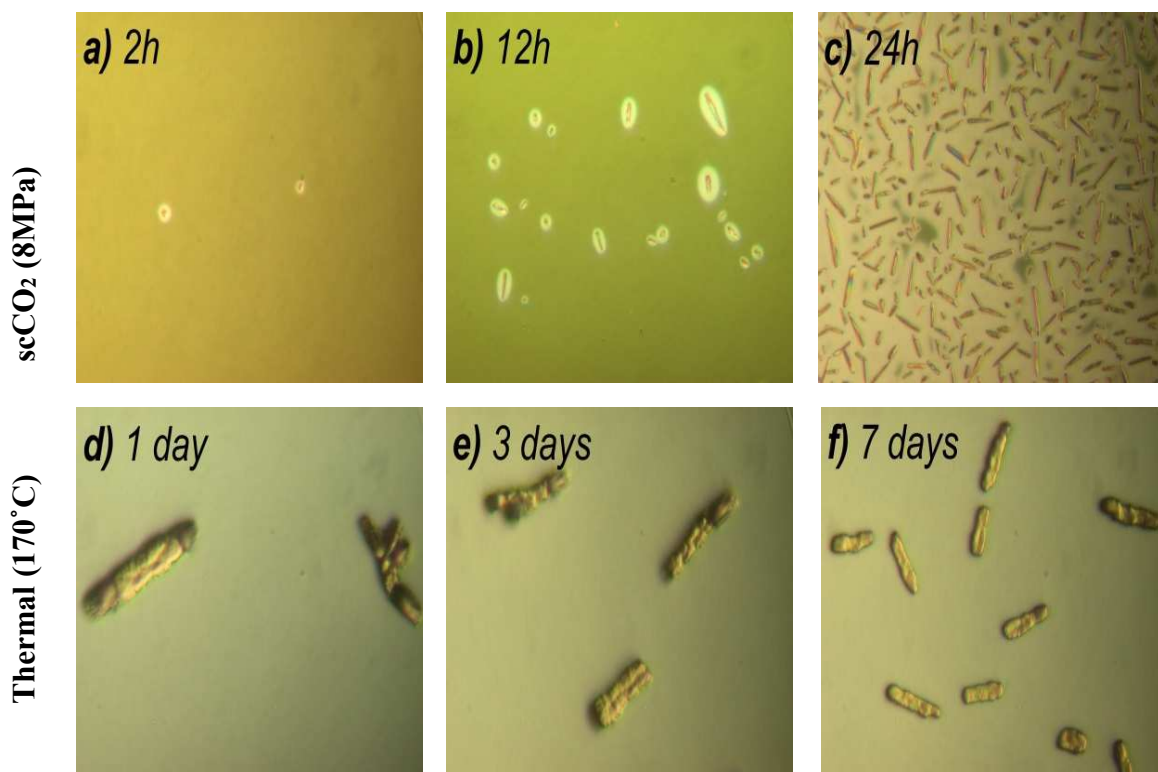
Figure 3- 5 Optical images of scCO$_2$ and conventional thermal annealing treated 50nm P3HT/PCBM thin films with (1:1) blend ratio (a-c) scCO$_2$ samples at 8MPa and 36°C with exposure times from 2h to 24h, (d-f) thermally annealed samples at 170°C with annealing times from 1 day to 7days. Image widths: 70x70μm^2.

In Fig. 3-5, the time evolution of CO_2 annealed and thermal annealed films are summarized. We can see that CO_2 is advantageous for the surface migration phenomenon due to the higher polymer mobility induced by the large amount of CO_2 molecules absorbed in the matrix. While 24h CO_2 exposure is enough to reach the metastable structures, thermal annealing at 170°C for 7 days is not sufficient enough to induce such a large magnitude of surface migration.

| | Thermal (170˚C) | scCO₂ (8MPa) | scCO₂ (14MPa) |
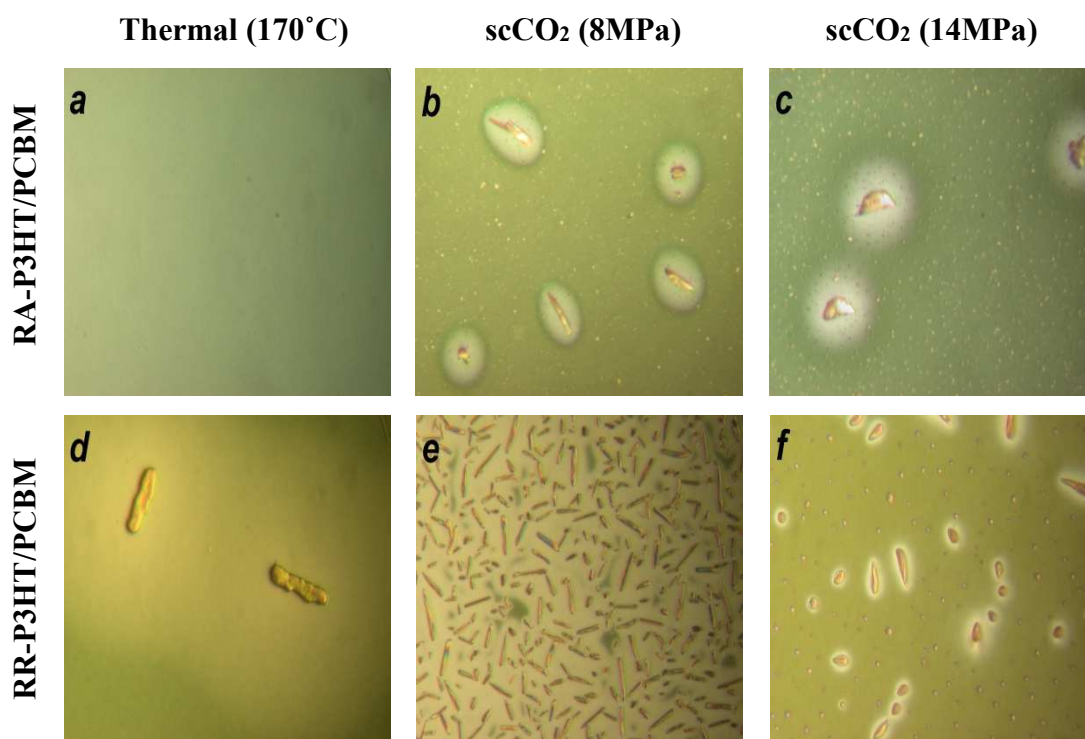
Figure 3- 6 Optical images of 24h-scCO₂ treated (at 36˚C) and 24h-thermal annealed (at 170˚C) 50nm P3HT/PCBM thin films with (1:1) blend ratio (a-c) Regiorandom P3HT/PCBM, (d-f) Regioregular P3HT/PCBM. Image widths: 70x70μm^2.

As reported by Kohn et. al.[1] (Fig. 3-2), regiorandom P3HT has higher miscibility with PCBM because of the larger amorphous component so that the surface migration of PCBM in the regiorandom P3HT/PCBM with the (1:1) ratio does not occur (Fig. 3-6a). However, as shown in

Fig. 3-6, the CO_2 process even with the off-ridge condition allowed us to induce the surface migration of the PCBM particles at the (1:1) blend ratio (Fig. 3-6 b&c). This finding is encouraging that regiorandom P3HT could be also utilized for energy production in BHJ solar cells in conjunction with our novel CO_2 annealing process.
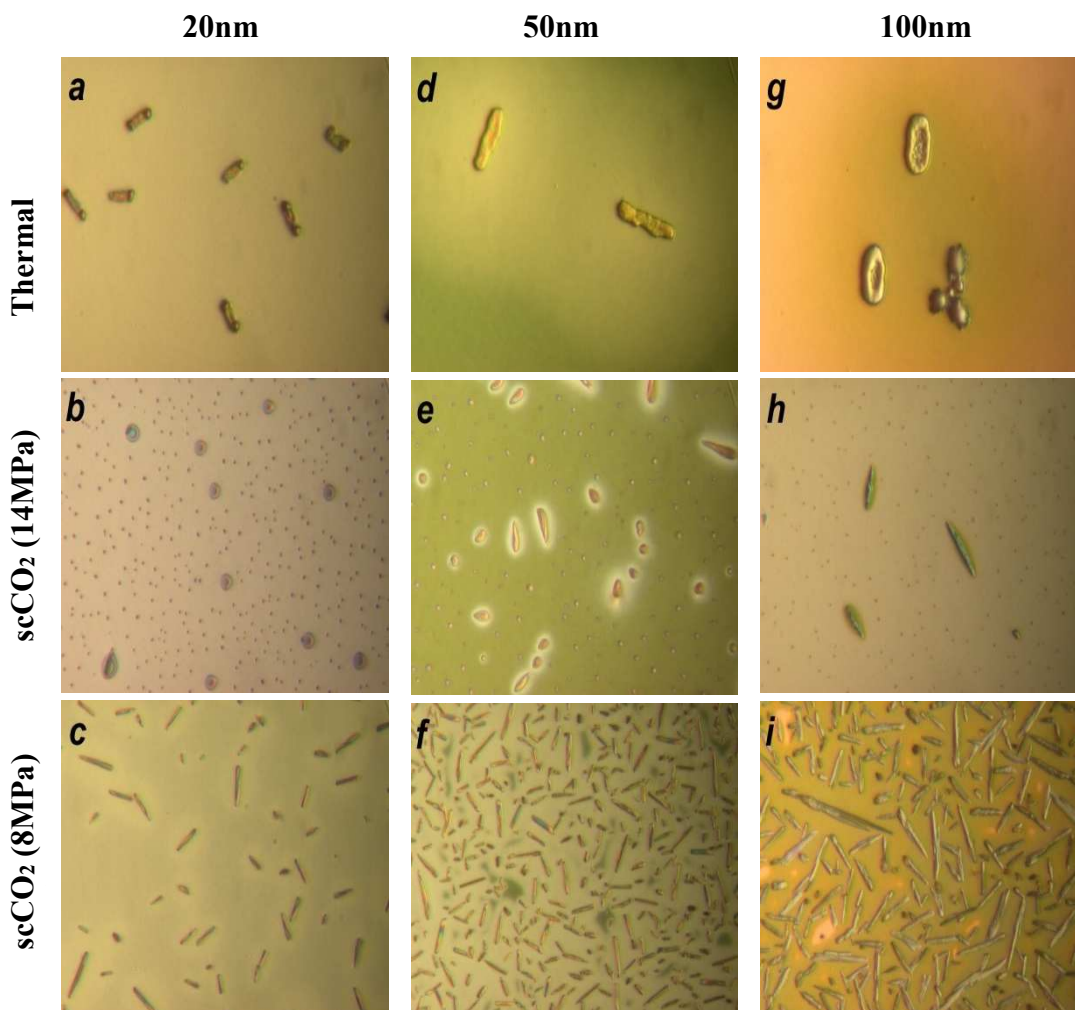
3.4.2. SEM and AFM results
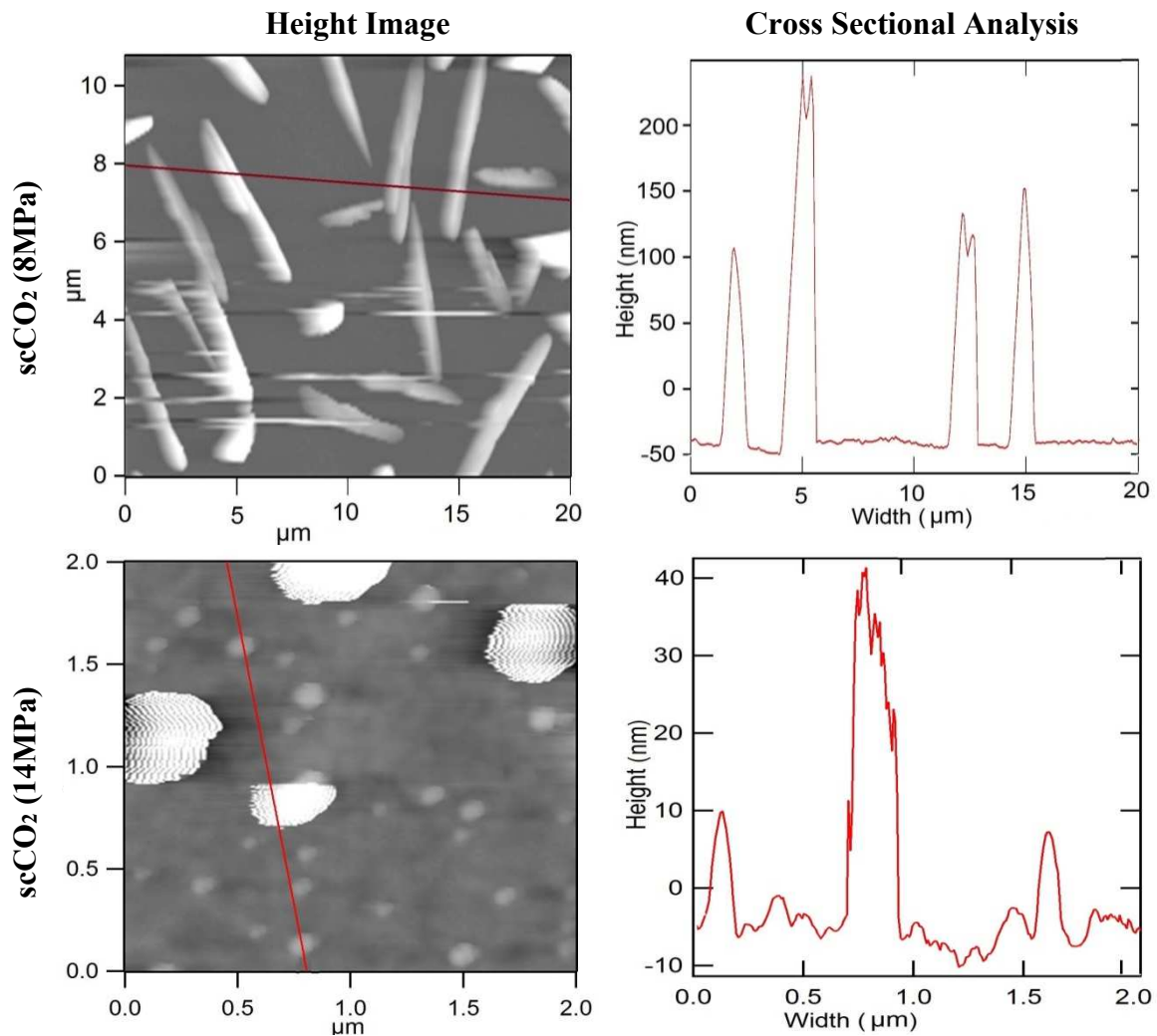
Figure 3- 7 Optical images of 24h-scCO$_2$ treated (at 36˚C) and 24h-thermal annealed (at 170˚C) 50nm P3HT/PCBM thin films with (1:1) blend ratio (a-c) Regiorandom P3HT/PCBM, (d-f) Regioregular P3HT/PCBM. Image widths: 70x70μm^2.

The CO_2 annealed and thermally annealed P3HT/PCBM blend films were also examined by atomic force microscopy (AFM) (Fig. 3-7) and cross sectional scanning electron microscopy (SEM) (Fig. 3-8). Preferential P3HT surface accumulation[28] after spin-casting was mentioned above which forms flat plateau like smooth surface of PCBM deficient region; on contrary, it was found that this smooth surface transformed into the rough morphology (fig 3-7) after the CO_2 treatment which indicates the PCBM enrichment on the film surface (Fig. 3-7 and 3-8(right)). The solubility of CO_2 with P3HT might be insufficient to melt the polymer (Fig. 2-9), but the PCBM component clearly migrates and forms large microclusters through the CO_2 exposure. Moreover, the SEM images allow us to conclude that the PCBM microclusters after the CO_2 process show much larger sizes compared to the thermally annealed film.
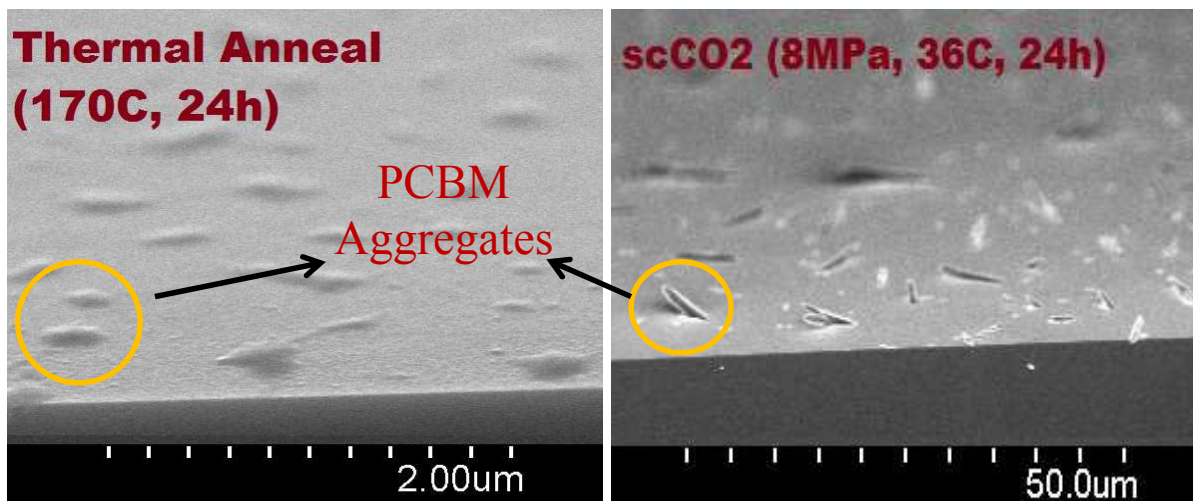
Figure 3- 8 SEM Images of 50nm P3HT/PCBM thermal annealed thin films with 2μm scale bar (left) and scCO2 annealed (8Mpa) thin films (right).

3.4.3. Uv-vis spectroscopy results

In this section, the effect of packing order of the donor materials on optical solar cell performance of the P3HT/PCBM blend films were demonstrated by means of UV-vis spectroscopy. In order to remove artificial noise and background for ultrathin films, reflecting mode was used to capture the data (see fig. 3-9(f) and fig. 3-10). Reflective mode gave productive and comparative results as a function of the blend film surface structure shown in Fig. 3-9. The PCBM contribution can be attributed to the UV-region at the lower wavelength of 350-400 nm) and P3HT contribution is seen at the visible light region (at the higher wavelength of 550-700 nm). As discussed in Chapter 1, the region of the anomalous adsorption of CO_2 molecules is determined by the correlation length of the density fluctuations of CO_2 near the critical point and thereby only occurs within the first few ten nanometers depth from the polymer/scCO2 interface[41]. Therefore, as in the 25nm P3HT/PCBM films, density fluctuating CO_2 molecules penetrate all the way down to the substrate surface so that the vertical film morphology is expected to be relatively homogeneous.[42] This can be further confirmed with UV-vis spectroscopy results where all data points for the 25 nm blend films (Fig. 3-7(a-c)) cross at around 500 nm wavelength, indicating that the signals emitting from P3HT and PCBM are volumetrically well proportioned and gives an "Isobectic" point.[43]
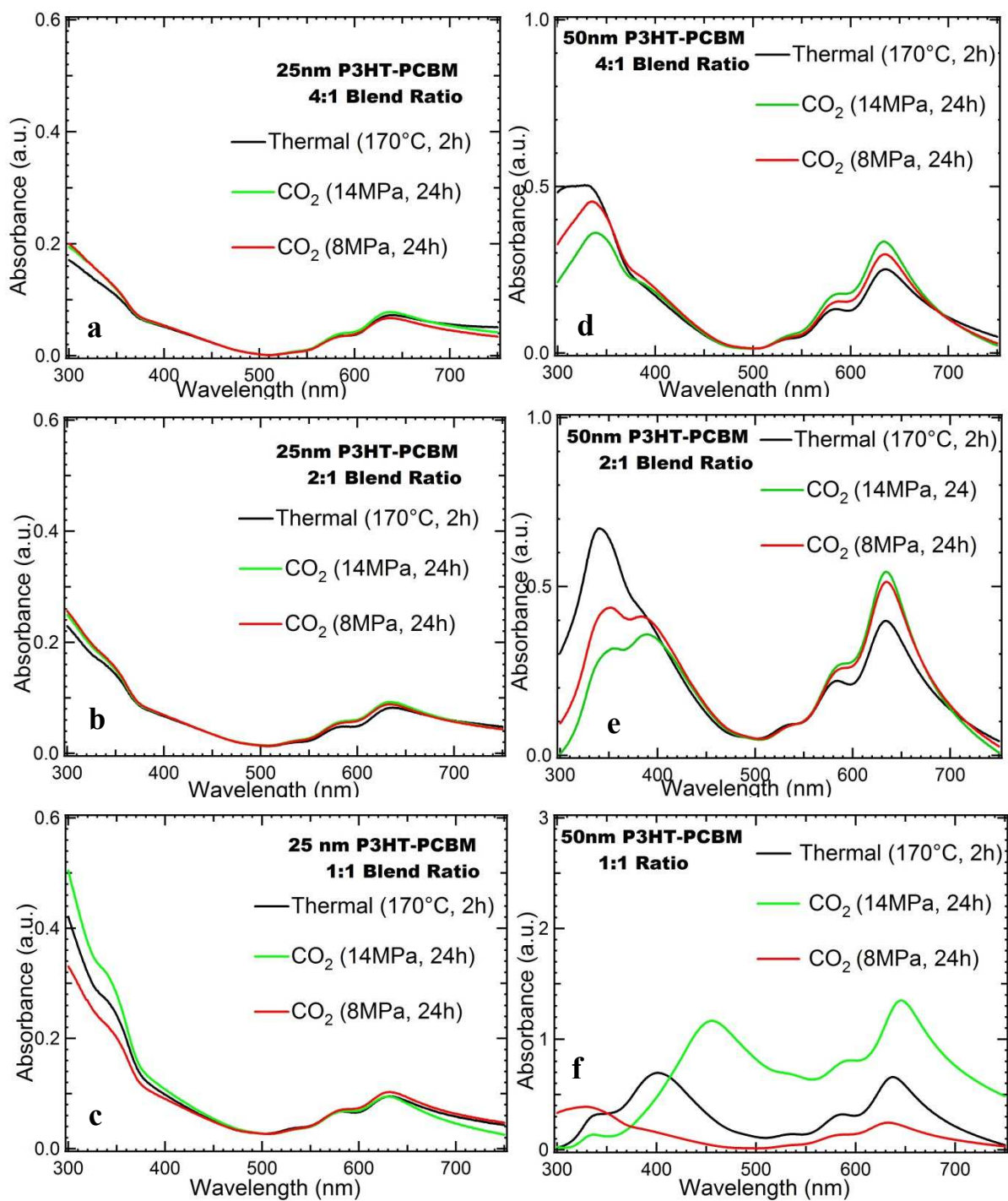
Figure 3- 9 Optical absorption of P3HT/PCBM films after isothermal scCO$_2$ (36˚C), and thermal annealing (a-c) 25nm P3HT/PCBM films with blend ratios of (4:1), (2:1) and (1:1) (d-f) 50nm P3HT/PCBM films with blend ratios of (4:1), (2:1) and (1:1).

The existence of the Isobectic point is an indication for coexisting crystalline P3HT and amorphous P3HT, and in Isobectic systems crystalline and amorphous P3HT are in a balance that upon PCBM concentration change there would not be acute changes. On the other hand, this balance seems to be slightly shifting for the 25 nm P3HT/PCBM films with the (2:1) blend ratio (Fig. 3-7(b)) which means that for this composition PCBM component leads to considerable changes in blend morphology under CO_2. Previous reports also suggested that 40 to 60% PCBM concentrations showed the strongest response for thermal annealing films in terms of device performance[44].

When the 25nm and 50nm P3HT/PCBM films are compared, we can see that CO_2 penetration depth is probably larger than 25nm, but smaller than 50 nm since the CO_2 effect becomes clearer with stronger peaks on the visible light region attributed to higher order interplane interactions[45]. The stronger peak intensities are related to the segregation of ordered P3HT domains with enhanced intraplain and interplain packing orders in the out of plane blend structures (fig. 3-9(d-f)). Especially, enhancements in visible light region compared to the control sample shown in Fig. 3-9(d and e) is associated with self-organization of P3HT in scCO$_2$ and more precisely, this phenomenon is stronger at the (2:1) blend ratio, which is in agreement with the 25 nm films.[46] Moreover, 50nm P3HT/PCBM thin films' light absorption capacity is more enhanced in the visible region by high pressure CO_2 annealing compared to ridge CO_2 annealing.

Another considerable finding in Fig. 3-9(e) is the enhanced PCBM shoulder at 400 nm which is not seen on the other graphs with the thinner films and less PCBM concentrated samples which makes it clear that this shoulder is associated with PCBM structure introduced by further PCBM accumulation.

On the other hand, remarkable changes shown in Fig. 3-7(f) is most likely due to scattering effect where the increased PCBM concentration causes larger microclusters and surface roughness that is not seen up to that thickness and concentration. Because the surface migration of the larger amount of PCBM is known to create large roughness (Fig. 3-3(f-i)), the scattering effect is not observed in the same samples on absorbance mode (Fig. 3-10) which suggests that those remarkable changes in Fig. 3-9(f) is artificial.
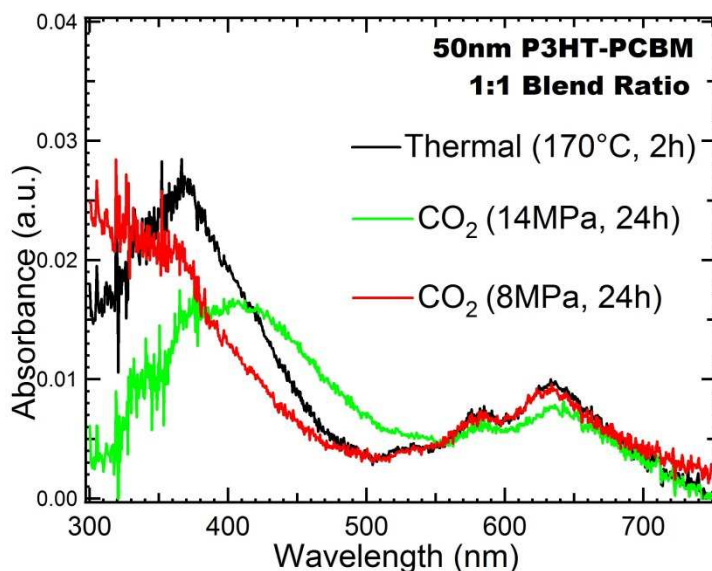
Figure 3- 10 Optical absorption of 50nm P3HT/PCBM films with (1:1) blend ratio after isothermal CO_2 (36˚C) annealing.

3.4.4. GID results
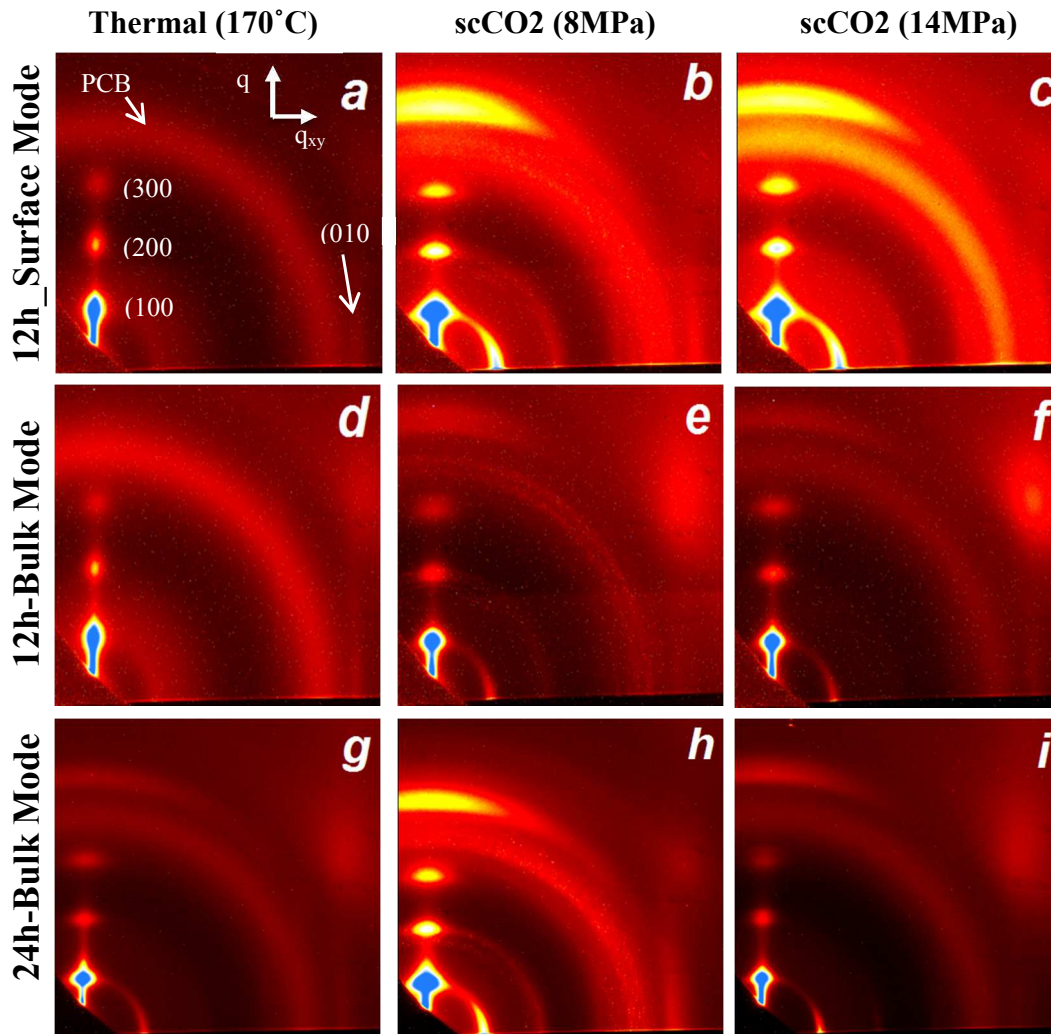
Figure 3- 11 2D GID images for the CO_2 (36°C) and thermal annealing treated P3HT/PCBM thin films (the original thickness of 50 nm) after expose to CO_2 at the ridge condition (a-c) 12h treatment (surface region) (d-f) 12h treatment (entire film region) (g-i) 24h treatment (entire film region)

Fig. 3-11 shows representative 2D diffraction patterns for the surface region and the entire film region of the CO_2 annealed and thermally annealed 50 nm P3HT/PCBM blend films at ambient temperature. The GID results from the surface and the entire film could be selectively

captured by changing incident beam angles, as discussed in Chapter 2. The results indicate not only crystal orientations but also structural differences between surface mode and bulk mode for the 8MPa and 14MPa $scCO_2$ blend films. This was also true for the different film thicknesses (25 and 100 nm in thickness). From the figure, the CO_2 annealed samples exhibit the surface effect where the PCBM surface migration is intensified at the density fluctuation ridge[36], which is consistent with the AFM and SEM results described above.

The thermal annealed and CO_2 annealed blend films at 14MPa exhibit Bragg reflections at around q=15 nm^{-1}, which is attributed to PCBM, and the intensities appear to be azimuthally uniform. The GID patterns in Fig 3-11 (b, e and h), on the other hand, give different structure and intensities for the PCBM diffraction, due to the PCBM crystallization shown as bright spots within diffraction rings.[1] Double rim diffractions (Fig. 3-11e and h) are also remarkable, indicating that both P3HT and PCBM possess varying domain sizes that refer to phase segregated and miscible regions. It should also be noted that the oriented enhanced crystallinity at the surface region can be expanded to the entire film with longer $scCO_2$ exposure time at 8MPa, as confirmed in Fig. 3-11(h) with the more equilibrium bulk film structure.

Fig. 3-12 shows the 1-d GID profiles along the q_z and q_{xy} directions. As discussed in Chapter 2, the quantitative analysis of the 1d scattering profiles using a Gaussian function, the peak position, peak intensity, and peak width were obtained. The lattice constants $a=2\pi/q_{z,0}$, and $b=2\pi/q_{xy,0}$ (Fig.2-8)[47] were calculated, and Scherrer equation ($L=(K\lambda)/(\beta\cos\theta$, K is the crystallite shape factor (=0.9), β is FWHM, θ is the scattering angle)[48] was used to obtain the crystalline size (L). The P3HT lattice parameters determined by sector integration of the respective P3HT Bragg peaks of (100), (200), (300) and (010) yield the lattice parameters as follows: a=1.69 nm and b=0.36 nm. In addition, the backbone chain orientation along the z direction improves

significantly with the CO_2 annealing especially at the ridge condition as compared to that with the thermal annealing. Hence, bright spots within PCBM Bragg peaks in fig. 3-11(e and h) are also noticeable corresponding to PCBM preferentially oriented crystals. Furthermore, the CO_2 annealed film at the ridge condition for an exposure time of 12h gives L=10.85 nm on the surface region and L=8.56 nm on the bulk region, both of which correspond to about 6 and 5 layers, respectively. In addition, for the longest CO_2 exposed (24 h) exposed blend films, the crystallite sizes in the entire film region increased to 10.52 nm (6 layers) as well. It should be emphasized that these sizes are much larger than that of the thermally annealed film (L= 6.96 nm at 170 °C for 24h,). A comparison of these results with the pristine P3HT films, the addition of PCBM distorts lamellar stacking regardless of the post-treatment methods. On the other hand, in the lateral direction, the (010) reflection, which corresponds to the intermolecular π-π stacking plane distance, becomes intensified especially after 24 h exposure of CO_2 at the ridge condition even in the presence of PCBM, which again can't be achieved by conventional thermal annealing or short CO_2 exposure treatments.
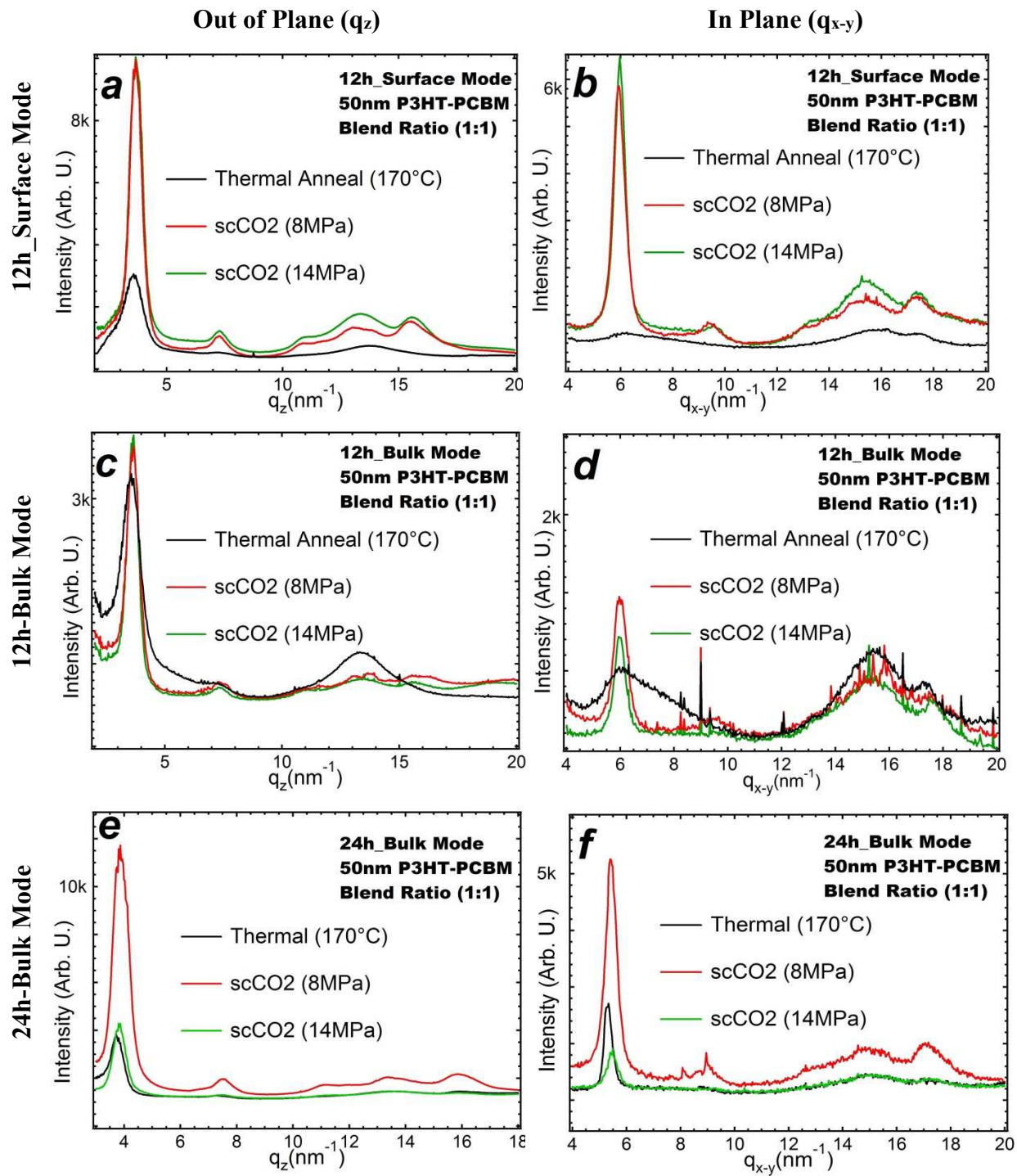
Figure 3- 12 GID profiles of the P3HT/PCBM thin films (the original thickness was 50 nm) along (left) the q_z and (right) q_{xy} directions after the CO_2 and thermal annealing (a,b) P3HT/PCBM surface region of 12h CO_2 (36˚C) and thermal (170˚C) annealing (c,d) P3HT/PCBM entire film region of 12h CO_2 (36˚C) and thermal (170˚C) annealing (e,f) P3HT/PCBM entire film region of 24h CO_2 (36˚C) and thermal (170˚C) annealing .

Figure 3- 13 Sketch demonstrating P3HT crystallization induced PCBM phase segregation on blend surface region a) thermal annealing sample b) high pressure scCO$_2$ sample c) fluctuation ridge scCO$_2$ sample

Figure 3-13 illustrates the proposed mechanism of the resultant P3HT-PCBM morphologies under conventional and CO$_2$ annealing. The existence of the broad azimuthal Bragg peaks shown in Fig. 3-11, i.e., (100), (200) and (300), the P3HT crystals indicate that large PCBM clusters formed upon phase segregation distort crystal orientations and this causes lamellar orientations shifted to in-plane direction, while the π-π orientations were shifted to out of the plane direction. This kind of transformation is specific to the CO$_2$ annealing that we did not observe azimuthal peaks for the thermal annealing samples. However, earlier reports suggested that similar transformation can be induced by a significant increase of PCBM concentrations[47]. According to the present results, the CO$_2$ induced phase segregation depends on the following two mechanisms: (i) the CO$_2$ induced plasticization increases polymer packing, resulting in a shrinking of lattice spacing, and thereby segregate to the PCBM particles out of the P3HT crystal region; (ii) around the density fluctuation ridge, PCBM nanoparticles are wetted with a CO$_2$ layer that attracts the PCBM particles toward the CO$_2$ rich region (i.e., the polymer/CO$_2$ interface). Therefore, as shown in Figure 3-13(c), the combination of the two

mechanisms promotes the phase segregation of the large PCBM clusters at the surface of the

P3HT/PCBM blend films (Fig. 3-7).

3.4.5. Conductivity results

I-V measurement is the most popular method for solar cell characterization. From the I-V

measurement result, it can be determined which parameter of the sample should be optimized the

solar cell to get higher efficiency. Basically for I-V characteristic measurements, voltage is

applied to electrodes of a solar cell and the current is measured. P3HT as a conjugated polymer

in exposure to oxygen and/or moisture results p-doped,[49, 50] and in such a circumstance it forms

Schottky contact with Al. When the Schottky barrier disappears at $V>V_{bi}$ (V_{bi}, built in potential),

it was reported that the device performance is controlled by active layer morphology due to

excess minority carriers.[51, 52]
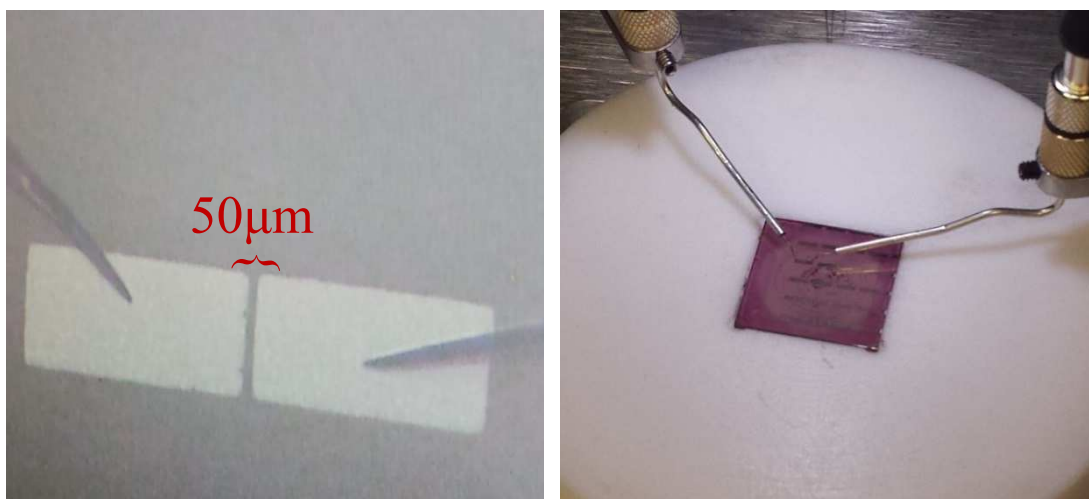
Figure 3- 14 50nm P3HT/PCBM device prepared for two probe device measurements, 100 nm Al top contacts with 50 μm spacing in between (left) to be measured in Agilent 4156C semiconductor parameter analyzer (right)

For the present device I-V measurements, devices with three different P3HT/PCBM blend ratios in two different solvents (toluene and chlorobenzene) were prepared by spin coating onto 0.7 mm glass substrates at 1500 rpm for 1 min. Each sample was rested for a day to remove residual solvents, and was subsequently treated with either $scCO_2$ or thermal annealing as desired. Finally, sample preparation was completed with 100 nm-thick Al contact vapor-deposited onto the blend film to measure the electron-acceptor electrical performance.
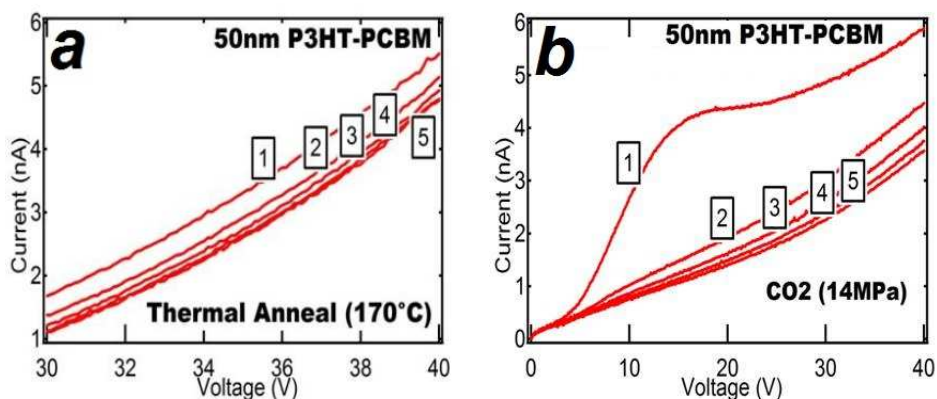
Figure 3- 15 Cyclic I-V measurements on one device until neutralizing light energy adsorbed during sample switch, a) 24h thermally annealed 50nm P3HT/PCBM solar device stabilizing on the 5th measurement b) $scCO_2$ (14MPa, 36˚C, 24h) annealed 50nm P3HT/PCBM solar device stabilizing on the 5th measurement

As shown in Fig. 3-14, each device was repeatedly applied bias before recording the final I-V data to damp residual light energy adsorbed during switching devices, and the numbers shown in each graph refer to the measurement order. In Fig. 3-14(b), the first I-V measurement was remarkably higher than other runs, indicating the excessive light adsorption during device switch. This might be due to a higher light adsorption ability of the P3HT/PCBM blend films treated by CO_2 at 14MPa (fig. 3-9(d-f)); hence for the high blend ratio (1:1) blend film surface structure caused scattering effect as shown in fig. 3-9(f) for high pressure (14MPa) CO_2 samples.

94
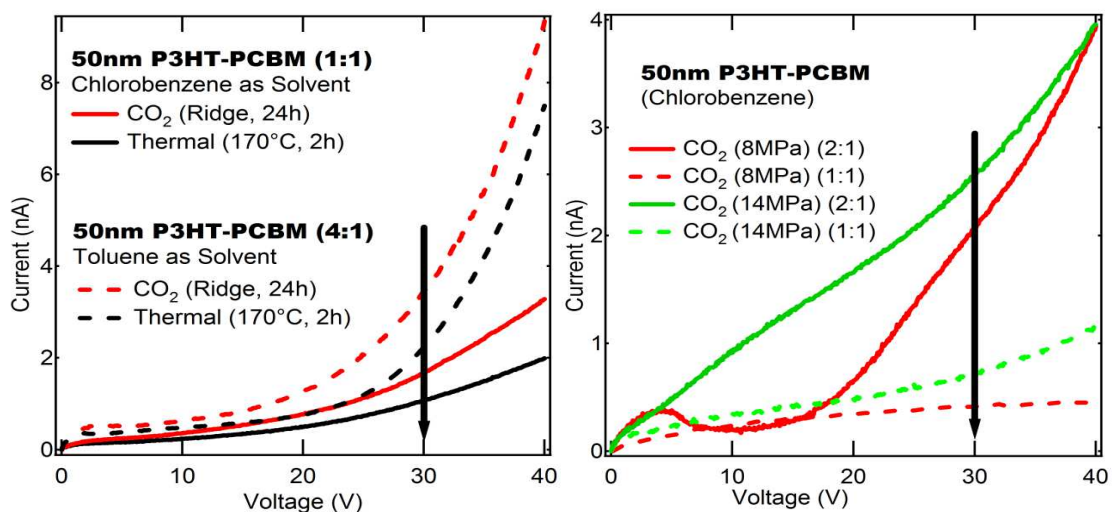
Figure 3- 16 Double linear I-V plots of 50nm P3HT/PCBM solvent dependence on thermal versus CO_2 annealing (left), and CO_2 pressure and PCBM concentration dependence (right)

Since the measurement of the solar cell is conducted in the dark, almost no current was flowing. The current increased as soon as charges were injected into the solar cell by the applied bias that was larger than the open circuit voltage. Effective parameters on the I-V characteristic of the P3HT/PCBM cell are interface`s conductivity, traps, recombination and charge carrier diffusion length. In Fig. 3-15, the I-V characteristics of the P3HT/PCBM blend film on the Al cathode is summarized as functions of the concentration dependence, CO_2 pressure, and solvents. The data extracted from the figure is tabulated in Table 3-1 for current responses of each device at 30V.

a)

I-V Response at 30V

	Chlorobenzene (1:1)	Toluene (4:1)
■ CO2 (8MPa)	1.68	3.45
■ Thermal (170C°)	1.06	2.23

b)

I-V Response at 30V

	Chlorobenzene (1:1)	Chlorobenzene (2:1)
■ CO2 (8MPa)	0.41	2.08
■ CO2 (14MPa)	0.72	2.56
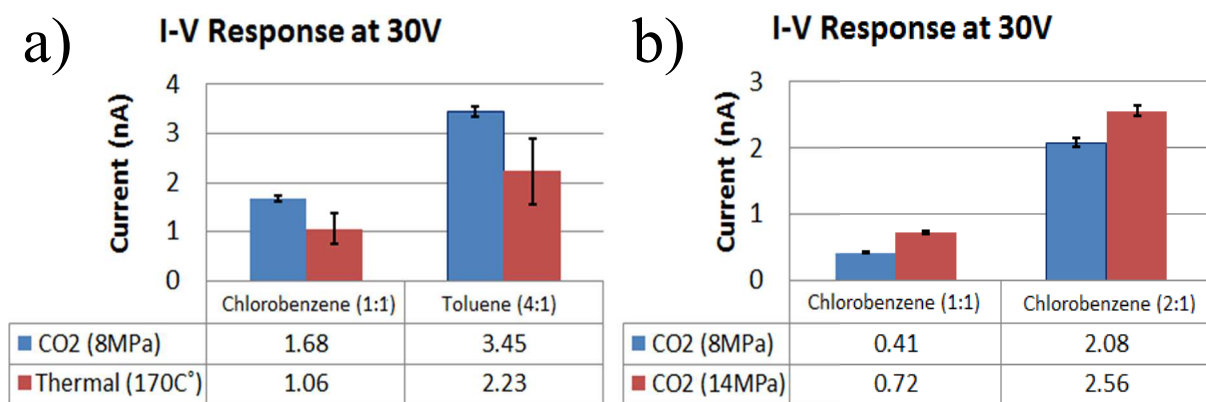
Figure 3- 17 Current responses at 30V for 50nm P3HT/ PCBM films a) scCO$_2$ and thermal annealed devices with Al contact vapor deposited at 5×10^{-7}torr b) scCO$_2$ annealed devices with Al contact vapor deposited at 2×10^{-6}torr.

The results showed that the CO$_2$ treated P3HT/PCBM blend generates higher current for applied bias regardless of CO$_2$ pressures than conventional thermal annealing. Hence, as shown in error bars, multiple device measurements from thermal and CO$_2$ treated samples revealed that device performance is more uniform on scCO$_2$ treated samples than thermal annealing samples. Again, this outcome might be due to the more homogenous surface coverage of PCBM microclusters on CO$_2$ treated samples. Furthermore, the best performance was achieved with the P3HT/PCBM devices of the (2:1) blend ratio treated with CO$_2$ at P=14MPa and 36°C for 24h. As we compared (2:1) and (1:1) blend samples, large crystal growth becomes obvious with increasing PCBM concentration (Fig. 3-4(c, f)), and the same trend is also followed by CO$_2$ exposure around density fluctuation ridge in comparison to high pressure (14MPa) CO$_2$ annealing. In conclusion, conductivity results however are not in favor of excessive PCBM cluster growth; therefore, results suggest that microcluster size distribution and surface coverage have critical importance.

3.5. Conclusion

In this study, pressure controlled CO_2 treatment at just above room temperature was applied to control morphologies of poly(3-hexylthiophene) (P3HT) and phenyl-C_{61}-butyric acid methyl ester (PCBM) blend thin films. Combined surface sensitive techniques including scanning electron microscopy (SEM), grazing incidence X-ray diffraction (GID), UV-vis spectroscopy, and optical microscopy, we found that the CO_2 treatments induce PCBM concentration gradient along the direction normal to the film surface by the excess CO_2 adsorption into the polymer matrix. The morphological changes after the CO_2 treatment were attributed to increased chain mobility, resulting in higher crystalline order of P3HT as discussed in chapter 2. In addition, we found that this polymer plasticization accelerates the crystallinity of the P3HT chains. As a result, the PCBM nanoparticles are pushed out from the inner chain conformations and are prone to migrate to the polymer-CO_2 interface where the excess amount of CO_2 molecules exists. The driving force for the surface migration is excess adsorption of CO_2 molecules on the nanoparticle surfaces, as discussed in Chapter 1: the CO_2-wetted nanoparticles preferentially migrate to the topmost CO_2-rich region through the concentration gradient.

We also discuss that this $scCO_2$ controlled phase segregation introduces better electrical response as deduced from device I-V performance. A comparison of the results between control sample (thermal) and CO_2 sample indicated that the $scCO_2$ induced PCBM rich layer can improve the device performance much better than a standard device composed of the P3HT/PCBM blend prepared by thermal annealing. Moreover, we found that the P3HT/PCBM morphology has stronger influence on device electron conductivity than polymer crystallinity. Our results offer great potential of the use of CO_2 as an alternative post-deposition treatment in order to control BHJ blend film morphology and electrical properties.

3.6. References

1.   P. Kohn, Z. X. Rong, K. H. Scherer, A. Sepe, M. Sommer, P. Muller-Buschbaum, R. H. Friend, U. Steiner and S. Huttner, Macromolecules **46** (10), 4002-4013 (2013).

2.   C. Deibel and V. Dyakonov, Rep Prog Phys **73** (9) (2010).

3.   C. W. Tang, Appl Phys Lett **48** (2), 183-185 (1986).

4.   P. E. Shaw, A. Ruseckas and I. D. W. Samuel, Adv Mater **20** (18), 3516-+ (2008).

5.   G. Yu, J. Gao, J. C. Hummelen, F. Wudl and A. J. Heeger, Science **270** (5243), 1789-1791 (1995).

6.   J. Gilot, M. M. Wienk and R. A. J. Janssen, Appl Phys Lett **90** (14) (2007).

7.   H. Hoppe, S. Shokhovets and G. Gobsch, Phys Status Solidi-R **1** (1), R40-R42 (2007).

8.   G. Li, V. Shrotriya, J. S. Huang, Y. Yao, T. Moriarty, K. Emery and Y. Yang, Nat Mater **4** (11), 864-868 (2005).

9.   A. Haugeneder, M. Neges, C. Kallinger, W. Spirkl, U. Lemmer, J. Feldmann, U. Scherf, E. Harth, A. Gugel and K. Mullen, Phys Rev B **59** (23), 15346-15351 (1999).

10.   N. S. Sariciftci, L. Smilowitz, A. J. Heeger and F. Wudl, Science **258** (5087), 1474-1476 (1992).

11.   Y. Kim, S. Cook, S. M. Tuladhar, S. A. Choulis, J. Nelson, J. R. Durrant, D. D. C. Bradley, M. Giles, I. Mcculloch, C. S. Ha and M. Ree, Nat Mater **5** (3), 197-203 (2006).

12.   R. Kokubu and Y. Yang, Phys Chem Chem Phys **14** (23), 8313-8318 (2012).

13.   S. van Bavel, E. Sourty, G. de With, K. Frolic and J. Loos, Macromolecules **42** (19), 7396-7403 (2009).

14.   P. Vanlaeke, A. Swinnen, I. Haeldermans, G. Vanhoyland, T. Aernouts, D. Cheyns, C. Deibel, J. D'Haen, P. Heremans, J. Poortmans and J. V. Manca, Sol Energ Mat Sol C **90** (14),

2150-2158 (2006).

15.	J. A. Barker, C. M. Ramsdale and N. C. Greenham, Phys Rev B **67** (7) (2003).

16.	S. S. van Bavel, E. Sourty, G. de With and J. Loos, Nano Lett **9** (2), 507-513 (2009).

17.	A. Kumar, G. Li, Z. R. Hong and Y. Yang, Nanotechnology **20** (16) (2009).

18.	B. Watts, W. J. Belcher, L. Thomsen, H. Ade and P. C. Dastoor, Macromolecules **42** (21), 8392-8397 (2009).

19.	W. Yin and M. Dadmun, Abstr Pap Am Chem S **242** (2011).

20.	M. Campoy-Quiles, T. Ferenczi, T. Agostinelli, P. G. Etchegoin, Y. Kim, T. D. Anthopoulos, P. N. Stavrinou, D. D. C. Bradley and J. Nelson, Nat Mater **7** (2), 158-164 (2008).

21.	D. A. Chen, A. Nakahara, D. G. Wei, D. Nordlund and T. P. Russell, Nano Lett **11** (2), 561-567 (2011).

22.	D. Chirvase, J. Parisi, J. C. Hummelen and V. Dyakonov, Nanotechnology **15** (9), 1317-1323 (2004).

23.	T. Erb, U. Zhokhavets, G. Gobsch, S. Raleva, B. Stuhn, P. Schilinsky, C. Waldauf and C. J. Brabec, Adv Funct Mater **15** (7), 1193-1196 (2005).

24.	J. H. Huang, F. C. Chien, P. L. Chen, K. C. Ho and C. W. Chu, Anal Chem **82** (5), 1669-1673 (2010).

25.	G. Li, Y. Yao, H. Yang, V. Shrotriya, G. Yang and Y. Yang, Adv Funct Mater **17** (10), 1636-1644 (2007).

26.	J. Peet, J. Y. Kim, N. E. Coates, W. L. Ma, D. Moses, A. J. Heeger and G. C. Bazan, Nat Mater **6** (7), 497-500 (2007).

27.	Y. Yao, J. H. Hou, Z. Xu, G. Li and Y. Yang, Adv Funct Mater **18** (12), 1783-1789 (2008).

28.	P. G. Karagiannidis, D. Georgiou, C. Pitsalidis, A. Laskarakis and S. Logothetidis, Mater

Chem Phys **129** (3), 1207-1213 (2011).

29.   H. Wang, E. D. Gomez, J. Kim, Z. L. Guan, C. Jaye, D. A. Fischer, A. Kahn and Y. L. Loo, Chem Mater **23** (8), 2020-2023 (2011).

30.   W. C. V. Wang, E. J. Kramer and W. H. Sachse, J Polym Sci Pol Phys **20** (8), 1371-1384 (1982).

31.   S. Blumel and G. H. Findenegg, Phys Rev Lett **54** (5), 447-450 (1985).

32.   J. R. Strubinger, H. C. Song and J. F. Parcher, Anal Chem **63** (2), 98-103 (1991).

33.   J. Y. Lee, G. A. Buxton and A. C. Balazs, J Chem Phys **121** (11), 5531-5540 (2004).

34.   J. Y. Lee, Q. L. Zhang, T. Emrick and A. J. Crosby, Macromolecules **39** (21), 7392-7396 (2006).

35.   S. Tyagi, J. Y. Lee, G. A. Buxton and A. C. Balazs, Macromolecules **37** (24), 9160-9168 (2004).

36.   T. Koga, Y. S. Seo, Y. M. Zhang, K. Shin, K. Kusano, K. Nishikawa, M. H. Rafailovich, J. C. Sokolov, B. Chu, D. Peiffer, R. Occhiogrosso and S. K. Satija, Phys Rev Lett **89** (12) (2002).

37.   X. X. Li and B. D. Vogt, J. Supercrit. Fluids **51** (2), 256-263 (2009).

38.   X. X. Li and B. D. Vogt, Polymer **50** (17), 4182-4188 (2009).

39.   K. Shin, X. Hu, X. Zheng, M. H. Rafailovich, J. C. Sokolov, V. Zaitsev and S. A. Schwarz, Macromolecules **34**, 4993 (2001).

40.   H. W. Ro, B. Akgun, B. T. O'Connor, M. Hammond, R. J. Kline, C. R. Snyder, S. K. Satija, A. L. Ayzner, M. F. Toney, C. L. Soles and D. M. DeLongchamp, Macromolecules **45** (16), 6587-6599 (2012).

41.   T. Koga, Y. S. Seo, Y. Zhang, K. Shin, K. Kusano, K. Nishikawa, M. H. Rafailovich, J. C.

Sokolov, B. Chu, D. Peiffer, R. Occhiogrosso and S. K. Satija, Phys. Rev. Lett. **89**, 125506 (2002).

42.   M. Asada, P. Gin, M. K. Endoh, S. K. Satija, T. Taniguchi and T. Koga, Soft Matter **7** (19), 9231-9238 (2011).

43.   M. D. Cohen and E. Fischer, J Chem Soc (Aug), 3044-& (1962).

44.   S. S. van Bavel, M. Barenklau, G. de With, H. Hoppe and J. Loos, Adv Funct Mater **20** (9), 1458-1463 (2010).

45.   P. J. Brown, D. S. Thomas, A. Kohler, J. S. Wilson, J. S. Kim, C. M. Ramsdale, H. Sirringhaus and R. H. Friend, Phys Rev B **67** (6) (2003).

46.   Y. Kim, S. A. Choulis, J. Nelson, D. D. C. Bradley, S. Cook and J. R. Durrant, Appl Phys Lett **86** (6) (2005).

47.   P. Kohn, Z. Rong, K. H. Scherer, A. Sepe, M. Sommer, P. Müller-Buschbaum, R. H. Friend, U. Steiner and S. Hüttner, Macromolecules **46**, 4002-4013 (2013).

48.   P. Scherrer, Nachr. Ges. Wiss. Göttingen **26**, 98-100 (1918).

49.   M. S. A. Abdou, F. P. Orfino, Y. Son and S. Holdcroft, J Am Chem Soc **119** (19), 4518-4524 (1997).

50.   S. Hoshino, M. Yoshida, S. Uemura, T. Kodzasa, N. Takada, T. Kamata and K. Yase, J Appl Phys **95** (9), 5088-5093 (2004).

51.   J. Bisquert, D. Cahen, G. Hodes, S. Ruhle and A. Zaban, J Phys Chem B **108** (24), 8106-8118 (2004).

52.   I. Mora-Sero, Y. Luo, G. Garcia-Belmonte, J. Bisquert, D. Munoz, C. Voz, J. Puigdollers and R. Alcubilla, Sol Energ Mat Sol C **92** (4), 505-509 (2008).

4. Chapter 4: Nanoscale adsorbed structures of P3HT chains on impenetrable solids

4.1. Abstract

The objective of this Chapter is to experimentally reveal the formation of adsorbed nanolayers on substrate surfaces that control film stability and crystalline structures of thin polymer films. Thin polymer films on solids are found in a variety of technological fields such as protective coatings, lubricants, decorative paints, and adhesion layers to achieve desired interfacial properties of solids. Owing to strong demands for new nanotechnologies, many sophisticated devices are now shifting towards nanometer scales while maintaining their exceptional performance properties. When the thickness of a polymer film approaches the radius of gyration of a random coil (R_g), the conformation of the chain molecules is greatly affected due to the compression of the random coils along the confinement direction. This confinement effect[1] results in various deviations in the properties and structures from the bulk such as viscoelastic property[2-5], glass transition[1, 6-9], interdiffusion[10, 11], physical aging[12-14], elastic modules[15, 16], and crystallization[17-19]. Very recently, Tang and co-authors further predicted that there is a new confinement length scale in thin polymer films that controls physical aging of glassy polymer films[20]: the origin is the sliding motion of short chain fragments along chain molecules[21, 22]. Molecular scale descriptions of the chain conformations at the solid-polymer interface have just been brought to light, but little is known about the structure–property relationship that is essential not only to unveil the origins of various unusual/novel behaviors, but also to design polymer-based advanced nano-devices and nanostructures.

In this chapter, I focused on P3HT adsorbed nanolayers formed onto Si substrates via a thermal annealing process before the use of the post-CO_2 annealing process described in Chapters 2 and 3. Stimulatingly, there is now growing evidence to suggest that the effects of the

adsorbed nanolayers overcome the effects of a "surface mobile layer" at the polymer-air interface[6-8, 23, 24], resulting in long-range perturbations (from the substrate surface) on local structures and properties of ultrathin polymer films[5, 25-27]. As schematically shown in Fig. 4-3, when molecular weight (M_w) of a polymer is beyond a critical value, the adsorbed nanolayers are found to consist of two different chain conformations: flattened chains that constitute the inner higher density region of the adsorbed nanolayer and loosely adsorbed polymer chains that form the outer bulk-like density region. It is evidenced that this two-layer formation is attributed to piecemeal deposition with differential spreading dictated by the still-uncovered surface area[27-29]. On the other hand, below the critical M_w, the flattened chains are mainly formed on a solid surface. This can be explained by the scaling treatment of adsorption kinetics[30, 31]: the surface coverage of early arriving chains that lie flat on the surface (i.e., the flattened chains) is a decreasing function of M_W (below the critical M_W) such that more free surface areas are available for late arriving chains that form bridges jointing up nearby empty sites (i.e., the loosely adsorbed chains). In addition, we recently found that these adsorbed chains interact (or entangle) with free chains (in the bulk of the film) differently, resulting in opposing roles in film stability of thin polymer films[32].

4.2. Introduction

4.2.1. General background

A spin-coating process is a well-established technique to prepare homogenous polymer thin films on planar solids. But, it is known that this rapid solvent evaporation process results in non-equilibrium stressed conformations of polymer chains on solids and such residual stress causes film instability[33-35] and changes in properties of polymer thin films[36, 37]. In order to

eliminate the residual stress, prolonged thermal annealing (at temperatures far above T_g) is typically required[35, 36, 38]. Aside from equilibration, it is also evidenced that such thermal annealing expedites polymer adsorption onto even weakly attractive solids[39, 40]. This can be explained by the fact that the total enthalpic gain due to an increase in the number of surface-segmental contacts overcomes a loss in the conformational entropy of the chain during the transition from a randomly coiled state to an adsorbed state[40, 41]. Guiselin[42] proposed the experimental procedure to unveil the irreversibly adsorbed polymer layer (so-called "Guiselin brushes" composed of a mixture of tail and loop segment sequences[40, 43]): One has to equilibrate the melt or dense solution against a solid surface; The unadsorbed chains can then be removed by a good solvent, while the adsorbed chains are assumed to maintain the same conformation due to the irreversible freezing they experience through many physical solid-segment contacts (Fig.4-1).

Fabrication of a polymer film (via spin-cast or solution cast)

Annealed at $T>>T_g$

Rinsed with a good solvent
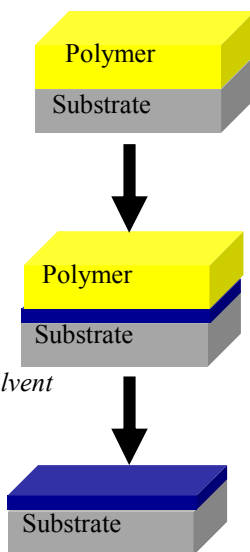
Residue layer (adsorbed nanolayer)

Figure 4- 1 Schematic diagram of the formation of the polymer adsorbed nanolayers on a solid substrate.

Despite experimental difficulties, several research groups have already demonstrated that Guiselin's approach is practical for various homopolymers, revealing the presence of the adsorbed nanolayers onto planar surfaces[5, 25, 27-29, 39, 44-49]. The formation of the adsorbed nanolayer has been reported on various nanoparticle surfaces as well[50-57]. Interestingly, Kumar and co-workers have shown that the adsorbed nanolayer can be significantly thinner around nanoparticles than at chemically similar planar solid surfaces[56]. Very recently, our group found that the adsorbed polybutadiene (PB) nanolayer on carbon black filler surfaces swells in a good solvent, displaying a parabolic profile with a diffuse tail[58]. Furthermore, the neutron spin echo results indicated the collective dynamics of the swollen chains that can be explained by the so-called "breathing mode"[59].

4.2.2. Nanoscale structures of the two different adsorbed chains

Here I briefly explain our recent experimental findings in the structures and the formation process of the adsorbed nanolayers. The details have been described in our recent book chapter[60]. We used PS as a model system and prepared the adsorbed nanolayers on Si substrates using Guiselin's approach. Si wafers were pre-cleaned using a hot piranha solution for 30 min, and were subsequently rinsed with deionized water thoroughly. We confirmed that the native oxide (SiO_x) layer after the piranha solution cleaning had a thickness of 2.4 nm on the Si (hereafter assigned as "non-treated Si"). The water contact angle of the non-treated Si (just before spin-coating of polymer films) was estimated to be less than 10º. In order to change the surface attraction of the polymer, the non-treated Si wafers were further immersed in an aqueous solution of hydrogen fluoride (HF) for 20 s to remove the SiO_x layer (hereafter assigned as "HF-etched Si"). It should be noted that a thin SiO_x layer of 1.3 nm in thickness was, however, reproduced

even immediately after HF etching, possibly due to atmospheric oxygen and moisture[29, 61]. The water contact angle of the HF-etched Si was determined to be $80 \pm 1°$. Hence, the HF-etched Si has a very different hydrophobicity when compared to the non-treated Si. Spin-cast PS films ($\approx$ 50 nm in thickness) prepared on the HF-etched Si substrates were first annealed at 150 °C for a long period of time (up to 200 h) and then solvent leached with toluene at room temperature repeatedly until the thickness of the residual layer remained unchanged. The final residual layers (i.e., the adsorbed nanolayers) were further dried under vacuum at 150 °C to remove any excess solvent trapped in the films. X-ray reflectivity (XR) in conjunction with a Fourier transformation method, a powerful tool to evaluate detailed structures for low x-ray contrast polymer multilayers[62-64], was used to obtain important data related to the details of the film structures.

Figure 4- 2 XR curves of the PS (M_w=290 kDa) interfacial sublayer (red circles) and flattened layer (blue circles) at t_{an}=100 h. The solid lines correspond to the best-fits to the data based on the dispersion (δ) profiles against the distance (z) from the SiO_x surface shown in the inset: red line: the interfacial sublayer; blue line: the flattened layer. The dotted line in the inset corresponds to the δ value of bulk PS. Note that the δ value of the lone flattened layer is smaller than that within the interfacial sublayer due to the empty (air) spaces of the film (Fig. 4-3).

Fig. 4-2 shows the XR curve of the PS residue layer (indicated in red) formed after the annealing time (t_{an}) = 100 h and toluene leaching process. The corresponding best fit (shown in the solid black line in Fig. 4-2) to the XR data was obtained by using a four-layer (a Si substrate, a SiO_x layer, and two PS layers with different densities) (the inset of Fig. 4-2). The choice of this layer model was determined by the corresponding Fourier transformation (FT) profile of the XR profile. The details of the FT method for low-contrast multilayer films have been described elsewhere[28]. Note that the $\Delta\delta$ value of the bulk PS with the X-ray energy of 14.2 keV is δ_{bulk} =1.14×10^{-6}. Hence, The XR results showed that the adsorbed nanolayers ($M_w \geq$ 123kDa) are composed of two distinct density regions in the direction normal to the film surface: the inner higher-density region (~ 10 % higher than the bulk) composed of the flattened chains with about 2 nm in thickness regardless of M_w and the outer bulk-like density region whose thickness increases with increasing M_w[28, 29, 32, 60] (Fig. 4-3).
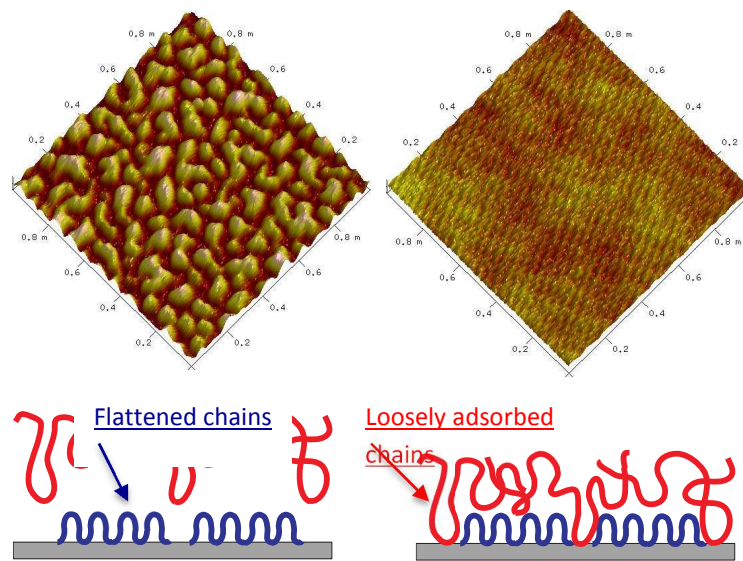

Figure 4- 3 AFM height images of (left) the PS (M_w = 290 kDa) flattened layer surface and (right) interfacial sublayer surface at t_{an} = 100 h. The scan sizes and height scales of the images are 1 μm × 1 μm and 0 - 6 nm, respectively. The bottom two cartons are the proposed chain conformations of the flattened layer (left) and interfacial sublayer (right), respectively.

The insensitivity of the thickness of the inner flattened chains to M_w can be drawn by a counterbalance between the conformational entropy of the chains and the energy gain of the attached segments to the surface in the total free energy[28, 41]. The formation of the flattened layer on a planar substrate is also consistent with the Brownian dynamic simulation results[65]: flexible homopolymer chains tend to orient their conformations parallel to the surface and form a compact, higher density layer relative to the bulk in equilibrium. Furthermore, we found that solvent leaching with chloroform (a better solvent than toluene for PS) allows for the unveiling of the lone inner high-density region[29]. This selective extraction of the two adsorbed layers is attributed to the large difference in desorption energy between the outer loosely adsorbed chains and the inner flattened chains, which is proportional to the number of segment-surface contacts[31, 66]. Hereafter, we assign the adsorbed nanolayer composed of the inner flattened chains and outer loosely adsorbed chains as an "interfacial sublayer", while the adsorbed nanolayer composed of the lone flattened chains is assigned as a "flattened layer"[29], unless otherwise stated.

Fig. 4-3 shows representative surface morphologies of the PS flattened layer and the PS interfacial sublayer after achieving the "quasiequilibrium" state (i.e., the final adsorbed layers whose thickness remains unchanged against annealing time (t_{an}) at $t_{an} > t_q$, as shown in Fig. 4-3. From the figure we can see that the flattened layer has microscopic "textures" with a characteristic length of about 100 nm, while the surface of the interfacial sublayer is homogeneous. It is hence reasonable to suppose that the empty regions of the flattened layer correspond to the sites where the loosely adsorbed chains grew and were then removed by the chloroform leaching. In addition, as summarized in Fig. 4-4, the two different chain architectures emerge and grow independently on the solid surface[29], while the time scale for the initial nucleation and growth of the flattened chains is predicted to be only a few hundred

nanoseconds[65, 67]. Our group has also revealed that this two-layer formation is general regardless of the choice of polymers with respect to varying surface-segment interactions and intramolecular architectures[26, 29]. Furthermore, it was found that the surface coverage of the quasiequilibrium flattened layer increases with increasing the magnitude of solid-segment interactions: the surface coverage follows poly(2-vinylpyridine) (P2VP) > poly(methyl methacrylate) (PMMA) > PS with the nearly same M_w on the same substrate[29].
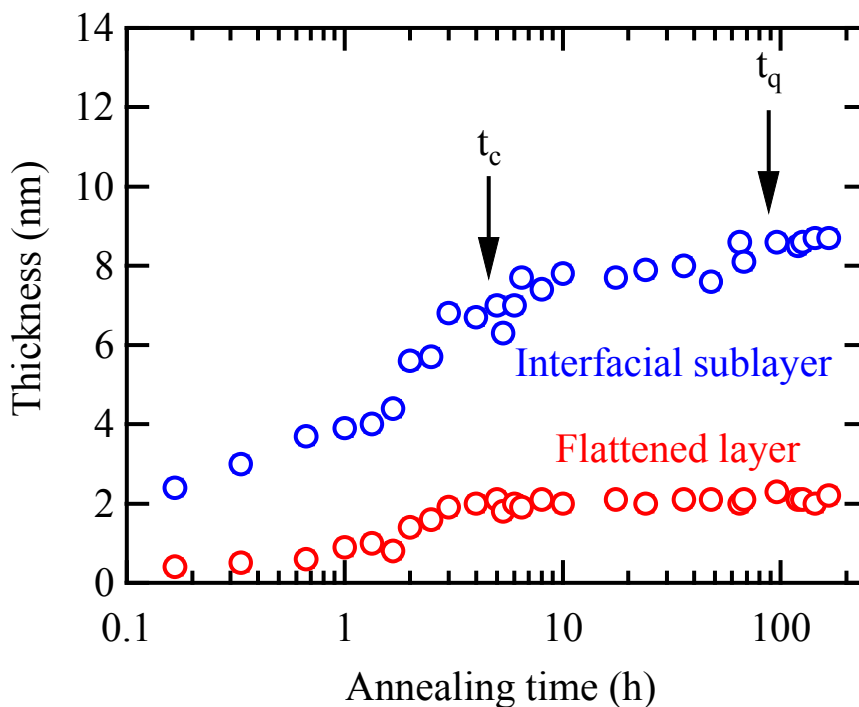
Figure 4- 4 Growth curves of the PS (M_w = 290 kDa) interfacial sublayer (blue circles) and flattened layer (red circles) against t_{an} at 150 °C measured by XR. The crossover time (t_c) from the power-law growth to logarithmic growth for the interfacial sublayer is indicated by the left arrow. The final adsorption time to reach a plateau (i.e., the quasiequilibrium state) in the growth curve is indicated as t_q.

4.2.3. Adsorbed Semicrystalline Polymer Nanolayers

The adsorption of semicrystalline polymers at the polymer melt-solid interface is another interesting question to be answered. In our recent study[26], 50 nm-thick PEO films (M_w = 20 kDa) were spin-coated onto HF-etched Si substrates and pre-annealed at T = 85 °C > T_m (64 °C) for 2 h to induce the irreversible adsorption of the PEO chains on the substrate. To investigate the adsorbed nanolayers in detail, the annealed samples were solvent leached with fresh chlorobenzene repeatedly. The adsorbed nanolayers were then post-annealed at 85 °C for 1 h to remove any excess solvent trapped in the films.

Figure 4- 5 AFM topographic images of the PEO (a) interfacial sublayers and (b) flattened layer. The samples were annealed at 85 °C for 1 h and rapidly quenched to 25 °C to induce the recrystallization. The corresponding one-dimensional GID results are shown in (c). The presence of the 120 diffraction peak at q = 13.6 nm^{-1} was used to determine the existence of the crystalline structure.

110

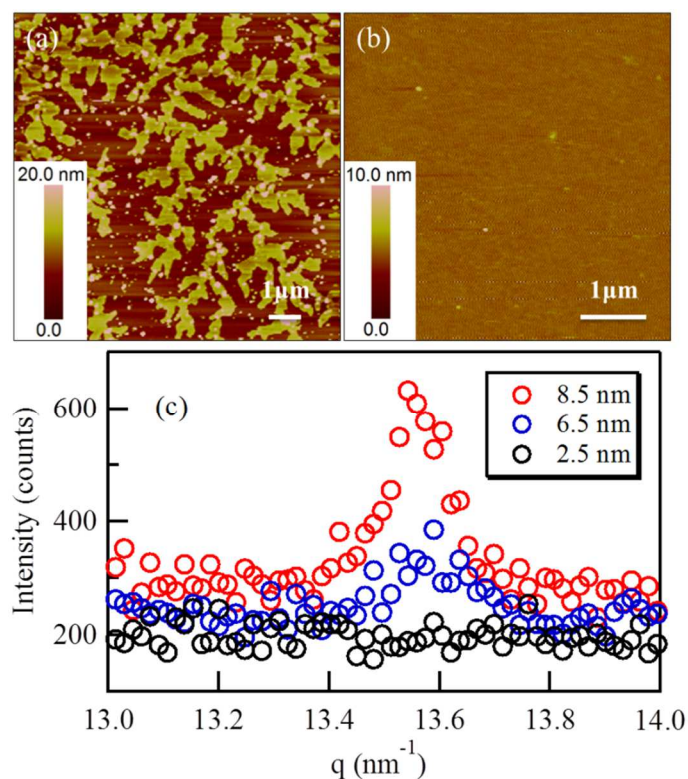Fig. 4.5 shows representative AFM height images of the PEO adsorbed nanolayers after a series of leaching experiments. As seen from the figure, finger-like seaweed lamellar structures produced via the DLA process are seen in the 6.5 nm-thick interfacial sublayer, while the surface of the 2.5 nm-thick flattened layer is featureless (i.e., no crystalline structures were observed). Grazing incidence X-ray diffraction (GID) measurements with a high brilliant synchrotron x-ray beams at SPring-8 (Japan) also confirmed that there is no crystalline structure formed in the 2.5 nm-thick residual layer (Fig. 5 (c)). Hence, it is reasonable to conclude that the PEO flattened chains are strongly bound to the solid such that they are not able to crystallize, while the loosely adsorbed PEO polymer chains can fold and grow via the DLA process. We also found that in the case of PEO chains on the HF-etched Si (a strongly attractive interaction), the chains adopt a flat-on orientation on the substrate[26]. On the other hand, polyethylene (PE) chains prefer to have an edge-on orientation on the HF-etched Si[25] (i.e., a weak interaction). These results are in good agreement with previous Monte Carlo simulations[68] and experimental results [69].

4.3.   Materials and Methods

4.3.1. Sample Preparation

A regioregular P3HT (M_w=54kDa-75kDa) was purchased from American Dye Source. The polymer was dissolved in a good solvent (chlorobenzene) with polymer concentrations of about 1 wt% and the solution was filtered through a 0.45μm pore-size filter. [6,6]-Phenyl C_{61} butyric acid methyl ester (PCBM, the average particle size of about 2nm) was used for this study. For P3HT/PCBM blend films, the PCBM particles at weight ratios of 1:1 and 4:1 (P3HT:PCBM) were added to the polymer solutions. Si substrates were cleaned by immersion in a hot piranha solution (i.e., a mixture of H_2SO_4 and H_2O_2, *caution: a piranha solution is highly corrosive upon*

contact with skin or eyes and is an explosion hazard when mixed with organic chemicals/materials; Extreme care should be taken when handing it) for 30 min, and subsequently rinsed with deionized water thoroughly. Then, only for PS thin films, we used an aqueous solution of hydrogen fluoride (HF) to remove a native oxide layer on Si substrates. Hereafter, we assign hydrogen passivated Si substrates and Si without the HF treatment as H-Si and B-Si, respectively. It should be noted that a SiO_2 layer of about 1.5 nm in thickness was reproduced even just after HF etching due to atmospheric oxygen and moisture[61]. However, the surface tension (γ) of the H-Si is quite different (38.1 mJ/m^2 for the dispersion part (γ_d) and 6.14 mJ/m^2 for the polar part (γ_p)) from that of the B-Si ($\gamma_d = 25.8$ mJ/m^2 and $\gamma_p = 25.8$ mJ/m^2)[70].

To prepare the final flattened layers and interfacial sublayers composed of the pure P3HT or P3HT/PCBM blend, we reproduced the established protocol[71]: Approximately 50 nm-thick spin cast films prepared on either H-Si or B-Si substrates were annealed at high temperatures (170 °C) for long time (typically 48 h) under vacuum below 10^{-3} Torr. As discussed above, the leaching conditions used (type of a solvent, leaching time, leaching temperature etc.) should be optimized; otherwise we might end up with the formation of the loosely adsorbed layers. This selective extraction of the two adsorbed layers is possible owing to the large difference in the desorption energy between the outer loosely adsorbed chains and the flattened chains, which is proportional to the number of segment-surface contacts.[72, 73] The films were leached in baths of a fresh good solvent (chlorobenzene) at 65 °C for extraction of the interfacial sublayer and 65 °C for extraction of the flattened layer. The resultant interfacial sublayer and flattened layers were dried in a vacuum oven at 150 °C for 24 h to remove any excess solvent trapped in the films.

4.3.2. Atomic force microscopy (AFM)

AFM (Agilent AFM 5500, Bruker Bioscope Catalyst and Digital Nanoscope III) was used to study the surface morphologies of the adsorbed layers and thin films. A standard tapping mode was conducted in air by using a cantilever with a spring constant of about 40 N/m and a resonant frequency of about 300 kHz. The scan rate was 0.5-1.0 Hz with a scanning density of 256-512 lines per frame.

4.3.3. Grazing Incidence X-ray Diffraction (GID)

The grazing incidence x-ray diffraction (GID) measurements for the CO_2-treated and thermally annealed PEO thin films were carried out at the X9 beamline at the National Synchrotron Light Source (NSLS) and the CHX beamline at the NSLS-II, Brookhaven National Laboratory (BNL). Two dimensional diffraction patterns were measured with a CCD camera (Princeton Instruments) with an incident x-ray angle of 0.2°, which is above the critical angle of P3HT, hence illuminating the entire P3HT adsorbed layers. The x-ray wavelengths (λ) were 0.0879 nm at x9 and 0.1377 nm at CHX, respectively. The GID experiments were carried out at room temperature.

4.3.4. X-ray Reflectivity (XR)

XR experiments were performed under ambient conditions at the X20A beamline of the National Synchrotron Light Source, Brookhaven National Laboratory. The specular reflectivity was measured as a function of the scattering vector in the direction perpendicular to the surface, $q_z = 4\pi\sin\theta/\lambda$, where θ is the incident angle and λ is the x-ray wavelength ($\lambda = 0.110$ nm, which is

equivalent to the X-ray energies of 10.5 keV). The XR data was fit by using a standard multilayer fitting routine for a dispersion value (δ in the X-ray refractive index) in conjunction with a Fourier transformation (FT) method, a powerful tool to obtain detailed structures for low X-ray contrast polymer multilayers[62].

4.3.5. Ellipsometry experiments

The thicknesses of the adsorbed layers were measured by an ellipsometer (Rudolf Auto EL-II) with a fixed refractive index of 1.45.

4.4. Results and Discussion

4.4.1. P3HT adsorbed layers

Fig. 4-6 shows a representative XR result for the P3HT flattened layer on the H-Si substrate (annealed at 170 °C for 72h). The corresponding best fit (shown in the solid line in Fig. 4-6) to the XR data was obtained by using a three-layer (a Si substrate, a SiO_x layer, and a P3HT layer) dispersion (δ) model for the flattened layer shown in the inset. From independent XR measurements using the H-Si substrate, the thickness of the SiO_x layer was determined to be 1.5 nm. The XR results gave the thicknesses of the interfacial sublayer and flattened layer as 10.0 nm and 3.5 nm, respectively. In addition, as shown in the inset, the dispersion value, which is proportional to the density of the layer, is estimated to be nearly half of the bulk P3HT thin film. To understand the film structure in more detail, AFM was used.

Fig. 4-7 shows the AFM height image of the (a) interfacial sublayer and (b) the flattened layer. From the figures we can see not only the interfacial sublayer but also flattened layer covered the Si substrates completely, indicating that the attractive interaction between the P3HT

114

and H-Si is strong, as previously seen in the P2VP/B-Si system[29]. From the images, it is also indicative that the interfacial sublayer has a rougher surface, implying that the formation of the crystalline structures even near the substrate interface. We will discuss this point later. At the same time, as shown in Fig. 4-8, the flattened layer has "dimple" structures with several tens of nanometers in size and an average height of about 3 nm at the air surface. Based on the phase image shown in Fig. 4-8 (right), it is likely that the dimple structures are composed of the same P3HT since there are no (phase) contrasts in the image.
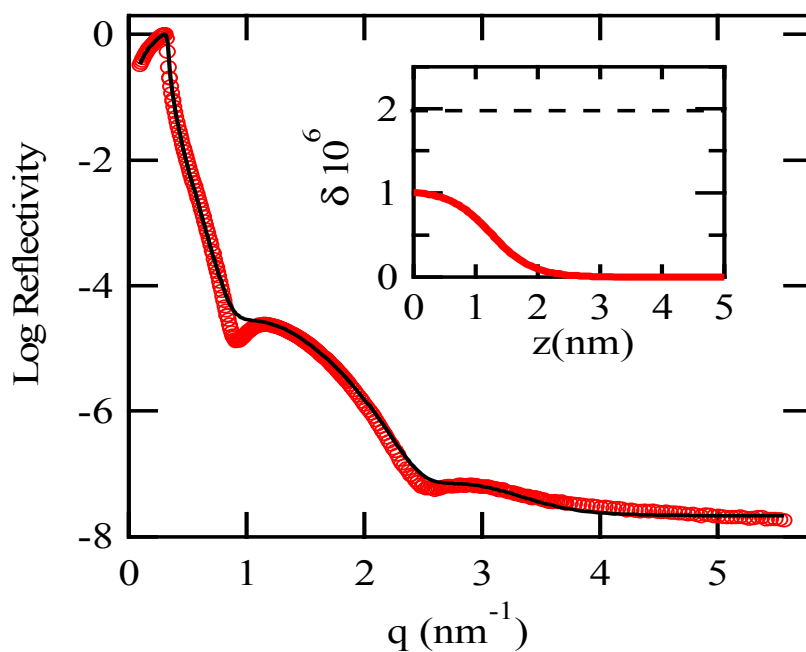
Figure 4- 6 XR curve of the P3HT flattened layer on H-Si. The solid line corresponds to the best-fit to the data based on the dispersion (δ) profile against the distance (z) from the SiOx surface shown in the inset. The δ value of the bulk P3HT is 1.98×10^{-6} (shown by the dotted line).

We also confirmed that the dimple structures exist everywhere in the flattened layer. Since the dimple structures are less than the coherent length (ξ) of X-ray beams at the sample position ($\xi_{surface} \sim 20$ μm in the present case), X-rays would interfere with the textures, possibly

causing a drastic change in the "amplitude" of the Kiessig oscillating fringes. This would make accuracy of the data fitting (for the density and roughness of the flattened layer) somewhat ambiguous, while the thickness is still independently and accurately determined from the "period" of the oscillation fringes
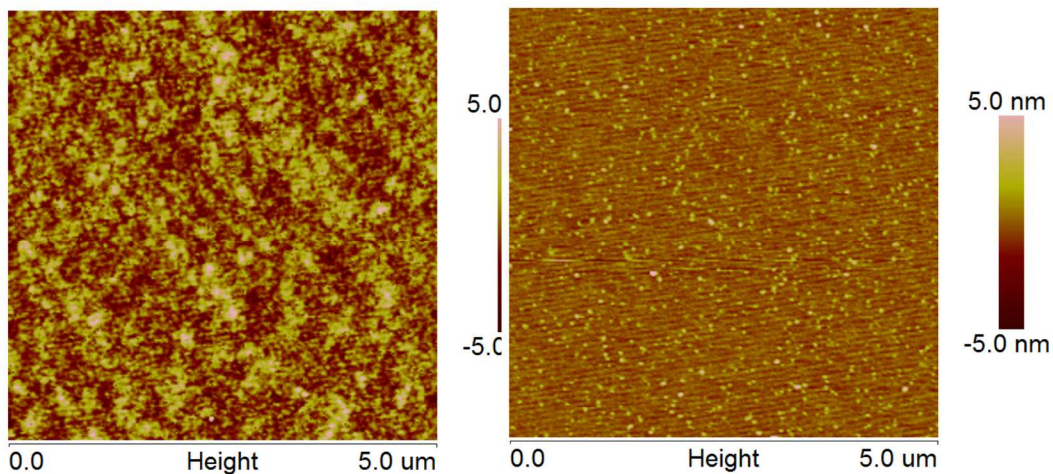

Figure 4- 7 AFM height images of (left) the height image and (b) phase image of the P3HT flattened layer. The left image is an expanded view of Fig. 4-7.
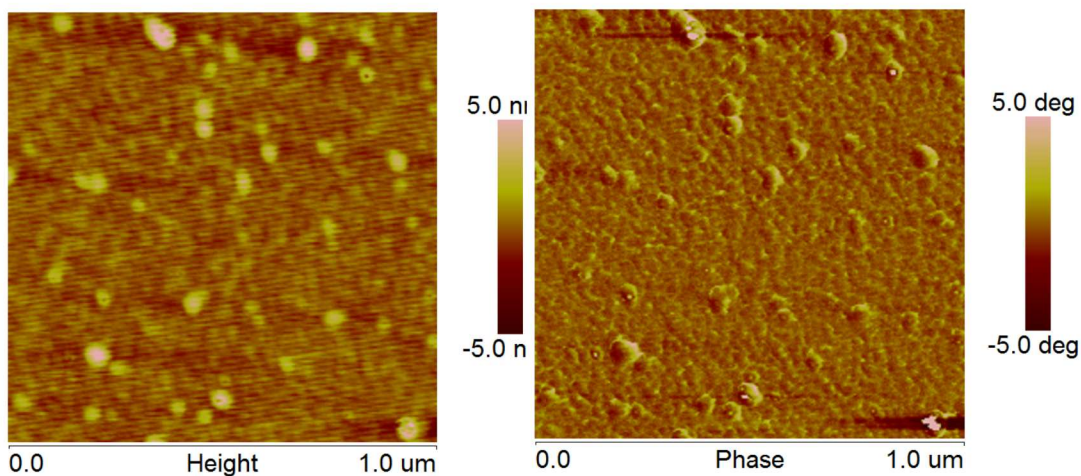

Figure 4- 8 AFM height images of (left) the P3HT interfacial sublayer surface at t_{an} = 48 h and (b) the flattened layer surface.

One possibility to explain the dimple structures is the presence of different chain conformations on the substrate. It is predicted that there are three different chain confirmations on a substrate: "edge-on", "vertical", and "face-on" (Fig. 4-9). Hence, it may be possible that a coexistence of these domains on the substrate. According to Berthelot's combining rule, the interfacial tension (γ_{ls}) is calculated as follows:

$$\gamma_{ls} = \gamma_l + \gamma_s - 2\left(\gamma_s \; \gamma_l \; \right)^{1/2}, \tag{1}$$

where γ_s and γ_l are the surface energies of the solid and liquid, respectively. The surface tension of thiophene is 32 mN/m, while the surface tension of C_6H_{13} is unclear. Here we assumed that the surface tension of C_6H_{13} is identical to that of heptane (C_6H_{14}, γ =17.5 mN/m at 30°C[74]). With these values, we calculated the interfacial energies to be 6 mN/m for C_6H_{13}/H-Si and 1.0 mN/m for thiophene/H-Si. Hence, the thiophene/H-Si interaction is more favorable than C_6H_{13}/H-Si, implying the formation of the face-on orientation. However, it is difficult for AFM to visualize the orientations of the crystalline structures. In order to quantify the crystalline structures and chain orientations of these adsorbed layers, GID experiments were performed.

Fig. 4-10 shows 2-d GID images of the interfacial sublayer and flattened layer. From the images, we can see (100), (200) and (300) Bragg reflections along the q_z direction. This indicates that the π-conjugated polymer chains adsorbed on the H-Si surface still self-assemble with a predominant "edge-on" orientation of planarized backbone with respect to the substrate surface (Fig. 4-9[75]).
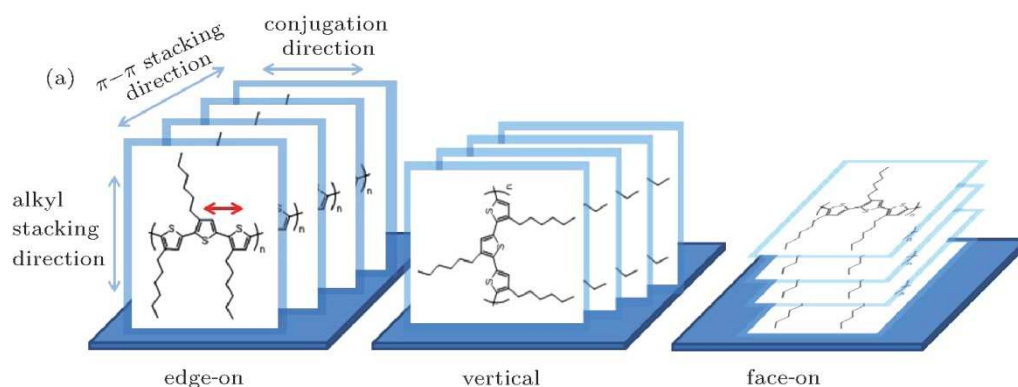
Figure 4- 9 Three typical P3HT chain orientations, edge-on, face-on, and vertical, where the lattice constants *a*, *b*, *c* are the distance between backbones (1.69 nm), stacking distance (0.78 nm), and distance between side chains (0.78 nm), respectively. Data from Xing et al. (Ref. 75).

We postulate that the polymer chains orient near the substrate in such a way that the alkane side chains can also adsorb on a substrate surface to increase the solid-segment contacts, overcoming the conformational entropy loss of the polymer chains in such a confined geromety[28, 41]. Based on the Bragg peak positions in the 1d GID profile (Fig. 4-11), we estimated the intermolecular backbone layer distance to be 1.71±0.02 nm for both the interfacial sublayer and flattened layer, which is in good agreement with the bulk (1.69 nm)[76]. However, the FWHM of the first order peak for the flattened layer was estimated to 0.0271 (rad), while that for the interfacial sublayer was estimated to be 0.0140 (rad). Namely, the crystalline sizes (*L*), which can be calculated by the Scherrer equation[77], were estimated to be *L*=2.9 nm for the flattened later and *L*=5.6 nm for the interfacial sublayer. It should be noted that the FWHM of the first order peak for a 40 nm thick annealed P3HT thin film is 0.0105 (rad), which gives rise to *L*=7.5 nm. It is likely that this decrease in the crystalline size for the flattened layer is attributed to a

confinement effect: as the film thickness of the flattened layer is commensurate with the intermolecular backbone layer spacing, the ordering is retarded.
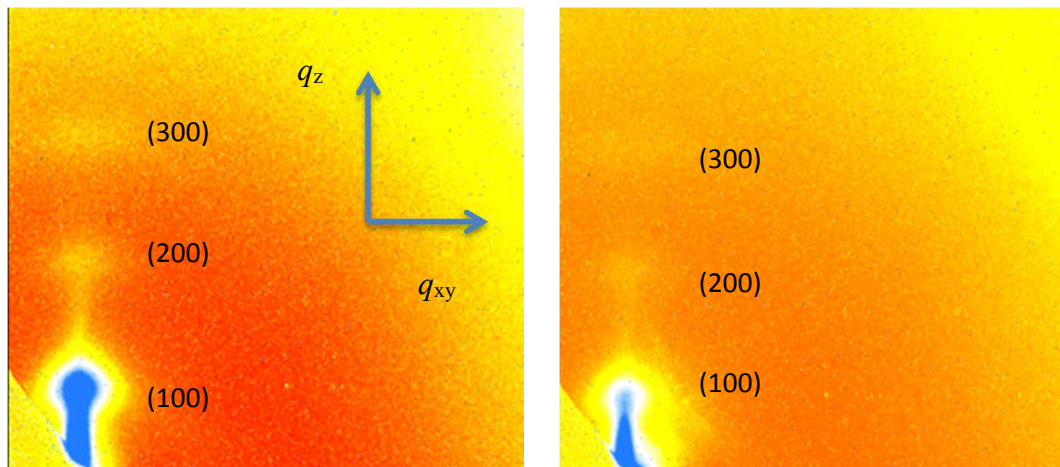
Figure 4- 10 GID results for the interfacial sublayer (left, 10 nm in thickness) and the flattened layer (right, 3 nm in thickness). The high intensity at the high q regime is due to scattering from the Si substrate.

Further GID experiments are needed to clarify the annealing time dependence of the chain orientations, allowing us to conclude the equilibrium chain conformations on the substrate surfaces.

Figure 4- 11 Out-of-plane GID profiles for the P3HT interfacial sublayer and flattened layer.

4.4.2. P3HT/PCBM adsorbed layers

We performed similar solvent leaching experiments for the P3HT/PCBM (the weight ratio of 1:1) thin films on the H-Si by using chlorobenzene. Ellipsometry results showed that the thicknesses of the P3HT/PCBM interfacial sub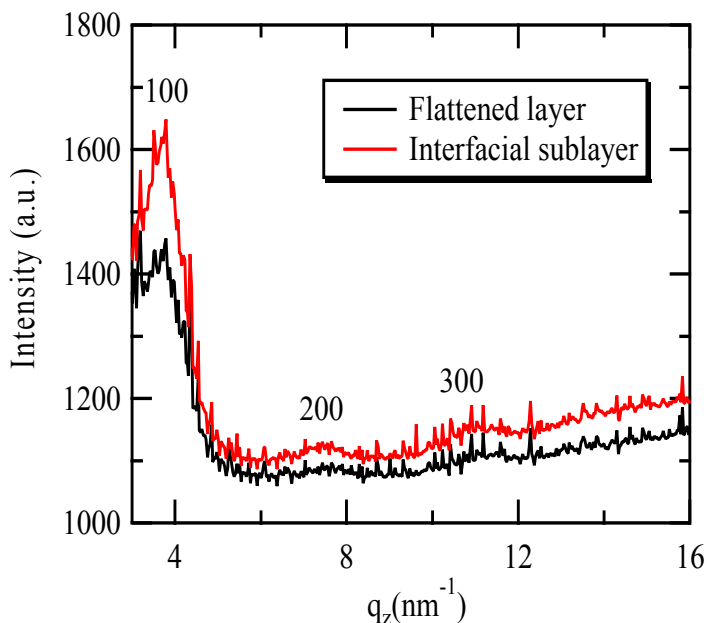layer and P3HT/PCBM flattened layer are 10 nm and 3.7 nm, respectively. Hence it is reasonable to suppose that the chain adsorption on the Si substrate is not affected by the presence of the PCBM nanoparticles. In addition, to study the thin films on B-Si and annealed at 170 °C for 48h and subsequently extracted the adsorbed and flattened layers by using the same solvent leaching protocol. The results are intriguing to show that the flattened layer thickness and the interfacial sublayer on the B-Si decreased to 1.8 nm and 7 nm, respectively with the surface tension of P3HT (26.9 mN/m)[78], the interfacial tension between interfacial sublayer and flattened layer on H-Si (a stronger interaction with PS) and B-Si (a weaker interaction with PS)[29, 32].

Table 4- 1 Interfacial energies used in the present study.

$\gamma_{HSi\text{-}P3HT}$	$\gamma_{HSi\text{-}PCBM}$	$E_{P, H\text{-}Si}$
2.13 mN/m	0.15 mN/m	1.98 mN/m
$\gamma_{BSi\text{-}P3HT}$	$\gamma_{BSi\text{-}PCBM}$	$E_{P, B\text{-}Si}$
3.98 mN/m	1.07 mN/m	2.91 mN/m

Figure 4- 12 AFM phase (left) and height (middle) images of the PCBM/P3HT flattened layer on H-Si. The corresponding cross-sectional height profile along the red line in the middle image is shown in the right graph.
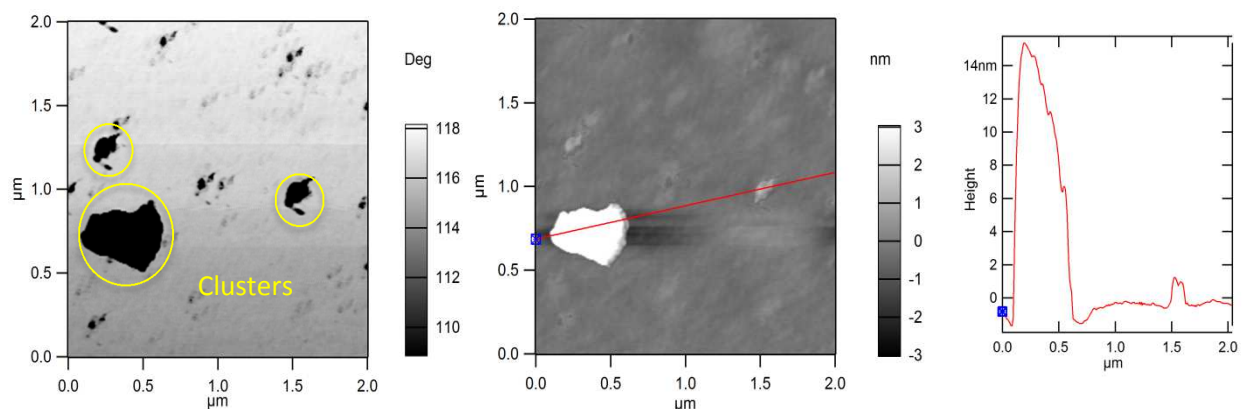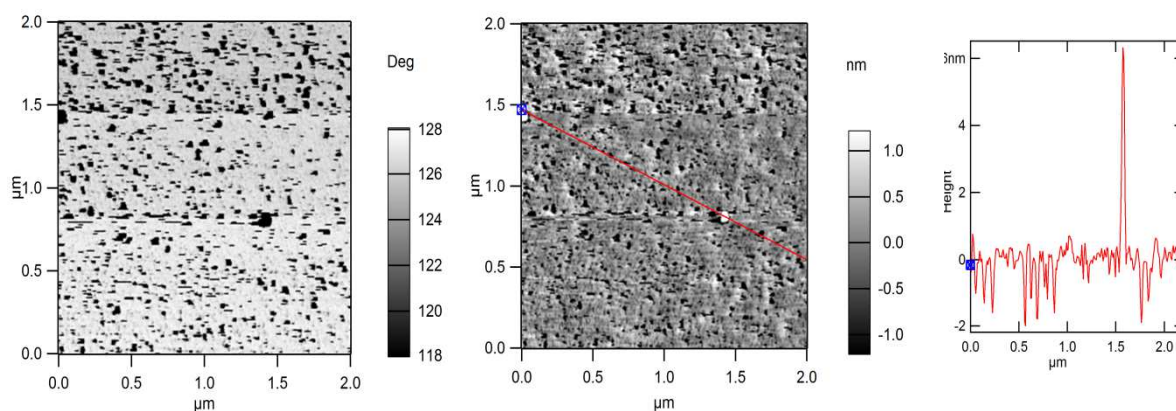

Figure 4- 13 AFM phase (left) and height (middle) images of the PCBM/P3HT flattened layer on B-Si. The corresponding cross-sectional height profile along the red line in the middle image is shown in the right graph.

Fig. 4-12 shows the AFM phase and height images of the P3HT/PCBM flattened layer on H-Si and B-Si. In the case of H-Si, it is clear that the PCBM nanoparticles form relatively large clusters with their sizes of submicron on the flattened layer or bulged into the flattened layer. The substrate was uniformly covered with the flattened layer, while the flattened layer also contains pores with several tens of nanometers. On the other hand, the surface morphology of the

P3HT/PCBM flattened layer on B-Si shows more holes in the polymer matrix. As shown in the cross-sectional image and phase image, it is likely that the holes penetrated to the substrate surface with the depth of ~ 2 nm, which is equivalent to the size of the PCBM individual nanoparticles.
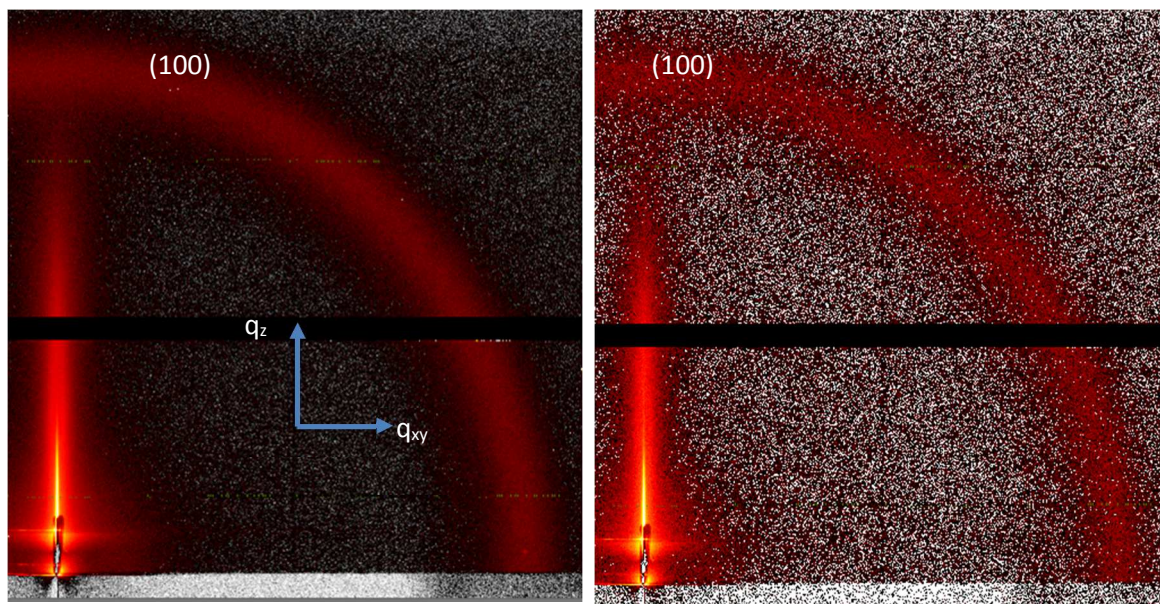
Figure 4- 14 2d-GID images of the P3HT/PCBM flattened layers on (left) H-Si and (right) B-Si.

It is known that nanoparticles often migrate to the film-substrate interface[79-87] and form a diffused immobile interfacial layer[79, 84, 85, 87]. Barnes and co-workers reported that the concentration of C_{60} nanoparticles in the diffused immobile interfacial layer reached about 50%, which is almost 10 times higher than the original particle concentration[79]. The particle migration is attributed to an entropy driven mechanism known as depletion attraction[88-90]. Krishnan and co-workers have shown that the loss in the translation entropy as well as the enthalpy of mixing of the particles are offset by the gain in the conformational entropy of polymer chains, as they are dislocated from the substrate due to the particle migration[84]. Karim and co-workers introduced a

new parameter, $E_p = \gamma_{S-P} - \gamma_{S-N}$, where γ_{S-P} and γ_{S-N} are the interfacial energy between the substrate and polymer and between the substrate and nanoparticles, respectively, to evaluate the energy penalty associated with a substrate being covered with PS or being covered with an immobilized layer of particles[87]. A higher positive value of E_p implies preferred migration of the particles toward the substrate interface. Based on the results, $E_p > 0$ for the H-Si and B-Si substrates such that the PCBM nanoparticles preferably migrate to the substrate surfaces. Hence, we postulate that the holes correspond to the areas where the nanoparticle clusters (several tens of nanometers) exist before the solvent leaching. Since the nanoparticles are not bound to the Si substrate, they can be easily washed off via the leaching process (unless the size is large enough (~ the micron scale), while the polymer chains are strongly bound to the substrate so that they retain the structures. As shown in Fig. 4-13, the pore density in the flattened layer formed on the B-Si is much higher than that formed on the H-Si, indicating more the nanoparticles are migrated to the B-Si surface, which is in good agreement with the magnitude of E_P tabulated in Table 4-1.
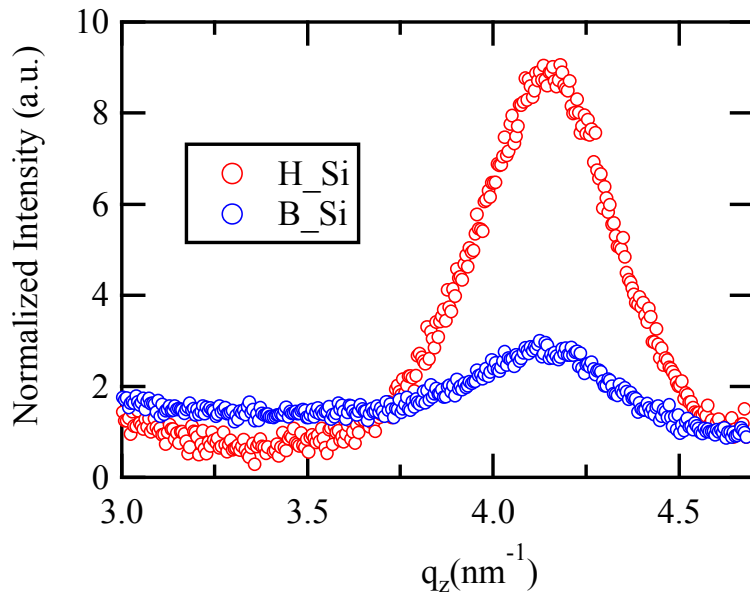

Figure 4- 15 1d-GID profiles of the P3HT/PCBM flattened layers on H-Si and B-Si.

Fig. 4-14 shows the 2d GID data for the P3HT/PCBM flattened layers on the two different surface treated Si substrates. Hence, as compared to Fig.4-10 (right), it is clear that the orientation of the backbone chains is randomized due to the presence of the PCBM nanoparticles on both H-Si and B-Si. Fig. 4-15 shows the 1d profiles integrated along the q_z direction and normalized by the film thickness. From the figure, the following two facts are evidenced:

(i)   The peak intensity for the flattened layer on H-Si is about 4 times higher than that for the flattened layer on B-Si, indicating that the grafting density of the bound polymer chains on H-Si is much higher than that on B-Si.

The peak position, which is determined to be $q = 4.1$ nm^{-1} for both H-Si and B-Si, shifts to the higher q value compared to the P3HT interfacial sublayer or the flattened layer (Fig. 4-11). This implies that the backbone stacking distance (1.53 nm) is shrunk by about 10% in the presence of the PCBM.

Hence, the impact of the PCBM nanoparticles on the local chain conformations of the π-conjugated polymer chains adsorbed on the substrate surface is significant. Further experiments are currently in progress to clarify the PCBM concentration dependence of the local chain conformations.

4.5.   Conclusion

The interfacial structures of the pure P3HT and P3HT/PBBM blend thin films on Si substrates with different surface treatments (H-Si and B-Si) were investigated by the established solvent leaching protocol in conjunction with a suite of surface sensitive experimental

techniques. The results are intriguing to reveal that the two different adsorbed layers (3 nm and 10 nm in thickness) are formed on the H-Si and B-Si regardless of the presence of the PCBM nanoparticles. We also found that the π-conjugated polymer chains still self-assemble into a predominant "edge-on" orientation even on the substrate surface, but the degree of the ordering is hindered. It was also found that while the total thickness of the interfacial sublayer and flattened layer remained unchanged with the inclusion of the PCBM nanoparticles, the local chain structures are significantly altered: the orientation of the π-conjugated polymer chains on the substrates become randomized and the packing of the backbone stacking is much tighter.

The edge-on orientation is often considered as an ideal one for bulk hetero-junction solar cells, namely alternating layers with interfacial plane between those layers orientated perpendicular to the substrate plane. Hence, the polymer chain orientations at the interfacial region where the polymer chains contact either cathode/anode may not be ideal for OPV devices. In order to investigate the effect, we will perform conductivity experiments for the interfacial sublayer and flattened layer in the near future. At the same time, sum frequency generation spectroscopy (SFG), which takes advantage of the fact that generation of a SFG photon is forbidden in the centrosymmetric bulk, but is nonzero at interfaces where inversion symmetry is broken[91-93], is needed to study the local chain orientations of the backbone and side chains of the π-conjugated polymer chains on the substrates. I believe that the better understanding of the structure-property relationship through my research work not only shed new light on the origin of the low efficiency of the current OPV, but also provide a new rational design for the next-generation OPV.

4.6. Acknowledgements

4.7. References

1. Alcoutlabi, M.; McKenna, G. B. *J. Phys. : Condens. Matter* **2005**, 17, R461-R524

2. Hu, X.-W.; Granick, S. *Science* **1992**, 258, 1339-1342

3. Bodiguel, H.; Fretigny, C. *Phys. Rev. Lett.* **2006**, 97, 266105

4. Koga, T.; Li, C.; Endoh, M. K.; Koo, J.; Rafailovich, M. H.; Narayanan, S.; Lee, D. R.; Lurio, L.; Sinha, S. K. *Phys. Rev. Lett.* **2010**, 104, 066101

5. Koga, T.; Naisheng, J.; Gin, P.; Endoh, M.; Narayanan, S.; Lurio, L.; Sinha, S. K. *Phys. Rev. Lett.* **2011**, 107, 225901

6. Ellison, C. J.; Torkelson, J. M. *Nature Mater.* **2003**, 2, 695-700

7. Fakhraai, Z.; Forrest, J. A. *Phys. Rev. Lett.* **2005**, 95, 025701

8. Fakhraai, Z.; Forrest, J. A. *Science* **2008**, 319, 600-604

9. Li, X.; McKenna, G. B. *Macromolecules* **2015**, 48, 6329-6336

10. Zheng, X.; Rafailovich, M. H.; Sokolov, J.; Strzhemechny, Y.; Schwarz, S. A.; Sauer, B., B.; Rubinstein, M. *Phys. Rev. Lett.* **1997**, 79, 241-244

11. Li, C.; Kim, H.; Li, C.; Jiang, J.; Koga, T.; Lurio, L.; Schwarz, S. A.; Narayanan, S.; Sinha, S.; Rafailovich, M. H.; Sokolov, J. C. *Europhys. Lett.* **2006**, 73, 899-905

12. Priestley, R. D.; Ellison, C.; Broadbelt, L. J.; Torkelson, J. M. *Science* **2005**, 309, 456-459

13. Frieberg, B.; Glynos, E.; Green, P. F. *Phys. Rev. Lett.* **2012**, 108, 268304

14. Frieberg, B.; Glynos, E.; Sakellarios, G.; Green, P. F. *ACS Macro Lett.* **2012**, 636-640

15. Torres, J. M.; Wang, C.; Coughlin, E. B.; Bishop, J. P.; Register, R. A.; Riggleman, R. A.; Stafford, C. M.; Vogt, B. D. *Macromolecules* **2011**, 44, 9040-9045

16. Xu, S. H.; O'Connell, P. A.; McKenna, G. B. *J. Chem. Phys.* **2010**, 132, 184902

17. Vanroy, B.; Wübbenhorst, M.; Napolitano, S. *ACS Macro Lett.* **2013**, 2, 168-172

18. Capitan, M. J.; Rueda, D. R.; Ezquerra, T. A. *Macromolecules* **2004**, 37, 5653–5659

19. Martin, J.; Nogales, A.; Mijangos, C. *Macromolecules* **2013**, 46, 7415−7422

20. Tang, Q.; Hu, W.; Napolitano, S. *Phys. Rev. Lett.* **2014**, 112, 148306

21. de Gennes, P. G. *Eur. Phys. J. E.* **2000**, 2, 201-203

22. de Gennes, P. G. *J. Chem. Phys.* **1971**, 55, 572-579

23. Yang, Z.; Fujii, Y.; Lee, F. K.; Lam, C.-H.; Tsui, O. *Science* **2010**, 328, 1676-1679

24. Ediger, M. D.; Forrest, J. A. *Macromolecules* **2014**, 47, 471-478

25. Asada, M.; Jiang, N.; Sendogdular, L.; Gin, P.; Wang, Y.; Endoh, M. K.; Koga, T.; Fukuto, M.; Schultz, D.; Lee, M.; Li, X.; Wang, J.; Kikuchi, M.; Takahara, A. *Macromolecules* **2012**, 45, 7098-7106

26. Asada, M.; Jiang, N.; Sendogdular, L.; Sokolov, J.; Endoh, M. K.; Koga, T.; M.Fukuto; Yang, L.; Akgun, B.; Dimitriou, M.; Satija, S. K. *Soft Matter* **2014**, 10, 6392-6403

27. Napolitano, S.; Wubbenhorst, M. *Nat. Comm.* **2011**, 2, 260-266

28. Gin, P.; Jiang, N. S.; Liang, C.; Taniguchi, T.; Akgun, B.; Satija, S. K.; Endoh, M. K.; Koga, T. *Phys. Rev. Lett.* **2012**, 109, 265501

29. Jiang, N. S.; Shang, J.; Di, X. Y.; Endoh, M. K.; Koga, T. *Macromolecules* **2014**, 47, 2682-2689

30. O'Shaughnessy, B.; Vavylonis, D. *Phys. Rev. Lett.* **2003**, 90,

31. O'Shaughnessy, B.; Vavylonis, D. *Eur. Phys. J. E.* **2003**, 11, 213-230

32. Jiang, N.; Wang, J.; Di, X.; Cheung, J.; Zeng, W.; Endoh, M. K.; Koga, T.; Satija, S. K. *Soft Matter* **2015**, DOI: 10.1039/c5sm02435h,

33. Richardson, H.; Carelli, C.; Keddie, J. L.; Sferrazza, M. *Eur. Phys. J. E* **2003**, 12, 437-440

34.   Reiter, G.; Hamieh, M.; Damman, P.; Sclavons, S.; Gabriele, S.; Vilmin, T.; Raphael, E. *Nat. Mater.* **2005**, 4, 754-758

35.   Damman, P.; Gabriele, S.; Coppee, S.; Desprez, S.; Villers, D.; Vilmin, T.; Raphael, E.; Hamieh, M.; Al Akhrass, S.; Reiter, G. *Phys. Rev. Lett.* **2007**, 99, 4

36.   Thomas, K. R.; Chenneviere, A.; Reiter, G.; Steiner, U. *Phys. Rev. E* **2011**, 83, 021804

37.   Barbero, D. R.; Steiner, U. *Phys. Rev. Lett.* **2009**, 102, 248303

38.   Chung, J. Y.; Chastek, T. Q.; Fasolka, M. J.; Ro, H. W.; Stafford, C. M. *ACS Nano* **2009**, 3, 844-852

39.   Fujii, Y.; Yang, Z. H.; Leach, J.; Atarashi, H.; Tanaka, K.; Tsui, O. K. C. *Macromolecules* **2009**, 42, 7418-7422

40.   Fleer, G. J.; Cohen Stuart, M. A.; Scheutjens, J. M. H. M.; Cosgrove, T.; Vincent, B., *Polymers at Interfaces*. Chapman and Hall: London, 1993.

41.   Schuetjens, M. H. M.; Fleer, G. J. *J. Phys. Chem.* **1980**, 84, 178-190

42.   Guiselin, O. *Europhys. Lett.* **1992**, 17, 225-230

43.   Shull, K. R. *Macromolecules* **1996**, 29, 8487-8491

44.   Durning, C. J.; O'Shaughnessy, B.; Sawhney, U.; Nguyen, D.; Majewski, J.; Smith, G. S. *Macromolecules* **1999**, 32, 6772-6781

45.   Napolitano, S.; Wubbenhorst, M. *J. Phys. Chem. B* **2007**, 111, 9197-9199

46.   Napolitano, S.; Prevosto, D.; Lucchesi, M.; Pingue, P.; D'Acunto, M.; Rolla, P. *Langmuir* **2007**, 23, 2103-2109

47.   Napolitano, S.; Lupascu, V.; Wubbenhorst, M. *Macromolecules* **2008**, 41, 1061-1063

48.   Rotella, C.; Napolitano, S.; De Cremer, L.; Koeckelberghs, G.; Wubbenhorst, M. *Macromolecules* **2010**, 43, 8686-8691

49.   Napolitano, S.; Rotella, C.; Wubbenhorst, M. *Macromol. Rapid Commun.* **2011**, 32, 844-848

50.   Villars, D. S. *J. Polym. Sci.* **1956**, 21, 257-271

51.   Medalia, A. I. *J. Colloid Interface Sci.* **1970**, 32, 115

52.   Blow, C. M. *Polymer* **1973**, 14, 309

53.   Dannenberg, E. M. *Rubber Chem. Technol.* **1986**, 59, 512

54.   Kenny, J. C.; McBrietry, V. J.; Rigbi, Z.; Douglass, D. C. *Macromolecules* **1991**, 24, 436

55.   Karasek, L.; Sumita, M. *J. Mater. Sci.* **1996**, 31, 281-289

56.   Harton, S. E.; Kumar, S. K.; Yang, H. C.; Koga, T.; Hicks, K.; Lee, E.; Mijovic, J.; Liu, M.; Vallery, R. S.; Gidley, D. W. *Macromolecules* **2010**, 43, 3415-3421

57.   Jouault, N.; Moll, J. F.; Meng, D.; Windsor, K.; Ramcharan, S.; Kearney, C.; Kumar, S. K. *ACS Macro Lett.* **2013**, 2, 371-374

58.   Jiang, N.; Endoh, M. K.; Koga, T.; Masui, T.; Kishimoto, H.; Nagao, M.; Satija, S. K.; Taniguchi, T. *ACS Macro Lett.* **2015**, 4, 838-842

59.   Farago, B.; Monkenbusch, M.; Richter, D.; Huang, J. S.; Fetters, L. J.; Gast, A. P. *Phys. Rev. Lett.* **1993**, 71, 1015-1018

60.   Jiang, N.; Endoh, M. K.; Koga, T., Structures and Dynamics of Adsorbed Polymer Nanolayers on Planar Solid. In *Non-Equilibrium Phenomena in Confined Soft Matter*, Napolitano, S., Ed. Springer: 2015; pp 129-160.

61.   Shin, K.; Hu, X.; Zheng, X.; Rafailovich, M. H.; Sokolov, J.; Zaitsev, V.; Schwarz, S. A. *Macromolecules* **2001**, 34, 4993-4998

62.   Seeck, O. H.; Kaendler, I. D.; Tolan, M.; Shin, K.; Rafailovich, M. H.; Sokolov, J.; Kolb, R. *Appl. Phys. Lett.* **2000**, 76, 2713-2715

63.	Koga, T.; Seo, Y. S.; Jerome, J.; Ge, S.; Rafailovich, M. H.; Sokolov, J. C.; Chu, B.; Seeck, O. H.; Tolan, M.; Kolb, R. *Appl. Phys. Lett.* **2003**, 83, 4309-4311

64.	Gin, P.; Asada, M.; Endoh, M. K.; Gedelian, C.; Lu, T. M.; Koga, T. *Appl. Phys. Lett.* **2009**, 94,

65.	Linse, P.; Källrot, N. *Macromolecules* **2010**, 43, 2054-2068

66.	O'Shaughnessy, B.; Vavylonis, D. *J. Phys. Condens. Matter.* **2005**, 17, R63-R99

67.	Källrot, N.; Linse, P. *Macromolecules* **2007**, 40, 4669-4679

68.	Ma, Y.; Hu, W.; Reiter, G. *Macromolecules* **2006**, 39, 5159-5164

69.	Yang, J. P.; Liao, Q.; Zhou, J. J.; Jiang, X.; Wang, X. H.; Zhang, Y.; Jiang, S. D.; Yan, S. K.; Li, L. *Macromolecules* **2011**, 44, 3511-3516

70.	Kawai, A.; Kawakami, J.; Sasazaki, H. *Journal of Photopolymer Science and Technology* **2008**, 21, 739-740

71.	Gin, P.; Jiang, N.; Liang, C.; Taniguchi, T.; Akgun, B.; Satija, S. K.; Endoh, M. K.; Koga, T. *Physical Review Letters* **2012**, 109, 265501

72.	O'Shaughnessy, B.; Vavylonis, D. *European Physical Journal E* **2003**, 11, 213-230

73.	O'Shaughnessy, B.; Vavylonis, D. *Physical Review Letters* **2003**, 90, 056103

74.	Ocko, B. M.; Wu, X. Z.; Sirota, E. B.; Sinha, S. K.; Gang, O.; Deutsch, M. *Phys. Rev. E* **1997**, 55, 3164-3182

75.	Xing, F.; Su-Ling, Z.; Yu, C.; Jie, Z.; Qian-Qian, Y.; Wei, G.; Meng-Yao, Y.; Zheng, X.; Xu-Rong, X. *Chinese Phys. B* **2015**, 24, 078401

76.	Kayunkid, N.; Uttiya, S.; Brinkmann, M. *Macromolecules* **2010**, 43, 4961

77.	Scherrer, P. *Nachr. Ges. Wiss. Göttingen* **1918**, 26, 98-100

78.	Germack, D. S.; Chan, C. K.; Hamadani, B. H.; Richter, L. J.; Fischer, D. A.; Gundlach,

D. J.; DeLongchamp, D. M. *Appl. Phys. Lett.* **2009**, 94, 233303

79.   Barnes, K. A.; Karim, A.; Douglas, J. F.; Nakatani, A. I.; Gruell, H.; Amis, E. J. *Macromolecules* **2000**, 33, 4177-4185

80.   Mackay, M. E.; Hong, Y.; Jeong, M.; Hong, S.; Russell, T. P.; Hawker, C. J.; Vestberg, R.; Douglas, J. F. *Langmuir* **2002**, 18, 1877-1882

81.   Wei, B.; Gurr, P. A.; Genzer, J.; Qiao, G. G.; Solomon, D. H.; Spontak, R. J. *Macromolecules* **2004**, 37, 7857−7860

82.   Besancon, B. M.; Green, P. F. *Macromolecules* **2005**, 38, 110-115

83.   Kropka, J. M.; Green, P. F. *Macromolecules* **2006**, 39, 8758-8762

84.   Krishnan, R. S.; Mackay, M. E.; Duxbury, P. M.; Hawker, C. J.; Asokan, S.; Wong, M. S.; Goyette, R.; Thiyagarajan, P. *J. Phys.: Condens. Matter* **2007**, 19, 356003-1-16

85.   Han, J. T.; Lee, G. W.; Kim, S.; Lee, H. J.; Douglas, J. F.; Karim, A. *Nanotechnology* **2009**, 20, 105705

86.   Mukherjee, R.; Das, S.; Das, A.; Sharma, S. K.; Raychaudhuri, A. K.; Sharma, A. *ACS Nano* **2010**, 4, 3709−3724

87.   Roy, S.; Bandyopadhyay, D.; Karim, A.; Mukherjee, R. *Macromolecules* **2015**, 48, 373-382

88.   Lee, J. Y.; Buxton, G. A.; Balazs, A. C. *J. Chem. Phys.* **2004**, 121, 5531−5539

89.   Kropka, J. M.; Putz, K. W.; Pryamitsyn, V.; Ganesan, V.; Green, P. F. *Macromolecules* **2007**, 40, 5424−5432

90.   Green, P. F. *Soft Matter* **2011**, 7, 7914-7926

91.   Gautam, K. S.; Schwab, A. D.; Dhinojwala, A.; Zhang, D.; Dougal, S. M.; Yeganeh, M. S. *Phys. Rev. Lett.* **2000**, 85, 3854−3857

92.   Shen, Y. R. *Nature* **1989**, 337, 519-525

93.   Chen, Z.; Shen, Y. R.; Somorjai, G. A. *Annu. Rev. Phys. Chem.* **2002**, 53, 437-465